University of Southampton Research Repository

UNIVERSITY OF SOUTHAMPTON

FACULTY OF ENGINEERING AND THE ENVIRONMENT

Energy Technology

Design of Hierarchically Structured BiOBr-based Photocatalysts and Photoelectrodes for Enhanced Solar Energy Conversion

by

Junqiu Guo

Thesis for the degree of Doctor of Philosophy

July 2019

UNIVERSITY OF SOUTHAMPTON

ABSTRACT

FACULTY OF ENGINEERING AND THE ENVIRONMENT

Engineering

Thesis for the degree of Doctor of Philosophy

Design of Hierarchically Structured BiOBr-based Photocatalysts and Photoelectrodes for Enhanced Solar Energy Conversion

Junqiu Guo

Photocatalysis is deemed as a sustainable approach for environment remediation and solar energy conversion, for which the practical viability is highly dependent on the high-performance photocatalysts and device. The pristine and modified BiOBr materials have recently emerged as promising photocatalysts in solar energy photocatalysis, though the facile constructions of hierarchical structures and the explicit dependence of band structure on metal-dopant have not well developed. This PhD research project aims to fabricate robust BiOBr-based photocatalysts and to unravel the relationship between their photocatalytic performance and photoelectrochemistry properties.

First, the Zn-doped BiOBr (denoted as Zn-BiOBr) were prepared via hydrothermal synthesis under basic solution and tested for dye photodegradation and photocatalytic H_2 evolution from water splitting using methanol as hole scavenger. The Zn-BiOBr samples display broader bandgaps (Eg) and higher photocatalytic H_2 evolution but detrimental activity in photodegradation of Rhodamine B (Rh.B) dye in a model wastewater in textile industry. The experimental (UV-Vis spectra, XPS and photoelectrochemistry) and DFT characterisations suggest the Zn-doping uplifts the conduction band minima (CBM) and deepen the valence band maxima (VBM), which provides enhanced driving force for water splitting, though the wider Eg weakens light absorbance and dye sensitisation ability and thus leading to detrimental RhB photodegradation activity.

Second, hierarchically structured Zn-BiOBr and BiOBr samples (annotated as Zn-BiOBr-H and BiOBr-H) composing of nano-flake building blocks were prepared using PEG-assisted hydrothermal synthesis. Comparing with irregular ZnBiOBr and BiOBr, the Zn-BiOBr-H and BiOBr-H exhibit superior performance in RhB photodegradation,

Table of Contents

photocatalytic H_2 evolutions and energy recovery from wastewater. The enhanced performance in these reactions is mainly due to the larger specific surface areas and attenuated light scattering of the hierarchical samples. A well-established mechanism of photocatalytic reaction on the hierarchical architectures was proposed in this work.

Third, the PEG-assisted hydrothermal synthesis was adopted in preparation of hierarchical BiOBr/ZnO heterojunctions (denoted as BiOBr/ZnO-PEG) with varying BiOBr loading. The photocatalysis results suggest the BiOBr/ZnO-PEG heterojunctions possess lower activity in RhB photodegradation under visible light, which is due to the coverages of surface-active sites of BiOBr by ZnO. Such synthesis method is extended to preparation of ZnO and S-doped ZnO, which possess different hierarchical structures compared to those of BiOBr-H and BiOBr/ZnO-PEG, confirming the previous proposed mechanism of construction of hierarchical architectures of BiOBr-H and Zn-BiOBr-H. Moreover, the dye photodegradation and photocatalytic antibacterial results confirm that photocatalysis contributes significantly for antibacterial property on ZnO, while S-doped ZnO possess intrinsic bactericidal capability and less dependence on photo-catalysis.

In order to improve the light harvesting on BiOBr, the I-doped BiOBr ($BiOBr_xI_{1-x}$) were prepared using a successive dip-coating method to deposit into CuSCN nanorod arrays grown on ITO substrates. The $BiOBr_xI_{1-x}$/CuSCN films with varied Br/I ratios and coating layers were compared in their photocurrent response. The increased photocurrent of the $BiOBr_xI_{1-x}$/CuSCN films indicated that coupling with $BiOBr_xI_{1-x}$ not only increased the light absorption of CuSCN films, but also supressed the charge recombination by the built-in electric field across the interface of $BiOBr_xI_{1-x}$/CuSCN heterojunctions. In addition, via electrochemistry impedance characterisations, the fabrication conditions of the $BiOBr_xI_{1-x}$/CuSCN heterojunctions are optimised.

Table of Contents

Table of Tables

Table of Figures

Table of Figures

Table of Figures

Academic Thesis: Declaration of Authorship

I, Junqiu Guo ....

declare that this thesis and the work presented in it are my own and has been generated by me as the result of my own original research.

Design of Hierarchical Structured Semiconductor Photocatalysts and Photoelectrodes for Enhanced Solar Energy Conversion ....

I confirm that:

1. This work was done wholly or mainly while in candidature for a research degree at this University;
2. Where any part of this thesis has previously been submitted for a degree or any other qualification at this University or any other institution, this has been clearly stated;
3. Where I have consulted the published work of others, this is always clearly attributed;
4. Where I have quoted from the work of others, the source is always given. With the exception of such quotations, this thesis is entirely my own work;
5. I have acknowledged all main sources of help;
6. Where the thesis is based on work done by myself jointly with others, I have made clear exactly what was done by others and what I have contributed myself;
7. None of this work has been published before submission.

Signed: ....

Date: ....

Acknowledgements

This four years' work has finally come to an end today. So are my schooldays. Behind every page of this work it lays not only persistent effort, but also cherished memories of days and nights in the past four years. I would appreciate all the help and guidance I have received all the way here. This work won't be accomplished without guidance and teaching from my supervisor Dr Zheng Jiang. Thank you for offering this opportunity to work with you in this interesting project. His generous help and inspiring notes enlighten me from the gloomy research dilemma.

Also, I want to express my gratitude to my friends and colleagues. Without the help from them, I won't be a good cook and housekeeper. Thank you all for sharing this four years' story with me. I will never forget the days we spend together in the lab and pubs. Best wishes to you. See you again my friends!

Of course, the help and support from my parents and family has always been indispensable part of my life. I will never stand in this place without their tremendous support.

In the last, I want to say thank you to my wife, Miss Zhang. Thank you for support and company during the past four years no matter it good or bad, rains or shine, laugh and cry.

And thank you, my son, Xiaoheng.

Definitions and Abbreviation

C

CB. ....Conduction band

CBM .... Conduction band bottom

CPE..Constant phase element

CTAB ....Cetyl trimethylammonium bromide

CVD... Chemical vapor deposition

E

Eg... Energy band gap

EIS.. Electrochemical Impedance Spectroscopy

ESCA...Electron Spectroscopy for Chemical Analysis

M

MOCVD...Metal Organic Chemical Vapor Deposition

MS...Mott Schottky

N

NHE...Normal Hydrogen Electrode

R

NHE...Normal Hydrogen Electrode

S

SEM...Scanning Electron Microscope

T

TBAB..Tetra-n-butylammonium bromide

TEM..Transmission Electron Microscope

V

VB...Valence band

VBM..Valence band Maximum

Definitions and Abbreviation

X

Chapter 1 Solar Photocatalysis on Semiconductor Photocatalysts

1.1   Introduction

Nowadays, human beings are facing an unprecedented global crisis on the energy and environment due to the ever-increasing consumption of the unsustainable fossil fuels (petrol, natural gas and coal) that threating climate and energy safety. Therefore, it is necessary to explore and exploit cleaner and renewable energy. Solar energy can be one of the best choice because it is free from the pollution and almost infinite though its widespread applications are undergoing [1].

Nowadays, the efficiency of the solar harvesting has been able to reach 46 % of the concentrated photovoltaics (PV) in laboratory and around 20 % of practical modules, however, the cost of such facilities to meet domestic needs is over £8000 (Excl. VAT) [2]. The costly facilities and materials of PVs inevitably curb the application of materials for solar energy harvesting. As a result, low-cost, reliable and efficient materials and solutions are desired to expand the solar energy conversion.

In comparison with photovoltaics, the photocatalysis represents another solar energy conversion process which utilises photons absorbed by semiconductor photocatalysts to generate active species and thus drive the chemical reaction on the intermedia/photocatalyst interface. In a typical photocatalytic reaction, as shown in Figure 1-1, the global photocatalytic process consists of three parts: photo-excitation, charge transportation and surface reactions, instead of two counterparts for PVs: photo-excitation and charge transportation.

1.1.1 The photocatalysis process and requirements

In detail, when light with energy higher than the photocatalyst bandgap (E_g) strikes on the surface of photocatalysts during photocatalysis, photo excitation will take place, leading to the generation of electron/hole (e^-/h^+) pairs. The absorption of the photon is always the very first step of photocatalytic reactions. The light absorption is mainly determined by two factors: the bandgap and morphology of the photocatalysts. Band gap, also called energy gap, is an energy range in a material where no electron permission states can exist [3]. And the band gap usually refers to the energy difference between the bottoms of the conduction band (CBM) and top of the valence band (VBM) in semiconductors [4]. As known to us, metals are

good conductors of electricity and heat, because continuous electrons states allow a large number of free electrons to carry charges or heat moving all through metals structures. Unlike metals, semiconductors possess separated the energy band of electrons, which make most of electrons localized in the valence band and difficult to move around in the materials. If an electron hops to the conduction band and become a free electron, it requires the minimum absorption energy of E_g for an electron to overcome the energy gap between the two bands [5]. When the energy of incident light is greater than that of a band gap of the semiconductors, the electrons in the valence band are capable to gain enough energy to jump to the conduction band and electron-hole pairs are generated in the conduction band and valence band, respectively [6]. Therefore, the photo-absorption of semiconductor is closely related with the value of the band gap of the materials [7].
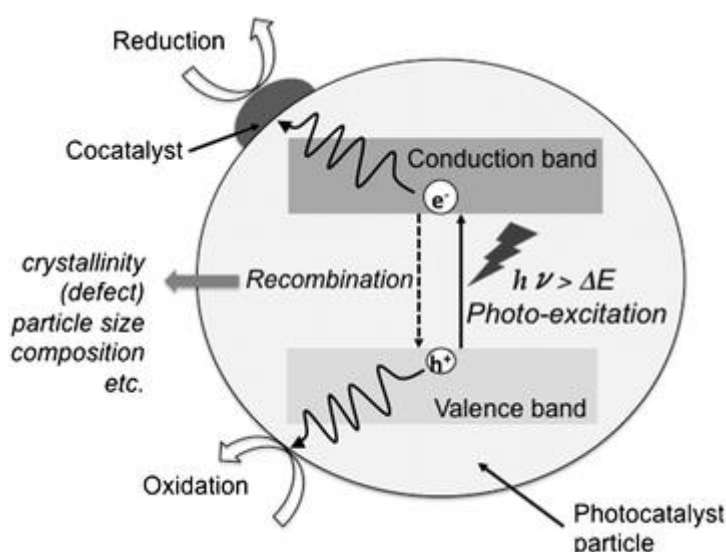
Figure 1-1 General process of photo-catalysis [8]

Following photo excitation, the charges will immediately be transported to the surface for the further reaction. However, a considerable part of photo-excited charge will be consumed due to the charge recombination during the charge separation and transportation [9]. Various factors, such as crystal structure, crystallinity and particle size, strongly affect this step. Low crystallinity of the materials leads to high concentrations of defects and the defects will act as trapping and recombination centres for the electron-holes charge carriers [10-12]. Therefore, the large number of defects will decrease the reactivity of the semiconductor photo-catalysts, while suitable levels of structural defects can even promote the photocatalysis due to its narrowing Eg and enhancing charge mobility. Moreover, photocatalyst particle size influences the charge transportation now that smaller sizes can reduce the transportation distance of photo-generated charge carriers to the reactive sites on the surface of semiconductor, and might decrease

the recombination probability [13]. Instead of producing thermal energy in the bulk through the charge recombination, the charges carriers migrated to the surface can produce free radicals (e.g. hydroxyl radicals $\cdot$OH) with surrounding species and initiate secondary reactions [14]. The surface reaction including oxidation and reduction can be applied in degradation of pollutant, reduction of CO_2, evolution of H_2 and formation of organic chemicals. According to the Gibbs free energy change, the surface reactions are assigned to uphill and downhill reactions.

As a typical surface reaction, photocatalysis efficiency highly depends on the surface area ratio of the photocatalysts [15, 16]. Lager area not only supplies richer reaction sites for the photo-excitons, but also provide larger area for the adsorption/desorption of photocatalysis reactants/products [17]. Therefore, the key factors governing the reaction of the photo-catalysts can be categorised into four parts: light absorption, energy band structure, charge transportation and surface reactions. Understanding the influence of each factor is of inherent importance to promote the efficiency of the photo-catalytic system. Apart from that, toxicity and stability of the materials also deserve intensive attention, because the environment aspect of the many photo-catalysts is still under heavily debate, such as CdS, TeZnCd, and V_2O_5 etc [18]. These materials exhibit promising photocatalytic performance, though they are challenged with the negative impacts on environment, due to their corrosion under intensive light irradiation [19].

Since the photocatalytic performance of TiO_2 was first reported by Fujishima in 1972, a large number of the semiconductor materials are successfully prepared, including oxides of the metallic elements, sulphides, nitrides, metal-free semiconductors and elemental photocatalysts [20-23]. Nevertheless, few of these materials completely meet all the practical requirements such as long lifetime of charge carries, suitable band gap for ultimate utilization of solar energy, low-cost, high efficiency, environmentally friendly and good stability in reaction conditions. Therefore, it is urgent to develop environment-friendly, highly efficient and visible-light driven photocatalysts [20, 24-28].

The Figure 1-2 illustrates the band gaps and band edge position of several semiconductor materials which are widely attempted and reported in literature. The data refers to conditions where the semiconductor is in contact with aqueous electrolyte of pH 0 [29]. It is worth noting that the energy band potential shifts with a change in pH, which can be described by the equation:

$$\Delta E_g = -0.059 pH$$

The standard potentials for several redox couples are also shown in Figure 1-2 with the reference to NHE (normal hydrogen electrode), which indicates the thermodynamic limitations for the photocatalytic reactions that could be carried out under the photo-excitations.
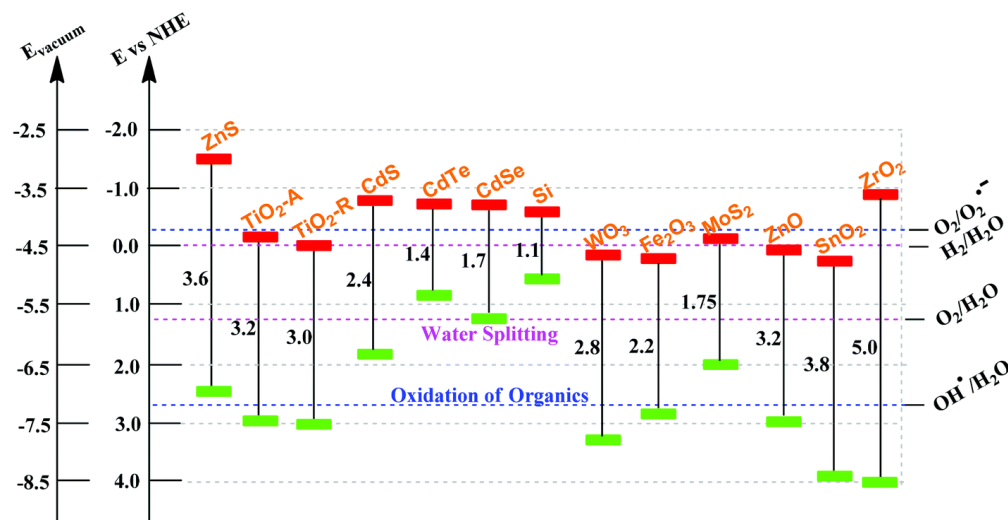
Figure 1-2 Valence and conduction band position for a range of semiconductors on potentials scales (eV) versus the standard hydrogen electrode (SHE) [29]

From thermodynamic viewpoint, photo generated charge carriers should provide sufficient energy to motivate surface oxidation and reduction. In other words, the reduction and oxidation potentials of chemicals should lie between the conduction band (CB) and valence band potentials. if a reduction reaction of the species in the electrolyte is going to be performed, CBM position of semiconductor materials must be located above the relevant redox level; and for an oxidation reaction, the valence position of the semiconductor has to be positioned below the relevant redox level [30]. The free energy of the charge carriers generated by photoexcitation of semiconductors is directly related to their chemical potential. In the dark, upon thermal equilibrium, the chemical potential of the electron is equal to that of the hole and corresponds to the Fermi level of the solid [31].

Generally, photocatalytic process can be categorised into four sections, including excitation of the electrons, the separation of charges (holes and electrons), charge transportation and following reaction. In order to improve the performance of photo-catalysts, some optimization should be introduced into the materials.

1.2   Strategies to improve the performance

Correspond to the previous analysis, the research strategy towards improving the performance and applications of the photo-catalysis can be concluded as energy-

band engineering, morphology & structure engineering, charge transportation optimization and film preparation. The picture down here depicts the roadmap of my strategies. The first stage concentrated on the structure tailoring and the material preparation.

```
┌──────────────────┐        ┌──────────────────┐
│   Structure &    │  ───▶  │   Energy-band    │
│     Sythesis     │        │   engineering    │
└──────────────────┘        └──────────────────┘
                                      │
                                      ▼
┌──────────────────┐        ┌──────────────────┐
│      Film        │  ◀───  │     Charge       │
│   preparation    │        │  transportaion   │
│                  │        │   optimization   │
└──────────────────┘        └──────────────────┘
```
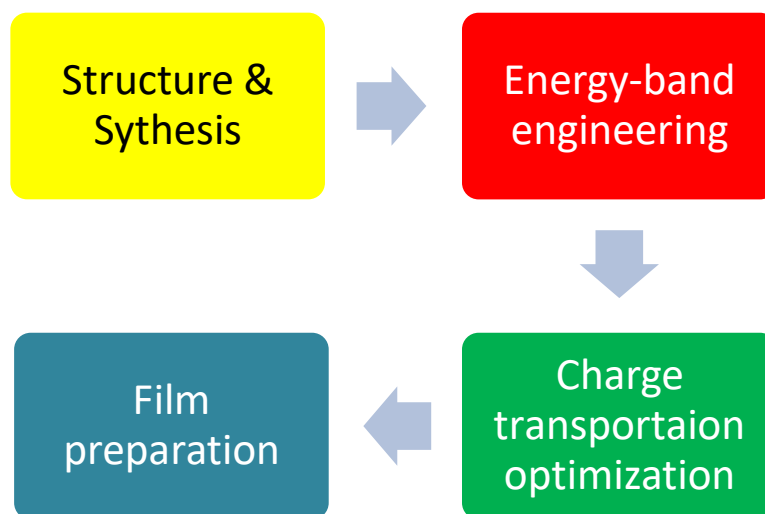
Figure 1-3 Strategy of optimization of photocatalysts

1.3 Photocatalytic Materials

1.3.1 Overview

Photocatalyst are usually defined as a class of materials which are capable to transform solar energy into chemical or electrical energy without being consumed during the reactions [25]. Typically, the engineering approaches to modify the photocatalysts can be concluded in two aspects: structure modification and composition adjustment. Especially, as the photocatalytic performance of materials is strongly influenced by their crystal structures and morphologies, structure optimization of a given materials is of critical importance in the performance enhancement. So far, numerous promising strategies of structure engineering has been proposed to obtain a desirable morphology. Among them, the self-assembly synthesis of hierarchical structure turned out to be a feasible method to promote the quantum efficiency and light absorbance.

The hierarchically structured materials are the materials with multidimensional domains at different levels or multimodal pore structures such as nano-rods, mesoporous, flake-assembled and tree-like. By mimicking the hierarchical and topological structure (trees, flowers, snowflakes, etc.), the hierarchical photocatalyst in the nature possess interconnected structure and large specific surface areas, which not only increase the light absorbance and energy input, but

also facilitate the transportation of charge carriers. Thus, the synergetic of multilevel of hierarchical structures often lead to the enhancement of photocataltic performance of materials.

Currently, a large number of research has been published on novel design of hierarchically structured materials such as TiO_2, ZnO, Fe_2O_3, etc. [5, 32], because these materials are chemically stable, environmental friendly and cost effectively during the preparation and reactions [24]. All these materials are endowed with excellent UV response and photo-catalytic activity. However, the wide band gaps of most aforementioned materials hinders their harvesting to visible light, that is the electrons of the solids can only be excited under the ultraviolet radiation [33]. Suffering from the relatively wide band gap and the charge recombination, these materials present lower energy conversion efficiency compared to narrow-bandgap photocatalysts (such as BiOBr and MoS_2) [34].

To increase the solar energy conversion, some materials with smaller band gap and intrinsically excellent charge separations have drawn our interest. This project concentrated on three types of catalysts: BiOX, ZnO and CuSCN, which are then used to build hybrid photocatalyst with desirable performance. As reported in literature, the hierarchical architectures of nano-crystal photocatalysts often possessed unique properties and exceptional performance, depending significantly on the morphology, shape, or orientation geometry and crystal surface of the constituent structure. However, construction of hierarchical photocatalyst from constituent nano-blocks remains a great challenge due to enormous thermodynamic, kinetic and technical challenges due to their structure complexity.

On the other hand, inspired from the signal amplification of diode in artificial circuit, heterojunction is also introduced in this project to further improve the photocatalytic performance of the materials [35]. Most common heterogeneous photo-catalysts are transition metal oxides, which have unique characteristics. Therefore, the interest of this project is mainly focus on the engineering the morphology and structure of the semiconductor and photo-catalyst, such as BiOBr, and ZnO etc. Among of those materials, the BiOBr could be one of the most prosperous candidates. Despite a plenty of research had been carried out on novel design of hierarchical photocatalysts, only a handful of papers explored and compared the mechanism of photocatalysis, in particular via photoelectrochemistry (PEC) methodologies.

1.3.2   Hierarchical ZnO

ZnO is a wide band gap semiconductor and has several favourable properties such as good transparency, high electron mobility and room-temperature luminescence. In the hierarchical ZnO materials synthesis, various microscopic textures can be categorized into mainly three groups which are nanorods, nanoflakes and nanospheres. Also, oriented hierarchical nanowires are another type of structure we are pursuing[36]. Because of different morphology, they carry various physical and chemical properties. The ZnO has a promising place in the NH_4 sensor and reduction in the NOx [37].

The structure of ZnO is a dominant factor for photocatalytic reaction because it will determine their applications in various fields. A suitable nanostructured ZnO will improve the efficiency of process and enhance the recovery of photocatalyst during post-treatment stage. Hierarchical structured ZnO can be categorised into four types: zero-dimensional (0D), one-dimensional (1D), two-dimensional (2D), three-dimensional (3D). [38]. Figure 1-4 shows the morphologies of hierarchical ZnO in various dimensions. Quantum dots shown in Figure 1-4 (a) represent ZnO in 0D. Nanorods arrays, nanosheets and nanoflowers shown in the following images are the examples of ZnO in 1D, 2D and 3D, respectively.

As mentioned above, the photocatalytic performance is affected by its specific surface area. The large specific surface area of ZnO enable more absorption of reactant molecular and thus provide more active sites for the photocatalytic reactions. Additionally, according to the research by Qi et al. [39], ZnO nanoflowers possessed a better light scattering properties compared to ZnO nanorods. By increasing the dimension level of the ZnO structure, the light absorbance is also dramatically enhanced. However, complexity of its structure also introduced some problems during the synthetic process and post-treatment. In Table 1-1 the advantages and disadvantages of ZnO in various structure are listed and compared.

ZnO has a tetrahedral bonding configuration and is an intrinsically n-type semiconductor due to the Zn-rich conditions. The defects such as oxygen vacancies (V_o) and zinc vacancies (V_{zn}) affect its optical and electric properties. It has been verified that increasing V_o in ZnO will lead to an increasing number of electron charge carriers. Accordingly, to achieve enhancement in the photocatalysis, introduction of appropriate defects or elements can be adopted to modify the energy band structure of ZnO. Recent studies unveiled that non-metal doping such as nitrogen, carbon, sulphur and fluorine are capable to narrow down the band gap

of ZnO by uplifting the valence band. More specifically, those impurities diffuse through the lattice interstices and bind to the atoms via oxidation process. The dopants incorporate into the crystal lattice and replace the position of oxygen, whose electrons mainly contribute to the valence band of ZnO. Moreover, transitional metal, rare earth elements and noble metals had also been introduced for band structures tuning. The metal doping offers the another means to improve the photocatalytic activity of the materials by increasing the trapping sites of electrons, which will reduce the charge recombination rate within the materials.

However, introducing impurities won't guarantee the promotion in photocatalytic performance. The amount and type of dopants should be carefully chosen. High level doped ZnO may result in the attenuation or decrease of the photocatalytic performance. In over-doped ZnO, the dopants may significantly change the lattice structure of the materials. The degradation in the structure and atom bonding would probably poison the performance of photocatalyst. Generally, there is no directed correlation between photocatalytic activity and dopant content level. In most cases, the overall performance of materials is synergic effect of crystallinity, structure, composition, specific surface area and reaction dynamics on the surface.
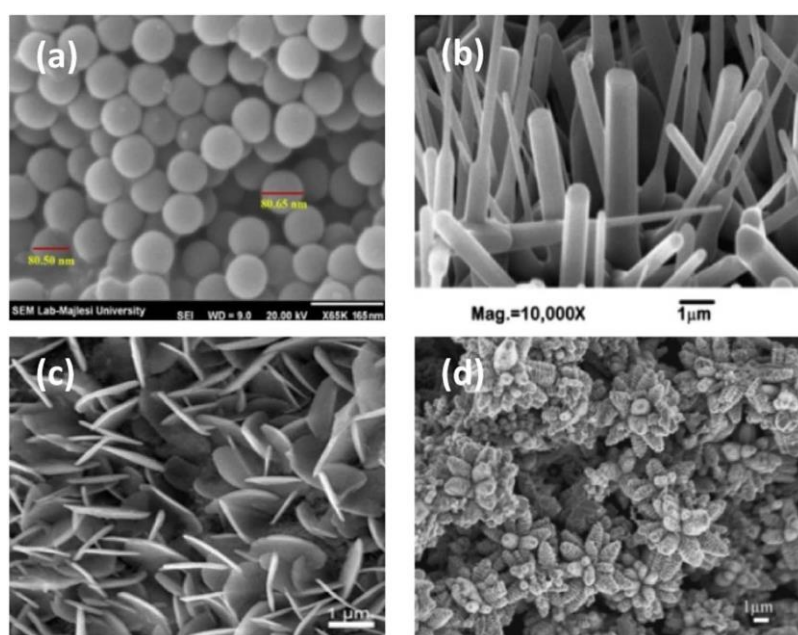
Figure 1-4 FESEM and SEM images for (a) 0D, (b) 1D, (c) 2D, (d) 3D ZnO [40]

Table 1-1 Advantages and disadvantages of hierarchical structured ZnO in photocatalytic applications [37]

ADVANTAGES	DISADVANTAGES

NANODOTS	Easily suspended in a solution; large specific surface area	Agglomerates in solution; challenging in recovery of catalyst
NANORODS	Easily growth on most substrates; no post-treatment required	Preparation conditions restricted; Lower surface area compare to 0D
NANOSHEETS	Easily assembled on substrates	Lower surface area
NANOFLOWERS	Good light absorbance; Improved molecular transportation	Preparation process challenging

1.3.3   Architectured Bismuth Oxyhalide (BiOX)

Bismuth oxyhalides, known as BiOX (X=F, Cl, Br, I), with tetragonal crystal structures are often categorised as main group metal oxyhalides. They are chemically stable and environmentally friendly. The crystal structures of BiOX are stacks of two-dimension layered [Bi_2O_2] slabs interlaced with double layer halogen slabs in c-axis direction. Within the layered structured BiOX, interlayers are bonded with weak Van der Waals interaction, while intralayer atoms are connected by strong covalent bonding [41]. The pen-layered structure introduced enough space for polarisation within the materials, which enable an internal built-in electric field between [Bi_2O_2] and [X]. The internal electric field will promote the photoexcited electron-hole separation, which is of great importance in the photocatalytic reactions. Unlike ZnO, which is only active under ultraviolet irradiation, the band gap of BiOX ranging from 1.8 eV for BiOI to 3.3 eV BiOCl enable a certain degree of visible light response. The difference in the band gap of BiOX depends on the electron affinity of the halogen atoms X in the materials, because the valence band maximum (VBM) of BiOX is consisted of O 2p orbitals and X np (n=3,4,5 for X=Cl, Br, I) orbitals and conduction band minimum (CBM) is the contribution from Bi 6p orbitals [42].

Among all BiOX, BiOBr has recently been intensively investigated on account of its exceptional visible-light-responsive photo-catalytic activity and photo-stability. Comparing with BiOCl, BiOBr possessed a smaller electronic energy band gap ($E_{gError!}$

Bookmark not defined.=2.5-2.9 eV), which is suitable for sunlight absorbance. Comparing with BiOI, BiOBr is more chemically stable during the photocatalytic reactions although BiOBr possesses a relative wide band gap. However, the efficiency of solar energy conversion on BiOBr is still too low to meet the demand of industrial application [43]. As a consequence, numerous attempts had been made to further enhance its photocatalytic efficiency and activity. All these approaches can be in three aspects: morphology design, energy band engineering and charge transfer optimization. In particular, morphology and structure design are of priority in the BiOX modification, because morphologies are not only closely involved with synthetic methodology but also determine the specific surface area as well as the light absorbance.

The main synthesis methods for obtaining hierarchical BiOBr include the solvo/hydrothermal, co-precipitation, micro-emulsion, template-assisted and sono-chemical methods. And according to the previous researches, various structures of BiOBr were obtained such as nanoflake, nanowires and mirco/nano pheres. Normally, BiOBr are inclined to form a layered structure due to its intrinsic layer stabbed crystal structures. 3D self-assembled hierarchical BiOBr are favoured for its superior light absorbance and high specific surface area compared to bulky and randomly arranged BiOBr nano-flakes.

Although various chemical methodologies have been implemented to prepare the BiOBr nanostructures, in non-aqueous solvents with assistance of organic templates, the target of creating 3D hierarchical architecture remains tremendously challenging. For example, hydrolysis can lead to poor crystallinity and failure to tune the assembly and morphology of the particles. Micro-emulsion and solvothermal synthetic methods are successful in the formation of 3D assemblies of nanoparticles, though it is time/energy-consuming, and/or environmentally unfavourable. Hydrothermal synthesis may adjust the morphology and crystallinity of BiOBr. Additionally, the assistance of expensive surfactants is prerequisite in fabricating 3D assemblies. All such synthetic protocols can either be energy inefficient, time-consuming or potentially harmful to the environment. Therefore, an attractive tailored synthesis of BiOBr hierarchical nanostructures in more environmentally compatible aqueous solutions, without the use of organic reagents, has yet to be realized.
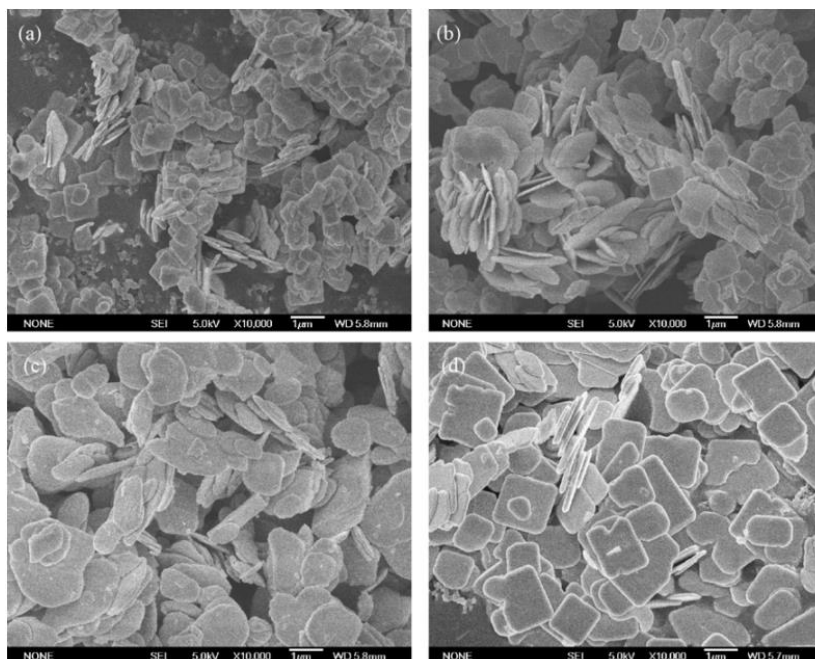
Figure 1-5 SEM images of the microscopic texture of the BiOBr under different heating durations[44]

The super structure, also known as hierarchal structure, has drawn enormous attention, because of its large capacity and developed porosity that unquestionably provides large surface area for the reaction. As a matter of fact, due to its complicated surface and structure, it also has a good mechanical and thermal stability. All these benefits contribute to its great potentials in the solar energy conversion.

During last few decades, there are numerous papers published worldwide discussing the mechanism behind various structures and efficiency promotion. Several theories was proposed to explain the self-assembled structures. Although there are numbers of the patterns available now, the performance did not vary widely between each of them.

1.3.4   Hierarchical CuSCN

CuSCN, a typical intrinsic p-type semiconductor, is optical transparent semiconductor for holes transporting in the electronic devices. CuSCN is a molecular, metal pseudo-halide of cuprous. More importantly, CuSCN is inherently inexpensive to prepare and commercially available [45]. Thiocyanate (SCN) here incorporates as halide ions because it performs similarly to halide ions in the chemical reactions. The physical and chemical properties of CuSCN have been studied since 1950s. With a relatively wide band gap ranging from 3.6-3.94 eV, the optical and electrical properties are often influenced by the synthesis methodology

and the morphology of CuSCN [46]. Depending on different synthesis procedure, CuSCN obtained can exist in two types of crystal structures, the α- and β-phases [47].

The α-phase is orthorhombic lattice, while the β-phase shows hexagonal structure. According to the recent researches, although two-phase coexistence was usually discovered in their CuSCN powders, the deposited thin-films are commonly presented as the β-phase. Its p-type conductivity can be expected if the material is prepared in a solution where the concentration of SCN^- is higher than that of Cu^{2+} [48]. The difference in the concentration of two ions would inevitably create a stoichiometric deficiency of Cu in the lattice, and thus the defect of holes will become the majority of the charge carriers showing p-type behaviour during the photocatalytic process. Meanwhile, the Cu vacancies in the crystal structure will lead to further broadening the optical bandgap and make itself more transparency.

In order to increase the light absorbance of CuSCN, hierarchically structured CuSCN with attenuated light scattering is aimed for preparations. The hierarchical CuSCN has been largely explored materials as superstructures for its widespread applications in the environment and industry. Many morphologies and structures have already been approached in the previous experiments. For example, in Figure 1-6 the hierarchically assembled nanotubes, nanorods, mesoporous and nano-sphere have been frequently reported on numerous papers. These hierarchical structures did not only promote the light harvest efficiency but also increase surface area.

However, the thermal stability of CuSCN hampers its widespread applications in the photovoltaics. The decomposition temperature of CuSCN was reported as 300℃, which much lower than the previous discussed materials such as BiOBr and ZnO [49-51]. To increase the stability of CuSCN, covering with second semiconductor could be efficient method to address the problem.
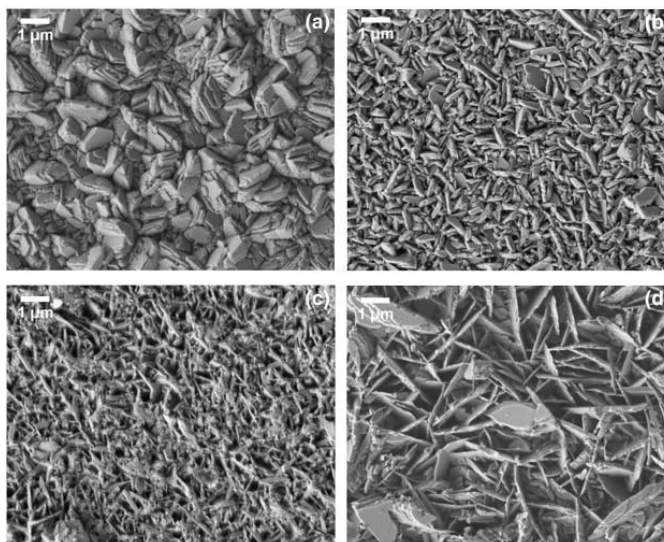
Figure 1-6 SEM images of the hierarchically allied CuSCN nanowires by electrodeposition [49]

1.3.5   Hierarchical heterojunctions

Heterojunctions are the interface between two dissimilar semiconductors. These semiconducting materials have unequal band gaps as opposed to a homo-junction. It is often advantageous to engineer the electronic energy bands in many solid-state device applications including semiconductor lasers, solar cells and transistors. The hetero-junctions which are defined bearing different band structures will contribute to promote photo-catalytic conversion efficiency. The charges excited by the light will largely de-trapped because the electrons and holes will be separated by the heterojunction due to built-in electric field across the interface. In fact, it is the existence of the potential difference in each side of the crystalline semiconductor that provides the oriented path for the charges in the reactions. In this way, the recombination of charges can be reduced to some extent.

As for photocatalysis process, coupling with second semiconductors are preferable in several applications, because of their higher light absorption, better suppression of photoinduced electron/hole pair recombination and increased charge separation. Lin and Chiang [52] have shown that the increased charge separation was due to an extended lifetime of charge carriers by inter-particle electron transfer between the conduction bands of nanocomposites leading to a larger number of electrons involved in a photo-degradation reaction. These superior properties are ascribed to a stepwise energy-level structure in the composite. Another similar study by Nur Johra. has also shown that highly active photocatalysts can be obtained by coupling two semiconductors having different band gaps [53]. Based

on their proposed mechanism, relatively efficient charge separation may be achieved due to photoinduced electrons that are transferred away from the photocatalyst. Therefore, the heterostructure of nanocomposites serve as an attractive alternative for enhancing the photoactivity of photocatalysts.

Figure 1-7 illustrates the process occurred on the hetero-junction photo-catalysts. Once the light strikes the surface of the hetero-junction, the photo-induced charge will be separated by the energy difference of each side, where the electrons will be introduced to the TiO_2 and the holes will be transferred to the valence band of the ZnO. In this way, the recombination of electrons and holes could be remarkably confined into the small space[16].
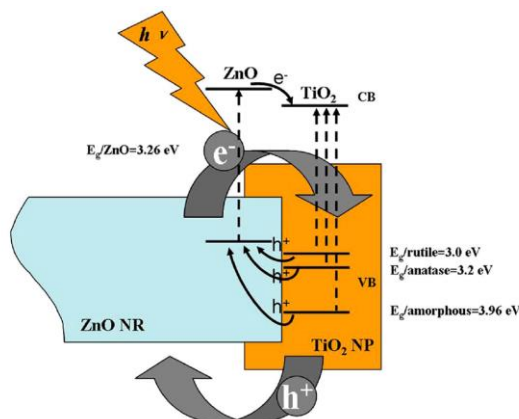
Figure 1-7 Charge transmission path in the hetero-junction photo-catalyst [38]

1.4   Materials synthesis

1.4.1   Introduction

The previous discussion demonstrated the importance of hierarchical structure in light absorbance and photocatalytic performance. Multi-dimensional self-assembled of nano/micro-crystal photo-catalysts generally outperform both their nanoscale constituent building blocks and their corresponding bulk materials in important applications, such as photo-catalytic environment remediation, solar fuel generation and solar energy harvesting. The photo-response and photo-catalytic performances of the assemblages are closely related to their intrinsic high surface-to-volume ratio, facile transportation of the reactants, anti-recombination process and the property of easy recycling.

To date, dozens of photocatalysts with various morphology had been successfully designed and prepared. Numerous attempts had been made to obtain hierarchically structured photocatalytic materials. The deposition, sputtering, anodizing and

hydrothermal synthesis are mostly used in the material preparation. For its dedicated patterns in the structure, the preparation should be carefully designed and carried out.

However, it is accepted that assembling such structures from finite-scale crystals represents a thermodynamically non-spontaneous process with a significant reduction of the system entropy and consequently necessitates either additional energy input or special reagents to improve or catalyse the nucleation, growth and elaborate assembly of the constituent blocks. The special regents employed in the synthetic preparation are generally functioned as surfactant or template to reduce the surface energy and coordinate the crystal growth in the materials synthesis. In the past decades, exploring new chemical synthetic methodologies with the aim of reductions in time and energy consumption has become a great concern for the society of human beings.

1.4.2   Hydrothermal (HT) synthesis

Hydrothermal synthesis can be defined as a method to synthesis single crystals that depends on its solubility in the solution under pressure [44]. Nowadays, this kind of method has already been widely employed into crystal growth for it can produce a crystal in good morphology at a relatively low cost. As for preparation of the hierarchical materials, the hydrothermal technique exhibits its advantage in the massive production. In the hydrothermal synthesis, usually there are precursors and template reagent or surfactant reagent in the autoclave. Those materials are put into the closed reactor in sorts of sequence. After loading the chemicals, the reactor is put into the oven for the heating treatment. After that, there will probably be calcination or annealing to tune up the crystallinity of the materials. In order to obtain some particular structure morphologies, the temperature, the pressure inside autoclaves and composition of the solutions should be carefully controlled and manipulated. Although a number of photocatalysts have been reported to be successfully prepared in hierarchical morphologies by the hydrothermal synthesis, yet this technique is still limited by the solubility of the materials and chemical properties of template reagents [20, 54, 55]. Hydrothermal synthesis could be powerless when some minor modification needs to be made in some nano-scale structures.

The advantages of hydrothermal synthesis are the capability to prepare the materials which are not stable of at their melting point. However, the completely

closed autoclave makes it impossible to observe the growth of the materials in the chamber.

1.4.2.1   Template assisted HT-synthesis

In the hydrothermal synthesis, sometimes the designed patterns would be a quite intractable problem without any assisted facilities. Consequently, template agents are required in these cases. The template acts as the mould in hydrothermal synthesis where it could be the aggregation centre and growth director in the reaction process. Mostly these template agents can be categorized into two groups, namely hard template and soft template. For metal oxides hierarchical structures, such as TiO_2, ZnO and BiOBr, the super structures can be produced via precipitation between the metal salts and ammonia [56, 57]. The surfactants such as cetyl trimethyl ammonium bromide (CTAB), polyvinyl-pyrrolidone (PVP), tetra butyl ammonium bromide (TBAB) and block co-polymers P123 are most widely used in the hydrothermal synthesis [58-60].

For example, Figure 1-8 displays a two-step surfactant assisted method to obtain the hierarchical structure in the ZnO. Firstly, long chain *N*-acyl amino acids were prepared from the reaction of lauroyl chloride with acidic amino acids in a mixed solvent of water and acetone. The prepared surfactant plays a significant role in governing the hierarchical structure through an explicit and implicit control. It is worth noting that in their work two amino acid with carboxylic group were introduced in the experiment. As non-polar amine acid, alanine was applied to cause a gradual variation in the structure of the molecular. This solvent study shows that the determination and the use of ideal solvent are important steps to obtain desirable structures, as changes in solvent system can induce a preferential enlargement of either hydrophilic head groups or hydrophobic tail groups and change the packing parameters of surfactant molecules during micelle formation, which eventually transform the macroscopic morphologies of ZnO assemblies. The selection of surfactant will make influence not only on the morphology of the materials, but also on the composition and crystallinity.
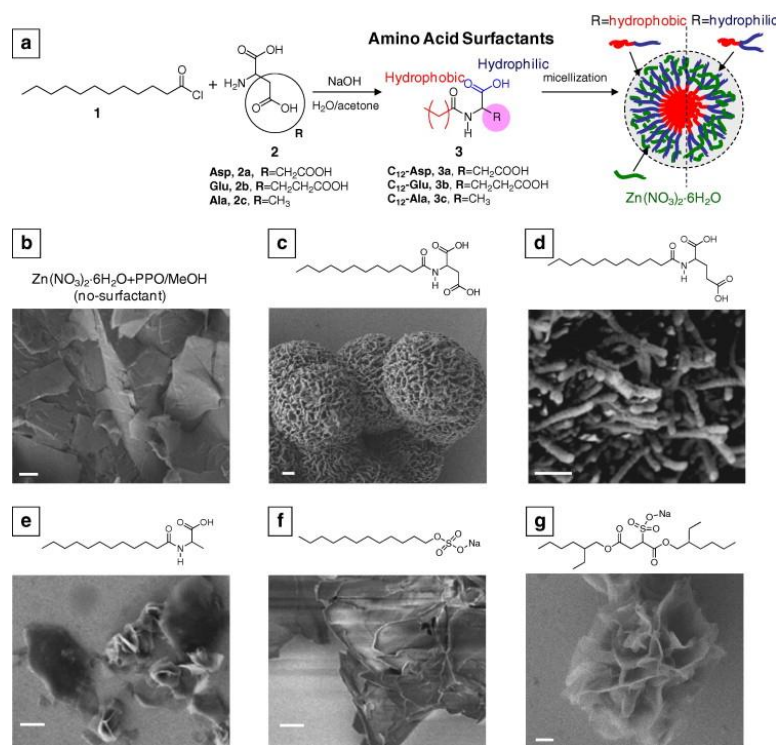
Figure 1-8 SEM images of ZnO precipitates obtained from methanol solutions of Zn (NO$_3$)$_2$·6H$_2$O and surfactants with varying degrees of hydrophobic/hydrophilic ratios [58]

Another category of templates used in the synthesis of hierarchically structured metal oxides are hard templates, which have a pre-set morphology and porosity which allow the reverse duplication of their structure. Commonly used hard templates include carbon materials and silica. The general procedure for hard template methods is to fill the void pores of the template with the metal oxide precursor, followed by converting the metal oxide precursor to its corresponding metal oxide, and finally remove the hard template by chemical etching or via combustion. Obtained metal oxides are a reverse image of the initial hard template. The key issue of all hard template methods is the design of the hierarchical structure within the hard template in the first place[61].

Error! Reference source not found. illustrates formation of hierarchical BiOI from the work of Xia et al. They had developed an ionic liquid (IL) -assisted solvothermal approach to make different porous or hollow BiOX microspheres [62-65]. Applying 1-butyl-3-methylimidazolium iodine ([Bmim]I), uniform hollow BiOI microspheres with holes on the surfaces were prepared [62]. They displayed improved photocatalytic activity for the degradation of MO (180 min, 92%) under visible-light irradiation compared with 2D BiOI nanoplates (180 min, 21%). During the formation process, the IL not only served as the iodine source but also as the solvents and templates for the fabrication of hollow BiOI microspheres. Changing the type of IL

from [Bmim]I to [C16mim]Br enabled BiOBr hollow microspheres to form using a similar solvothermal process [63]. The IL cation of [C16mim]$^+$ has a longer alkyl carbon chain than [Bmim]$^+$. This long carbon chain can better prevent or delay crystal growth, as confirmed by time-dependent scanning electron microscope studies. After the PVP surfactant was introduced to combine with the IL [C16mim]Br, BiOBr porous nanospheres were formed. The PVP+IL complex system exhibited better control over crystal growth. The synergistic effects of the high BET surface area, energy band structure, smaller particle size, and good light absorbance of BiOBr porous nanospheres contributed to their improved photocatalytic activity for RhB degradation under visible light irradiation compared with BiOBr hollow microspheres.
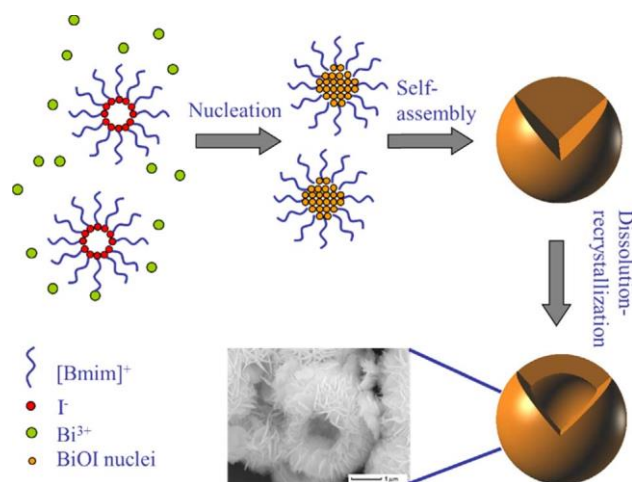
Figure 1-9 Schematic illustration of the formation process for BiOI hollow microspheres [66].

1.4.2.2 Template-free HT-synthesis

The template-assist strategy usually consists of two steps: the surface coating of template with materials and template removal. Despite the two-step process has been widely applied in the preparation of complex hierarchical structures, template removal by calcination or etching is generally costly and far from the idea of "green chemistry". In contrast, one-step template-free synthesis can effectively avoid the problem. Instead of utilizing the template agents, the template-free preparation is inclined to exploit the reaction mechanism in order to modify the shape of the hierarchical materials during the experiments. Ostwald ripening, coordination, hydrolysis and selective corrosion are usually proposed to explain the formation of the hierarchical structures in the materials[67].

In the preparation of 3D hierarchical BiOX, template-assisted hydrothermal method are usually considered as an effective approach to construct porous or flower-like

structure [14]. The existence of template agent in the solution, such as ethylene glycol (EG) or polyethylene glycol (PEG), will facilitate the coordination of Bi^{3+} to yield the alkoxide complexes so as to slow growth rate of BiOX into nanoflakes [68]. As shown in Figure 1-10, self-assembly of nanoflakes is induced by the viscosity and gradually form the 3D hierarchical structure under the guidance of the template. All of the BiOX microspheres were photocatalytically active, and BiOX displayed better photocatalytic activity under both UV–vis and visible-light irradiation. Another work from Xiong et al. had prepared flower-like BiOCl hierarchical nanostructures by directly reacting metallic Bi nanospheres with an $FeCl_3$ aqueous solution at room temperature. The flower-like BiOCl hierarchical nanostructures displayed higher photocatalytic performance for the degradation of RhB than did commercial BiOCl materials [69].
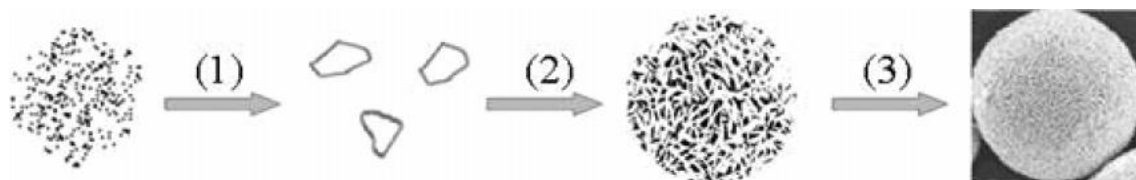
Figure 1-10 (1) Formation of BiOX nanoparticles and their growth into nanoplates at the early stage. (2) EG-induced self-assembly of these primary nanoplates to form loose microspheres. (3) Formation of regular hierarchical microspheres through a dissolution-recrystallization process of the preformed nanoparticles [56].
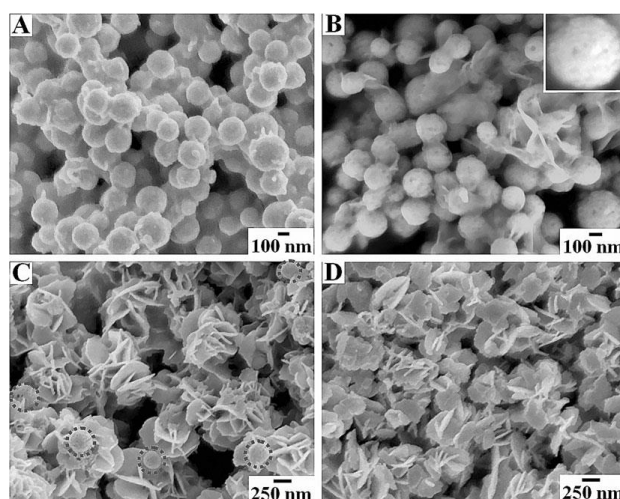
Figure 1-11SEM images of $BiOCl/FeCl_3$ prepared with different amounts of $FeCl_3$ [69]

However, the hydrothermal synthesis is difficult to control the parameter during the process, because the entire process is taken place in an enclosed container. Therefore, in order to ensure a good quality of the product, some measures should be taken to improve the process. In this case, a carefully designed experiment will be desperately required if a complex morphology is expected in the result.

Currently, it has been reported that the hierarchical nanotubes, nanosheets, nanorods and cubes were successfully obtained through the hydrothermal ways. And lots of mechanisms of the formation of the superstructures were proposed by numbers of research groups. According to their explanation, the morphology could be largely affected both in the reaction and post-reaction procedures. For example, in the nanotubes, the explanation is that during the acid washing process, the electrostatic repulsion is removed by the acid solution, which results in the assembly of the nanotubes[70]. The further details could be found on. Besides that, Ostwald ripening and oriented attachment also leads to its formation of hierarchical nano-flakes[71].

1.4.3   Deposition

Deposition and sputtering are also considered to be efficient approaches to obtain the hierarchically structured materials. However, these methods would probably need a series of facilities to support for the sake of carrying out our plan. In the deposition synthesis, chemical vapour deposition (CVD) or metal organic chemical vapour deposition (MOCVD) are often used in the paper to realize the structure building [32, 72]. Due to its high vacuum and high temperature inside the chamber, a very thin layer of materials could be deposited onto the substrates, above which pure gases from various resources are injected into the reactor. The surface reaction between the organic molecular and metal organic compounds makes hydrides to form multilayers semiconductor. In the Metal Organic Chemical Vapor Deposition (MOCVD) technique, reactant gases are combined at elevated temperatures in the reactor to cause a chemical interaction, resulting in the deposition of materials on the substrate[73].

In spite of its precision and versatility, the staggering cost of the equipment and complicated operation inevitably will curb its application in the large-scale preparation. As a result, it seems more approachable to seek alternatives way from high cost deposition.
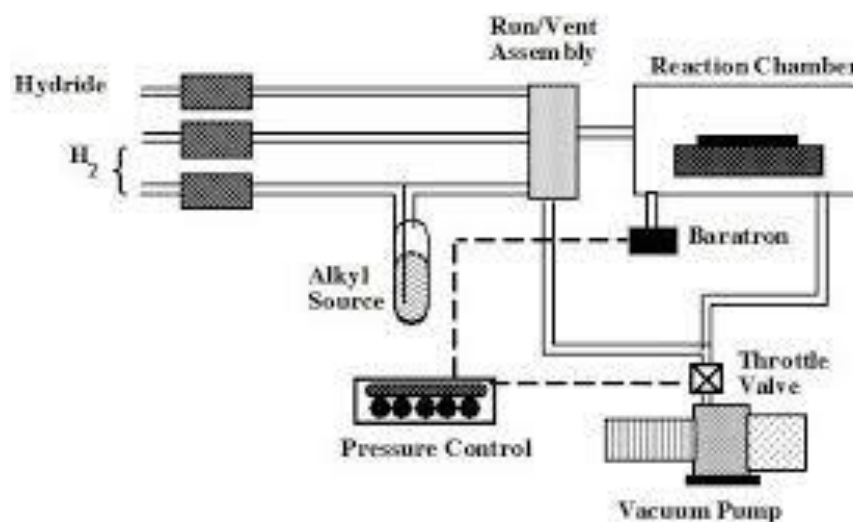
Figure 1-12 The image shows the deposition process and required instrument [74]

However, deposition exhibits unparallel advantage over hydrothermal and co-precipitations. Especially for large-area films making and temperature sensitive materials preparation, deposition can effectively control the growth parameters (pressure, rate, temperature, etc.) and thus avoid the thermal degradation of the materials. Meanwhile, deposition process is also able to deliver a rapid and quality product comparing with hydrothermal synthesis.

For instance, CuSCN, as mentioned above, is a promising candidate for a series of photocatalytic reactions. CuSCN preparation process requires a careful control on the ratio between Cu^+ and SCN^- and the temperature during synthesis, which is beyond the capability of CVD or PVD methods. However, the electrochemical deposition may effectively overcome this problem.
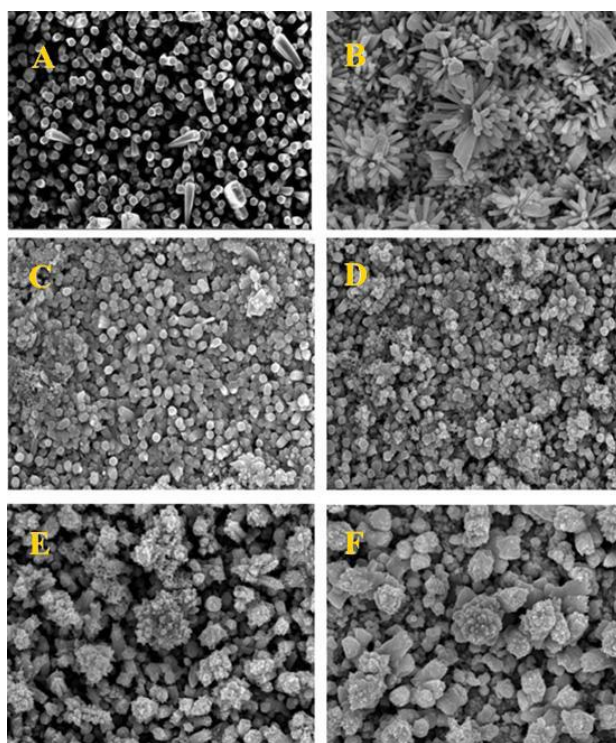
Figure 1-13 SEM images of the CuSCN films deposited at (A) -0.30 V, (B) -0.31 V, (C) -0.32 V, (D) -0.35 V, (E) -0.40 V (F) -0.42 V [49]
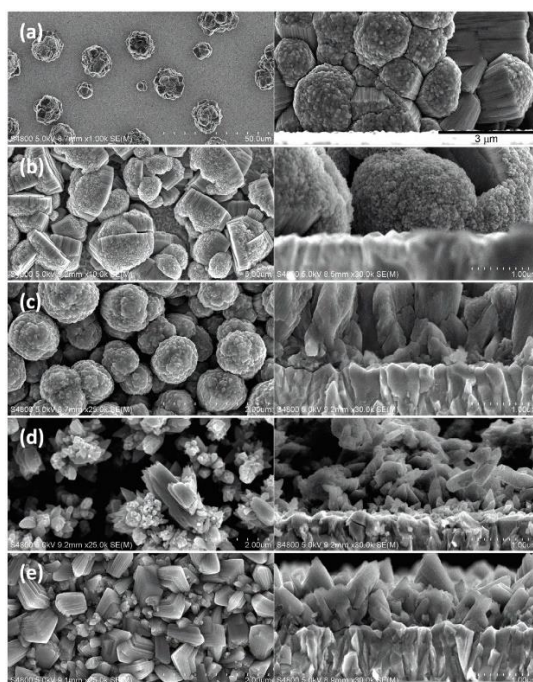
Figure 1-14 SEM photographs for surface (left) and cross-section (right) of CuSCN thin films electrodeposited from ethanolic solutions containing Cu^{2+} and SCN^- in ratios of (a) 1:5, (b) 1:3, (c) 1:2, (d) 1:1 and (e) 3:1 [75]

As shown in Figure 1-13 and Figure 1-14, the SEM images exhibit the various morphologies of CuSCN prepared under different conditions. In order to identified best synthesis conditions, Ghosh and Sun et al. have explored the influence of

different potentials bias and Cu$^+$/SCN$^-$ ratios on the morphology and crystallinity of CuSCN [75, 76]. The morphology of the deposited thin films was tuned from nanorod structure to granular ones by variation of the applied potential in the range of -0.3V to -0.42. Crystalline rhombohedral CuSCN phase was attained in this potential range. Additionally, in order to obtain the nanorods array, the ratio between Cu$^+$ and SCN$^-$ should be kept at 1:2, because the high concentration of thiocyanate ions creates stoichiometric deficiency of Cu in the solid and Cu vacancies in the materials will contribute to the p-type behavior of CuSCN [45, 46, 48].

Anodizing, generally, is electrolytic passivation used to coating oxidation layers onto the metal component. At first, anodizing was used to prevent the galling between the threaded metal components. Then people had realized that it could increase the adhesion between the coating layers and film. As a result, anodizing has been applied to fabricate the electrode in the super capacity and dye sensitized solar cells (DSSCs) because it can bring well-ordered meso-porous or tubular patterns on the surface of the materials which are attached to the substrate[77]. In the DSSCs, these super structures provide enormous surface area for the reaction and simultaneously the porous structure absorbs the dyes onto surfaces. Undoubtedly, the photovoltaic reaction will be accreted and added interference to the projected light, although sometimes brittle [78]. However, in order to obtain well-assembled hierarchical materials, experimental conditions such as electrolyte concentration, acidity, solution temperature, and current should be carefully controlled.

The nature of electrolyte employed for the development of materials strongly influences the formation of the graded structure. It was well recognized that under the same conditions, different electrolytes may produce different electric field intensities. For example, the electric field in the binary electrolyte is quite different from that of multiple-electrolyte [79].

In addition, it was also well known that in the initial stage of anodization, the higher electric field intensity can induce bigger breakdown sites which finally result in wider diameter of the particles [80].

TiO$_2$ is a chemically stable photocatalyst with outstanding performance in wide range of area. However, the stability of TiO$_2$ lead to limited methods for morphology engineering. Recently, a series of research has been carried out to

explore the feasibility of structure modification of TiO_2 via anodization [81]. The SEM images displayed in Figure 1-16 and Figure 1-17 shows the morphologies of TiO_2 corresponding to the different anodising conditions. According to the results form Sreekantan et al., the favoured synthesis condition governed morphologies of TiO_2 nanotubes, which will further determine the overall performance of the materials [82, 83]. in their work, the synthetic conditions were carefully compared, yet the relationship between synthetic conditions and morphologies was not clarified in their work. Thus, more detailed experiment is expected to explain the mechanism on the fabrication of TiO_2 nanotubes.
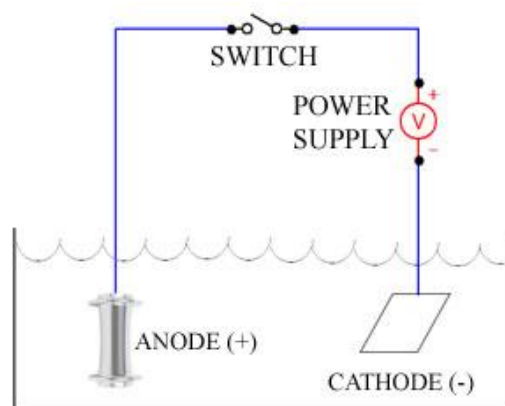
Figure 1-15 Basics in the anodizing synthesis. Usually there are two electrodes. Surface of the anodes in most cases are the target area for the hierarchically assembly. Cathodes are usually made of platinum or titanium in the system [84].
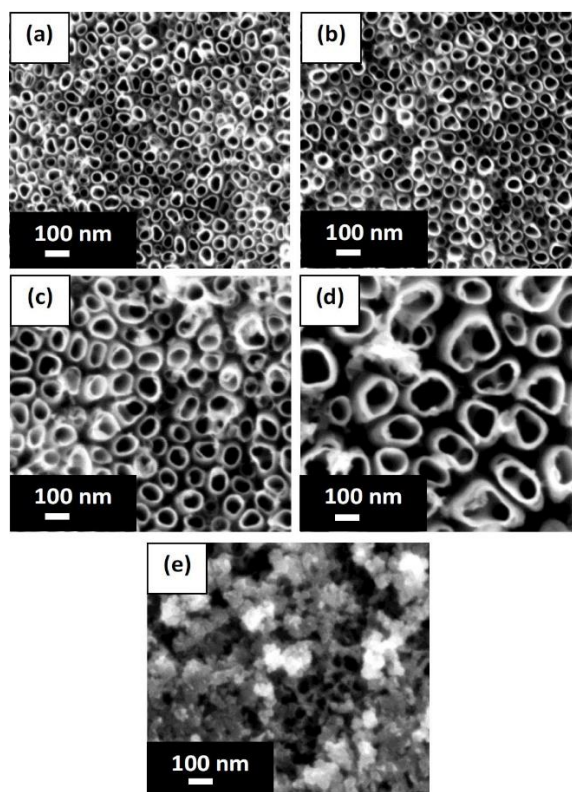
Figure 1-16 FESEM images of TiO₂ nanotubes formed in glycerol + 6 wt% EG + 5 wt% NH₄F at (a) 20, (b) 30, (c) 40, (d) 50, and (e) 60 V [81].
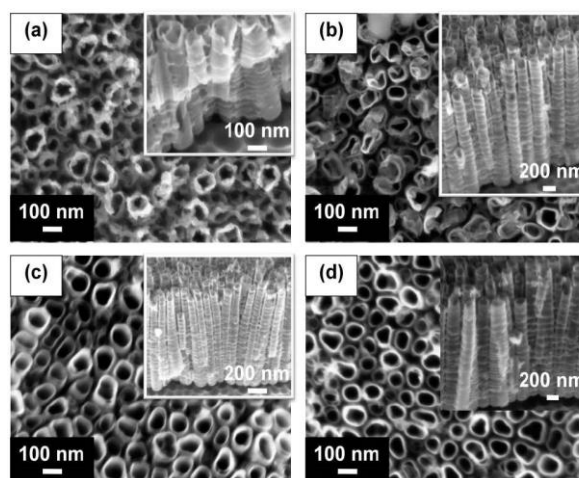
Figure 1-17 FESEM images of TiO₂ nanotubes formed in glycerol + 6 wt% EG + 5 wt% NH₄F for anodization times of (a) 1, (b) 15, (c) 20, (d) 30, (e) 180, and (f) 360 min [82].

1.4.4 Ink-jet Printing

Ink-jet printing is an emerging approach to obtain the hierarchical structure. This idea was generated from the solid freeform fabrication, which also give birth to the well-known three-dimensional (3D) printing [85]. Some of the scientists believe that introducing this technology into the synthesis of solar energy conversion materials

would deliver an un-expectable result. Printing could deposit various materials onto the substrate via the nozzle in the printer. Actually, printers in the most published papers are modified from our daily used printers. Generally, there are two types of ink-jet printers applied to this area [32]. One is continuous printer and the other is called drop-on-demand (DOD). In the continuous printers, the liquid ink is directly pumped from cartridges onto the papers or plate through a nozzle in the gun body. The stream of the liquid ink is break into numerous pieces by a piezoelectric crystal in the nozzle, which will vibrate at a controlled interval given by the outside researchers. However, most consumer inkjet printers are DOD, where some heating components and piezoelectric materials are employed. In DOD system, the heating process creates a series ink bubbles that finally drop on the papers.

In spite of its simplicity and efficiency, inkjet printing is also challenged by some of its defects. The viscosity of the liquid, size distribution of the drop and the property of the particle inside are most frequently concerned issues in the experiment design. Due to the exquisite patterns within our aimed structure, the size of the drop should be restricted to a smaller diameter compared to our daily use. As a result, the nozzle would be modified according to our demand. Usually, the diameter of the nozzle is 40-100μm and the drops of liquid ink will extend no more than 1mm on the target [13].

In fact, ink-jet printing usually displays limited capability in the preparations of super structured photocatalysts. Several researches have already claimed their success in fabrication of the hierarchical materials via ink-jet printing. The research work from černá shown in Figure 1-18, TiO_2 was deposited on soda-lime glass via ink-jet printing process [86]. Although TiO_2 coating layers were homogeneous, compact without any crack, morphology quality of TiO_2 is inferior than the TiO_2 prepared from template-assisted hydrothermal synthesis [87].
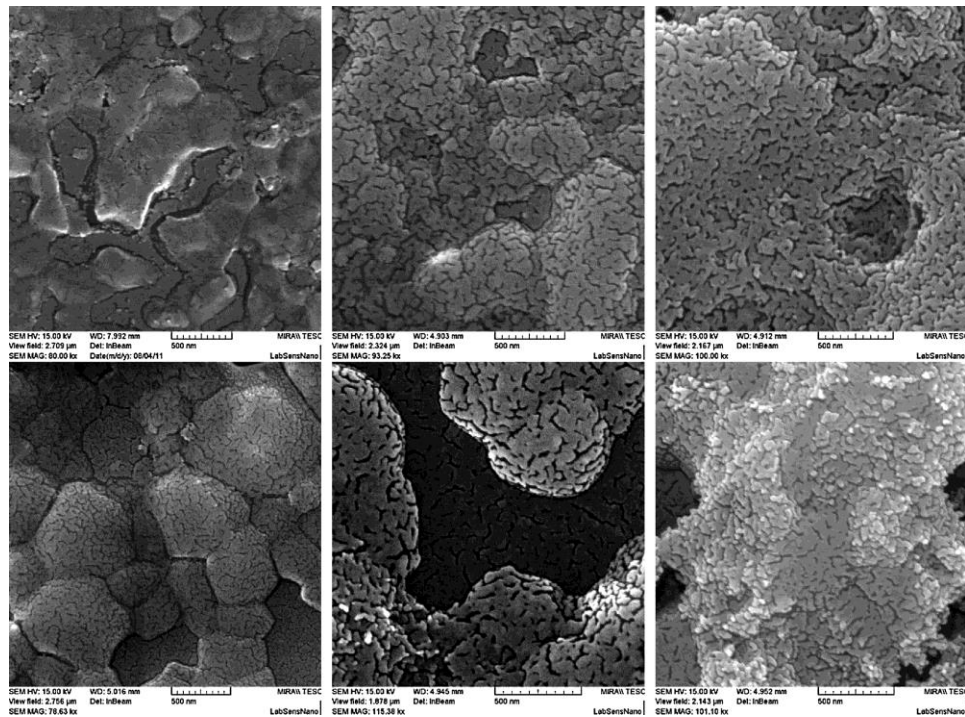
Figure 1-18 SEM images for one-layer samples of TiO_2 synthesized at 110 ∘C (top) and 160 ∘C (bottom) for different time; 6 h (left); 24 h (middle); 48 h (right) [86]

1.5 Energy-band engineering

The energy band or electronic band structure of solids describes the ranges of the energies that the electrons in the materials may have (called energy band) and ranges of the energies that the electrons may not have (called band gap)[88].

Also, the light absorption and structure patterns will have influences on the light conversion efficiency. The surface morphology will determine the light quantity through the materials. As a matter of fact, once the light reaches the surface of materials, it will scatter or reflect from the surface. Some go in, some scatter away. To ensure a plenty of luminous flux, there is a need for a reengineering of the morphology and surface to a well-ordered assembly structure. These kinds of structures would scatter the light within the materials so that the light will be trapped into the materials. Inevitably, the absorption of the light would dramatically increase in this way [89].

Moreover, the enhanced structures would strengthen the mechanical property and thermal stability for the reason that the complexity of the structure could endure much more stress and heat compared with the normal structures. At the same time,

the dimension level and size of the structure patterns would affect the recombination in the materials. These details provide more choices for the charge transmission. In order to reduce the recombination, bulk materials could be shape into Nano sized materials, which will shorten the transmission path of the charge.

1.6 Charge transportation optimization

Charge transportation or precisely charge separation and transportation is of vital importance in the entire photocatalytic process, which ensure plenty of charge taking place in the photocatalytic reactions [89]. When electrons in a filled valence band (VB) are excited into a vacant conduction band (CB) by a photon of energy greater than the energy of a gap between the VB and CB, a band gap, to give a photo-excited electron (e−) and a hole (h+) in the CB and VB, respectively. These species, i.e., charge carriers, in the CB and VB reduce and oxidize substrates adsorbed on the photo-catalyst surface, respectively, or they recombine with each other and disappear without leading to any chemical reaction. If the recombination goes too fast, it will undoubtedly compensate the amount of charge carriers in the reaction area where oxidation and reduction highly depend on participation of these charge carriers. Therefore, the reducing charge recombination in photo-catalysts can be one solution to improving the efficiency of the photo-catalysts[90].

Inspired by the function of Mott-Schottky barriers, separating charges in the semiconductors, selective metal loading on the photocatalytic materials will also work on the photo-catalysts. When the metal loaded onto the photocatalytic semiconductors, a metal-semiconductor (M-S) junction is form in the surface [91]. The junction itself can be rectifying or non-rectifying. The rectifying M-S junction forms Mott-Schottky barrier, while the non-rectifying M-S junction is called ohmic contact. Whether it is an M-S junction or ohmic contact depends on the height of the Mott-Schottky barrier, Φ_B, shown in Figure 1-19 [30, 92, 93]. If the barrier is significantly large, then the semiconductor will be depleted in the junction and form a Mott-Schottky barrier. While for the lower barrier, the junction will therefore form ohmic contact instead [94].
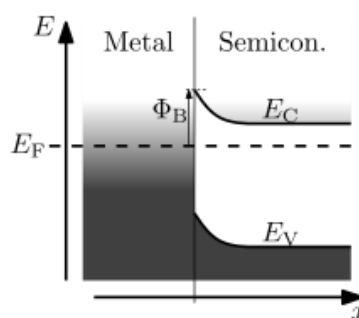
Figure 1-19 Band diagram for Metal-Semiconductor junction at zero bias [94]

Due to existence of the energy barrier in materials, the excited electrons on CB are incapable to overcome the barrier to get to the metal, while the positive charge transfers to the metals. Therefore, the photo-induced charge carriers are able to be separated by the barrier which consequently reduces the rate of the charge recombination [95].

Utilizing advantage of the depletion zone in the junction, Mott-Schottky barrier can also be applied in the semiconductor-semiconductor (S-S) junction as long as two kinds of materials are in different band structure. In the heterojunction shown in Figure 1-20, two kinds of semiconductors join together and probably perform more than sums of the parts [96]. Apart from promoting charge separation, coupling semiconductors with different gaps can also enhance the light absorption, promote the surface reaction kinetics, and thus improve the photocatalytic efficiency [97].
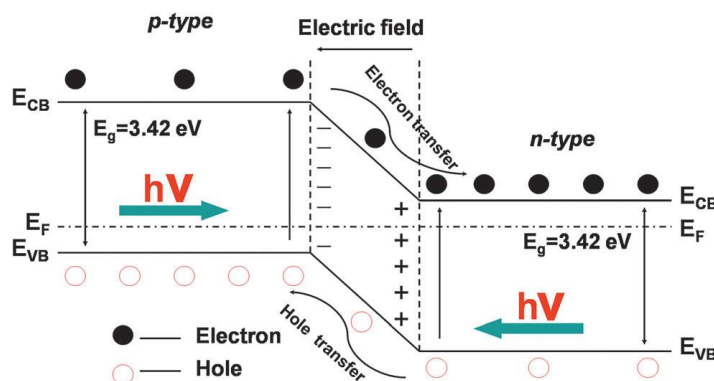
Figure 1-20 Schematic diagram showing the energy band structure and electron-hole pair separation in the heterojunctions [3]

Generally, the S-S heterojunctions can be divided into two kinds of group: p-n heterojunction and non p-n heterojunction. Among these, construction of carbon-semiconductor (C-S) could be a promising way in the future. Carbon fibres, with large surface area, are typically used as the structure or support of the photocatalytic materials [98]. In the practical test published, the increase of the surface area leads to a remarkably promotion in its photocatalytic activity [99],

which can be explained according to the Langmuir-Hinshelwood mechanism. Therefore, it can be expected the performance of photo-catalysts will be upgraded on account of the combination of the carbons and semiconductors [3, 100].

To date, a large number of important papers have been published on the design of hierarchical photocatalysts with multiple porous structures and enhanced efficiency [101-103]. Although excellent reviews devoted to hierarchical semiconductors such as ZnO, BiOBr and TiO_2, only a handful topics referring to their energy band contributions and applications in photocatalysis and photoelectrochemistry has been apprised. Thus, I believe that a comprehensive and intensive research on this subject is timely to promote further developments in this critical, exciting and still emerging area of research.

In this project, we thoroughly discussed the influence of hierarchically nanostructured semiconductors on various photocatalytic applications. A special emphasis is directed toward better understanding of the design, fabrication, performance and applications of hierarchical semiconductor photocatalysts. Also, various applications of hierarchical photocatalysts for degradation of pollutants, air purification, H_2 production, and CO_2 reduction, and future research challenges are discussed.

Chapter 2 Experimental Characterisation

2.1   Compositions and Structures

2.1.1   Powder X-ray Diffraction

X-ray diffraction (XRD) yields the atomic structure of materials. It is based on the elastic scattering of X-rays from the electron clouds of the individual atoms in the system. Powder X-ray Diffraction is a technique used to characterize the crystallographic structure, crystallite size, and preferred orientation in poly-crystalline or powder samples. Powder diffraction is commonly used to identify unknown substances, by comparing the XRD pattern data with a database maintained by the International Centre for Diffraction Data. Powder diffraction may also be used to characterize heterogeneous solid mixtures to determine relative abundance of crystalline compounds [104].

The planes of atoms are labelled with a set of integers (h, k, l), called Miller indices, which identify the reciprocals of the fractional intercepts, which the plane of interest makes with crystal axes. For cubic crystal the distance dhkl between adjacent Bragg planes is

$$d_{hkl} = a \frac{1}{\sqrt{h^2+k^2+l^2}} \tag{1}$$

When a beam of X-rays interacts one of the atoms in the crystals, the X-rays are diffracted in all directions. In general, these diffracted waves from different atoms will be, on average, out of phase and cancelled out. However, for an X-ray wavelength λ and the angle of incidence θ with respect to Bragg plane, scattered waves from various ions lying in a single Bragg plane will be coherent if the angle of reflection equals the angle of the incidence, as shown in the Figure 2-1 Scattering in this direction from successive planes a distance dhkl apart will be coherent, and will interfere constructively if

$$n\lambda = 2d_{hkl} \sin\theta \tag{2}$$

Where n is integer, and this equation is also known as the Bragg Law of diffraction. Thus the diffracted beam makes an angle θ with the Bragg plane and the angle between the incident beam and the diffracted beam is 2θ [36].
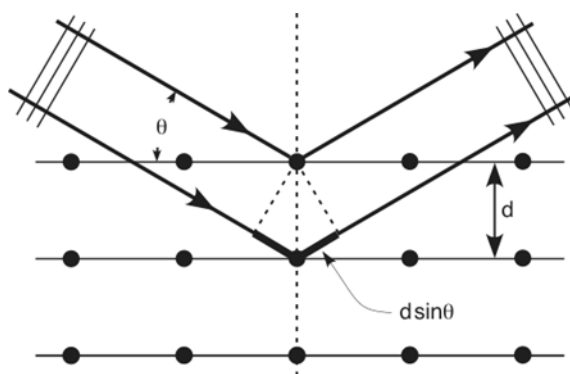
Figure 2-1 Illustration of condition required for Bragg diffraction [105]

2.1.2 X-ray Photoelectron Spectroscopy (XPS)

X-ray photoelectron spectroscopy (XPS), also known as Electron Spectroscopy for Chemical Analysis (ESCA), is a quantitative spectroscopic technique that measures the surface elements composition and the chemical and electronic states of the elements. It also characterizes the valence band structure that exists within the material. Generally, XPS spectra are obtained as plot of the number of detected electrons by irradiating a material with a beam of X-ray while simultaneously measuring the kinetic energy of the electron emitted from top 1 to 10 nm of the material being analysed. It is a surface-sensitive technique when implemented to the solid materials. The X-rays employed in XPS penetrate a substantial distance into the sample. This method of excitation imparts no surface sensitivity at the required atomic scale. For instance, electrons of a given energy, E_0, are emitted from atoms in a solid at various depths, d, below a flat surface. Only those electrons which reach the surface and at the same time leave the solid still have their initial energy (E_0) and can be detected. This is not literally true in an XPS experiment, but in XPS experiment it is only those photoelectrons, possessing characteristic emission energies and contributing to the peaks, will be considered in the subsequent analysis. Photoelectrons, which have lost some energy and contributed to the background of the spectrum rather than a specific peak, are not considered [106].
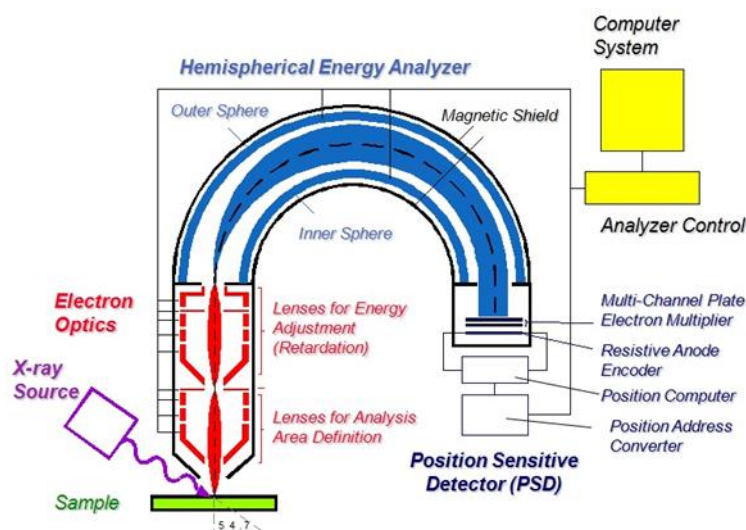
Figure 2-2 Illustration of the XPS instrumentation [107]

The process by which an electron can lose energy as it travels through the solid is known as 'inelastic scattering'. Each inelastic scattering leads to a reduction in the electron energy and a change in the direction of travel. Apparently if the source atom is closer to the surface, then a greater fraction of the emitted electrons will be detected since there will be less chance of inelastic scattering before it escapes from the solid. Therefore, the surface sensitivity must arise from the emission and detection of the photo-emitted electrons. The chemical state information obtained with XPS includes oxidation states and hybridization states for chemical bonds of elements. Application of peak fitting routines is generally required to distinguish peaks from overlapping oxidation or hybridization states [108].

Fermi level (EF) is the highest energy level occupied by an electron in a neutral solid at absolute 0 temperature. Electron binding energy (BE) is calculated with respect to the EF [90]. The core electrons are local close to the nucleus and have binding energies which are characteristic of their particular element [94].
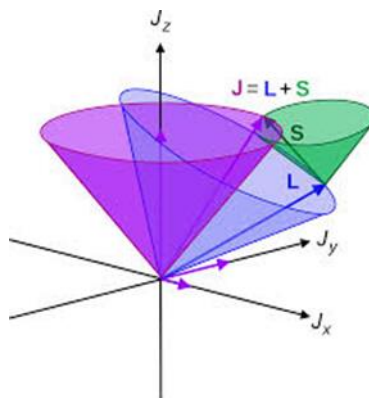
Figure 2-3 Schematic of spin-orbit splitting[109]

.

2.1.3   Scanning Electron Microscopy (SEM)

Scanning electron microscopy (SEM) provides information about the surface topography. And with help of EDX, composition of the materials can also be analysed in the SEM. The most common mode of detection is via analysis secondary electrons emitted from atoms excited by the electron beam. On a flat surface, the plume of secondary electrons is mostly contained by the sample, but on a tilted surface, the plume is partially exposed, and more electrons are emitted. By scanning the sample and detecting the secondary electrons, an image can be created to display the topography of the surface [110].

In my project, SEM was performed to investigate the surface morphology using JEOL JSM-6301F Field Emission SEM at an accelerating voltage of 10kV-15kV.

2.2   Optical Properties Characterisation

2.2.1   Ultraviolet-Visible spectroscopy

Ultraviolet-visible spectroscopy also known as absorption spectroscopy or reflectance spectroscopy in the ultraviolet-visible spectral region, which means it uses light in the visible and near-infrared ranges. The absorption or reflectance in the visible range directly affects the perceived colour involved of the sample material, in which molecules or continuous solids undergo electronic transition from the ground state to the excited state. Usually, the According to basic optical theory, the absorbance, reflectance and transmittance of the light can be correlated by using the equation below.

$$Absorbance\ (\%) + Reflactance\ (\%) + Transmittance\ (\%) = 1 \qquad\qquad (3)$$

UV-Visible spectroscopy is very useful for exploring the optical and electronic properties of materials, including light semiconductors and hydrid materials for the solar energy conversion. In this project, this technique has been utilized to characterize the photo degradation extent of the liquid organic dye pollutants, and also the solid samples used for characterizing the absorption ability and electronic band gap energy [33].
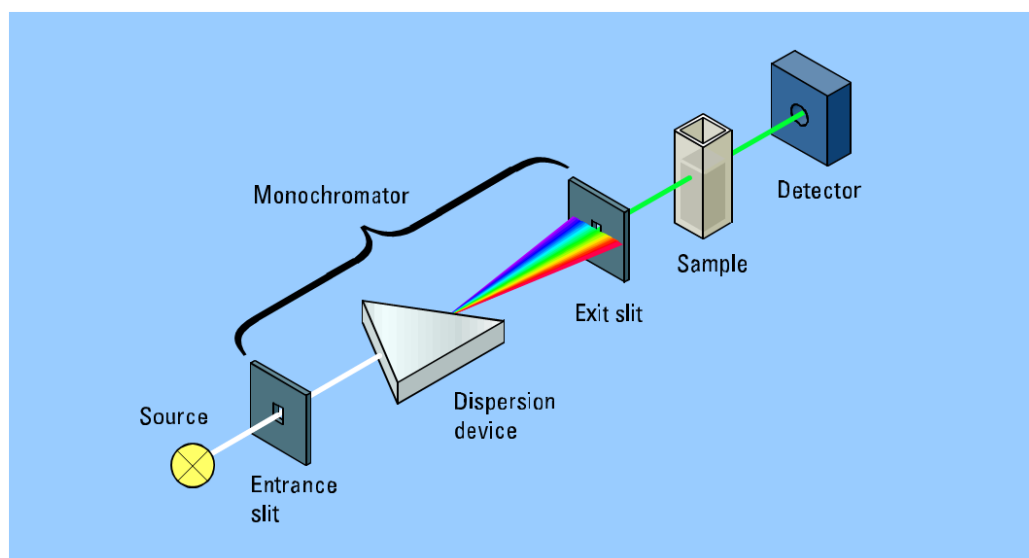
Figure 2-4 Working principle of the UV spectrometer [111]

2.2.2　Fluorescence spectrometer

The fluorescence is a result of three-stage process happens in some materials. The first stage is similar to the photo-catalysis process. Photons in the energy of hν are supplied by light source for example incandescent lamp and strike on the surface of the materials, creating an excited electronic state. In the excited electronic state, the electrons transfer to higher energy level and afterwards they may fall to the ground state. However, during this process, not all the excited electrons return to the ground state because energy of electrons will be undermined by multitude possible interactions with their molecular environment. When fluorophores return to the ground states, photons are emitted from the surface. The fact is that one fluorophore can generate lots of photons is fundamental to the high sensitivity of fluorescence detecting technique.
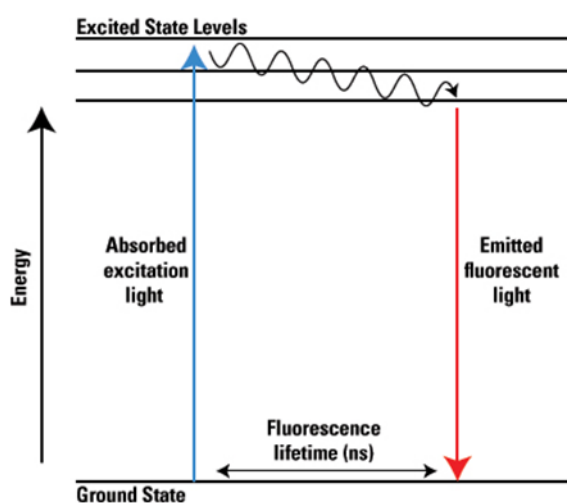
Figure 2-5 Instrumental of the fluorescence detecting technique [112]

In the photocatalytic process, there is charge recombination taking place all through the process. However, it will fundamentally compensate the efficiency of the reaction by reducing the charge density in the materials. The electrons are excited and transfer to reaction interface; they will give off fluorescent light when the recombination happens. In order to measure this phenomenon, the fluorescence spectrometer can be applied to collecting its absorption spectrum and emission spectrum [112].

2.3   DFT Simulations

For the past 30 years, the density functional theory has been the dominant theory in the semiconductor calculation. The reliability of the calculation highly depends on the development of approximation exchange-correlation function theory[113]. Significant progress has been made in the recent years in the local density approximation [114].

The local density approximation is very simple and remarkably reliable for the structure, elastic module, relative phase stability of many materials, but is less accurate for binding energies and details of the energy surface away from equilibrium geometries [115, 116], e.g.: transition states. The GGA family of functional improves binding energies to average errors of 20 kcal/mol and relative errors of 3-7% while meta-GGA and hybrid-exchange functional reduce these errors to 3-5 kcal/mol and 2-3% [117]. This is close to the accuracy required for predictive simulations of thermochemical properties. The GGA, meta-GGA and hybrid functional retain, and somewhat improve, the LDA's excellent description of bonds lengths with typical errors in the region of 1-2 milli-Angstrom [96]. Using these functional elastic moduli is reproduced to within 10% and vibrational frequencies to approximately 40cm^{-1} [118].

2.4   Performance Evaluation

2.4.1   Photo-electrochemistry (PEC) test

In the study of semiconductors, the position and structure of the valence band and conduction band are always of primary importance in the characterization of the prepared materials. Usually, the XPS (X-ray photoelectron spectroscopy), DFT (Density Functional Theory) simulation and electrochemistry test are the techniques applied to identify the band structure of the semiconductors [12]. Among those, Mott-Schottky plot is frequently used to determine the flat band and conduction

band by plotting $1/C^2$ against the applied potential V, where C is the interfacial capacitance. Mott-Schottky and EIS (electrochemical impedance spectroscopy) are of significant importance in describing the very fundamental knowledge of the semiconductor and electrolyte interfacial properties [119].

The energy levels for redox-active species in solution arise by virtue of the donors (Red) and acceptors (Ox) in solution; that is,

$$Ox + e^- \leftrightarrow Red$$
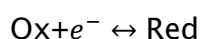
The energy of the solution states depends on whether the state is occupied (Red) or vacant (Ox), owning to the different solvent sheath energy, λ, around Red and Ox species. Since the solvent molecule exchange between the coordination sphere of redox-active species and the bulk electrolyte is a dynamic process which leads to a range of solvent-sheath energies, the density of the redox states can be best described in terms of separate Gaussian distribution [7, 120].

In the interfacial of the semiconductor and electrolyte, the energy level can be illustrated as the picture below. An energy-level diagram of the n-type semiconductor and a redox couple in an electrolyte solution is shown in the Figure 2-6.

For the semiconductor, we have identified the valence band, the conduction band edges (VB and CB respectively), the band gap energy (E_g), and the Fermi level (E_f) which is the energy at which the probability of an electronic state being occupied is 0.5 [4, 121]. These bands are dependent on the semiconductor potential, φ, charging as -eφ, where the e is the charge on the electron [31].
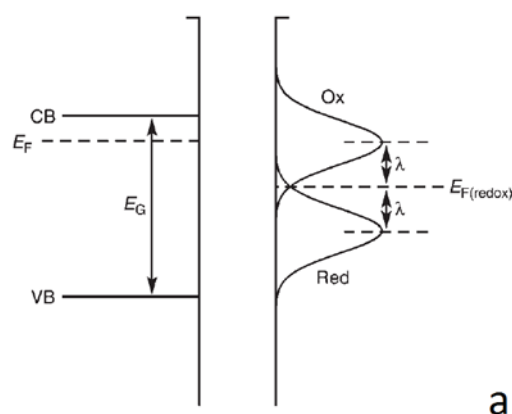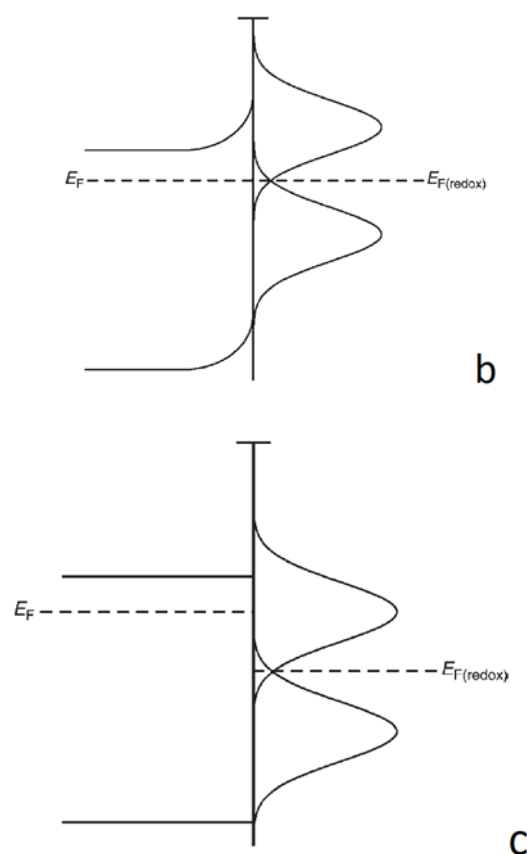
Figure 2-6   Schematic of an n-type semiconductor showing the valence and conduction bands, Femi level, band gap energy, and the redox states in the solution, with their corresponding Femi level and solvent reorganization energy. Also, electronic equilibrium between the n-type semiconductor and redox couple in solution is presented in the gram. Situation when the semiconductor is at its flat-band potential V_{fb} [94].

When an n-type semiconductor and a redox couple come into contact, EF is higher in energy compared to E_f (redox), equilibrium can be derived through the transfer of electrons from the semiconductor to Ox, so that the Fermi levels for both phases are equal [122], as in Figure 2-6. This has the effect of charging the semiconductor positively, and since semiconductor carrier densities are much lower than those in solution, the diffuse charge in the semiconductor (space charge region) is counterbalanced essentially by a sheet of charge in the electrolyte [57]. Changing the voltage of the semiconductor artificially using a potentiostat causes the semiconductor and redox couple Fermi levels to separate, and hence the level of band bending owing to electron depletion in the semiconductor will change depending on the applied voltage [92, 123, 124]. When the voltage is applied so that there is no band bending, or charge depletion (Figure 2-6c), the semiconductor is at its flat-band potential, V_{fb} [125].

The position of the valence band and conduction band comply with the Poisson Boltzman Equation, which describe the electrochemical potential of irons in the diffusion distribution in the three demission which [7, 126],

$$\frac{\partial^2 \phi}{\partial x^2} = -\frac{\rho}{\varepsilon \varepsilon_0} \qquad (21)$$

Where ρ corresponds to the charge density at a position x away from the semiconductor surface, ε is the dielectric constant of the semiconductor, and $\varepsilon 0$ is the permittivity of free space. Using the Boltzmann distribution to describe the distribution of electrons in the space charge region and Gauss' law relating the electric field through the interface to the charge contained within that region [116], Poisson's equation can be solved to give the Mott–Schottky equation:

$$\frac{1}{C^2} = \frac{2}{\varepsilon \varepsilon_0 A^2 e N_D}(V - V_{fb} - \frac{k_B T}{e}) \qquad (22)$$

Here C and A are the interfacial capacitance and area respectively, N_D is the number of donors, V is the applied voltage, kB is Boltzmann's constant, T is the Kelvin temperature, and e is the electronic charge. Therefore, a plot of $1/C^2$ against V should yield a straight line from which V_{fb} can be determined from the intercept on the V axis. The value of ND can also be conveniently found from the slope knowing ε and A [122].

Besides, the charge transfer during the photocatalytic reactions is another aspect which determines the performance of the photocatalysis. In order to have a good understanding of charge transfer process, the Electrochemical Impedance Spectroscopy (EIS) was introduced into my research to investigate the double layers. EIS is a useful tool to characterise the electrochemical reaction, such as photocatalytic reactions [116, 127, 128]. This technique offers means to measure the current response over a range of frequencies, and therefore the impedance of the system is determined. EIS is now widely applied to analysis of energy storage, corrosion and coating properties [11, 129, 130].

The basis of the EIS experiment is to implement a small amplitude sinusoidal AC voltage, V(t), and then measure the amplitude and phase angle of the resulting current, I(t). From this impedance, Z(ω), can be expressed using the Ohm's Law.

$$V(t) = V_0 + V_m \sin(\omega t) \qquad (14)$$

$$I(t) = I_0 + I_m \sin(\omega t + \theta) \qquad (15)$$

$$Z(\omega) = \frac{V_t}{I_t} \qquad (16)$$

Here V_0 and I_0 are the DC bias potential and the steady-state current flowing through the electrode, respectively, when the impedance experiment conducted V_m and I_m are the maximum voltage and current of the supplied sinusoidal signals, respectively, and θ is the phase angle of the resultant current. As an alternative, a more solid explanation describes $Z(\omega)$ in terms of orthogonal axes rather than polar coordinates:

$$Z(\omega) = Z' + jZ'' \tag{17}$$

$$Z' = |Z(\omega)|\cos(\theta) \tag{18}$$

$$Z'' = |Z(\omega)|\sin(\theta) \tag{19}$$

Here j is the imaginary number ($j = \sqrt{-1}$). A range of frequencies, ω, can be examined to generate an impedance spectrum.
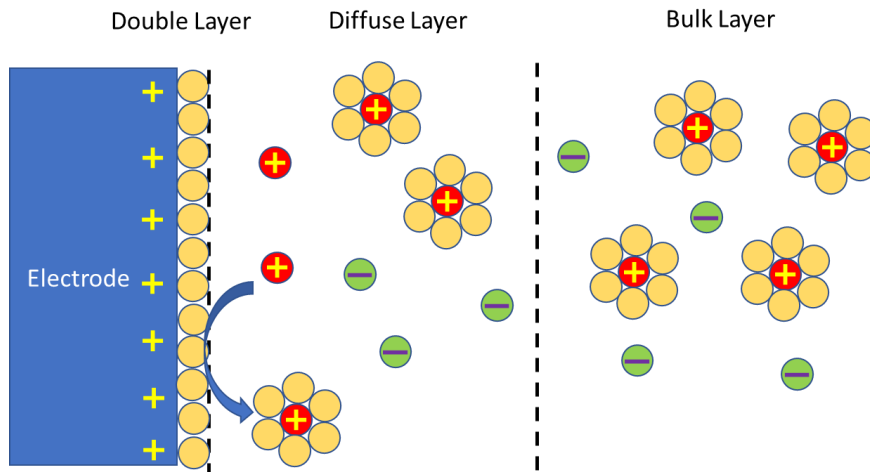
Figure 2-7 Schematic of double layer in a liquid at contact with a positively-charged solid electrode
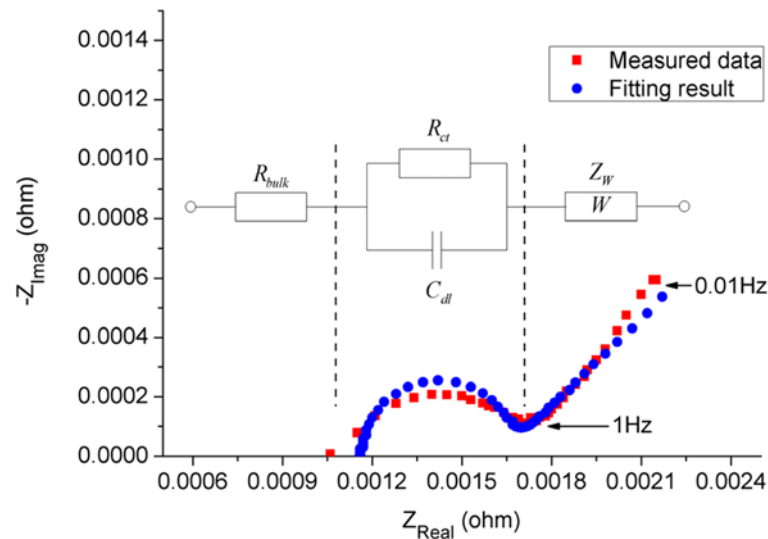
Figure 2-8 Typical EIS response for TiO$_2$ in the electrolyte [131]

Interoperation of this EIS data was carried out by considering the faradic and non-faradic process, which can take place on the interfacial between the TiO$_2$ surface and electrolyte and relate the results back to the Randles circuits as shown in Figure 2-8.

The only faradic process involves the charge transfer in the redox couple. Charge transfer in this redox couple is represented by the resistance of Randle circuit (R$_{CT}$). In the parallel with R$_{CT}$ is the non-faradic electrode capacitance caused by the building up of charge at the TiO$_2$ electrode surface [7, 129, 132]. In the Randle circuits, it is usually presented by the constant-phase element (CPE) to take into account of the non-homogeneity of the electrode surface; for example, surface of roughness. The depressed semi-circuit seen in the Figure 2-8 indicates surface non-homogeneity. The impedance of a CPE in an arc circuit, Z$_{CPE}$, is

$$Z_{CPE} = \sigma \omega^{-m} \left[cos\left(\frac{m\pi}{2}\right) - jsin\left(\frac{m\pi}{2}\right) \right] \qquad (20)$$

Where σ is the CPE prefactor, ω is the angle frequency, m is the CPE exponent. R$_{CT}$ and Z$_{CPE}$ are in parallel with each other because they represent alternate charge paths at the electrode surface. Also included in series with R$_{CT}$ is Warburg impedance, Z$_W$, which account for the diffusion of electroactive species towards the electrode. It is of significant importance at low frequencies. Z$_W$ is essentially the same as Z$_{CPE}$, but with m = 0.5. The final component is another resistance (RS) representing the voltage drop in the electrolyte owing to the passage of current between the surface of the TiO$_2$ electrode and the reference electrode.

Chapter 3 **Zn-doped BiOBr photocatalysts: the effects of Zn-doping on the structure and the visible-light-responsive photocatalytic properties**

3.1 Introduction

Bismuth oxyhalide compounds have found to be potential candidates in the preparation of photocatalytic heterojunction. Among those bismuth oxyhalide, BiOBr is of particular importance because it's visible light response, relatively stable under the light irradiation and superior to the commercialized Degussa P25 (TiO$_2$ aerosol mixture comprising of Rutile and anatase phases) under UV illumination [133, 134]. As shown in the picture below, BiOBr is a type of layer-structured semiconductor that consists of tetragonal [Bi$_2$O$_2$]$^{2+}$ positive slabs, which is intercepted by double slabs of Br$^-$ to form Bi$_2$O$_2$Br$_2$ layers along c axis. The excellent intrinsic crystal structure endows BiOBr with excellent electrical, optical and photocatalytic property [67, 134, 135]. Apart from that, its photocatalytic performance is also correlated with particle size and crystallinity, which is determined by the synthetic routes. The various preparation of the BiOBr in the same time exerts certain influence on the morphology and efficiency of photo-catalysis of the material [136].
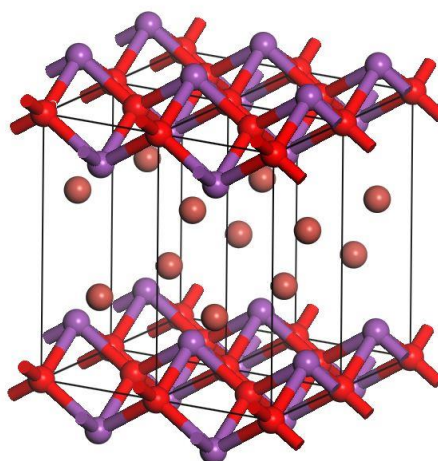
Figure 3-1 2×2×1 supercell of BiOBr

In the view of improving the efficiency of the photo-catalyst, the band structure engineering with dopants can be a reasonable technique, not only because doping can optimize electronic properties of the materials by influencing the band structure of materials but also promote the light harvesting of the materials [32, 137, 138]. Performance of numerous photo-catalysts has been reported to be successfully promoted by modification of the electronic band structures and crystal properties [56, 67, 106, 115, 139-143]. The modification of BiOBr by doping metal ions and coupling with other semiconductors can significantly promoted the processes of photocatalytic reactions. Transition metal elements with multi-valence states and abundant *d* orbital electrons had also proved to be a promising candidate for the band structure engineering [144]. However, the dopants in the materials do not always produce the good result [139]. It depends on electronegativity of the elements and how the dopants integrate in the materials structure [145]. Interstitials or substitution of the atoms in the cell structure will make a different influence on the properties of the materials [146, 147]. Nowadays, there are some papers claiming that the Zn doped BiOBr or ZnO/BiOBr heterojunctions has significantly promote the photocatalytic efficiency of the ZnO or BiOBr [148, 149]. By introducing Zn into the materials, mixed structures of (Zn)BiOBr, ZnO/BiOBr, ZnO(Br) and ZnBr would probably also obtained in the product. And also, the unique structure of BiOBr may be influenced by the Zn doping [115, 150, 151]. As a consequence, it cannot simply attribute the enhanced performance to the Zn dopants. More importantly, in the previous work, the contribution from photoexcited electrons and holes during the photocatalytic reaction of BiOBr is still under debate. Traditional method for investigating the contribution from charge carriers depends heavily on the performance comparing of photodegradation in different dye solution, nevertheless it has limitations in quantification and isolation of the contribution from charge carriers and radicals.

Here, in order to understand the influence of the metal doping in the BiOBr and the experiment was set up to explore the photocatalytic properties and mechanism of Zn-doped BiOBr, the crystal structure, and electronic structure. 1/8 and 1/16 Zn-doped BiOBr was prepared to discuss the metal doping and influence on the energy band and photocatalytic performance. The origin of the visible-light response of the Zn-doped BiOBr was interpreted via valance band XPS and first-principle simulation using CASTEP package. The photo-catalysis performance of the BiOBr and Zn-doped BiOBr was quantitatively measured by photoelectrochemistry test under visible-light to conclude the roles of Zn-doping as well as the contribution of the photoexcited charge carriers.

3.2 Experimental Section

3.2.1 Synthesis of hierarchical structured Zn-doped BiOBr

The different ratios Zn-doped BiOBr was prepared via a simple hydrothermal synthesis. Typically, 1.48g $Bi(NO_3)_3 \cdot 5H_2O$ was dissolved in 3 ml acetic acid (HAc) and diluted with 17 ml deionised water. Then various amount of $Zn(NO)_3 \cdot 6H_2O$ was added into the solution of $Bi(NO_3)_3$. The mole ratio between Zn and Bi were in 0:1, 1:8 and 1:16. 2.035g NaOH and 0.415g KBr were dissolved in 20ml deionised water. Two solutions were mixed together with the pH kept in 12. The resulting solutions were then undergoing rigorous stirring for 6h before an overnight aging. After that the precipitation was washed with deionised water and dried in oven under 60℃.

The photoelectrodes of xZn-BiOBr photocatalysts were fabricated by doctor-blade coating of the photocatalyst pastes onto clean ITO/glass (resistance of 15Ω/sq, 1.5 cm x 1.5 cm slices) which was pre-washed alternatively by DI water and absolute ethanol under ultrasonication (40 kHz, 5 min each). The pastes of photocatalysts were prepared by mixing 0.1 g photocatalysts with 100 µL ethanol/water (3:1) solution. 10 µL of photocatalyst paste was dropped on the dry clean ITO/glass fixed on flat bench using scotch tape to expose 1 x 1.5 cm^2 area, and then slowly rolled a clean glass rod to cast the film. The casted films were then dried at 60 ℃ for 24 h before photoelectrochemistry tests.

3.2.2 Characterizations

All the x-ray diffraction data were collected form the Rigaku Smart Lab using Cu-Kα1 radiation (λ=0.154056 nm) at a scan rate of 0.05˚ $2\theta^{-1}$s and were used to determine the phase of the structures of the samples. The UV-vis diffuse reflectance spectra were obtained on Perkin Elmer Lambda 950 UV/Vis/NIR spectrophotometer equipped with a 150 mm snap-in integrating sphere for capturing diffuse and specular reflectance. $BaSO_4$ was used as a reflectance standard in the UV-visible diffuse reflectance experiment. Scanning electron microscopy (SEM) was performed to investigate the surface morphology using JEOL JSM-6301F Field Emission SEM at an accelerating voltage of 10kV. X-ray photoelectron spectroscopy (XPS) was performed in a Thermo Scientific Escaplab 250 K-alpha photoelectron spectrometer using monochromatic Al-Ka radiation. Survey scans were collected in the range 0–1100 eV (binding energy) at pass energy of 160 eV. Valence band spectra were also recorded. Peak positions were calibrated to carbon and plotted using CasaXPS software.

3.2.3   DFT simulations

The CASTEP code was applied to calculate the band structure of the Zn-BiOBr on the supercomputer. The electronic structure was calculated via HSE06 (Heyd-Scuseria-Ernzerhof) function which is a kind of hybrid approximation of the exchange-correlation functional energy in density functional theory (DFT). The non-conserving pseudopotentials were implemented in the calculation. In my calculation, the spin polarization effect is considered, and the energy cut-off for the plane wave expansion is set to be 750 eV, meanwhile, the calculation precision is set to 2.0×10^{-6} eV/atom. The band structures were calculated along the special lines connecting the following high-symmetry points: Z (0,0,0.5), A (0.5,0.5,0.5), M (0.5,0.5,0), Γ (0,0,0), Z (0,0,0.5), R (0,0.5,0.5), X (0,0.5,0) and Γ (0,0,0) in the k-space. The k-point spacing is 0.125. The module and parameters of the crystal was set up on the Material Studio before submitted to the supercomputer. Here the super cell (2×2×1) was built to simulate the Zn doped BiOBr. One of the Bi atoms in the super cell was replaced by the Zn. After that the cell was optimized and uploaded to the supercomputer to carry out the rest of the simulations.

3.2.4   Photocatalytic tests

The photocatalytic activity of the prepared samples in terms of the photocatalytic decolourization of RhB(Rhodamine B) aqueous solution was performed at ambient temperature under visible-light irradiation using a 500W Xe lamp (15 cm above the dishes) with a 400 nm cut-off filter as a light source. In the photo catalysis experiments, 0.1 g of the prepared photo catalyst powder was dispersed in a 100 mL RhB aqueous solution with a concentration of 10 ppm in a beaker. The mixed solution was remained in dark for an hour to establish an RhB solution adsorption–desorption equilibrium on the photo catalyst before light irradiation. During photocatalysis, the 4mL reaction solution was taken out in every 3 mins irradiation interval and filtered to measure the concentration change of RhB using a UV-visible spectrophotometer. Since the RhB was at rather low concentration in the aqueous solution, its photo degradation followed a pseudo-first-order reaction and its kinetics can be expressed as

$$-\ln\left(\frac{c}{c_0}\right) = kt \qquad\qquad (1)$$

Where k is the apparent rate constant and c0 and c are the initial and reaction concentrations of aqueous RhB solution, respectively. Photoelectrochemical measurements were conducted in three-electrode cell using AUTOLAB PGSTAT 30. The as-prepared films were used working electrode. A platinum wire was used as

counter electrode and calomel electrode was used as reference electrode. All the electrode was placed in electrolyte of 100ml 0.5M Na_2SO_4 (pH 6.5). Potentials were referenced to reversible hydrogen electrode (RHE) using Nernst equation:

$$E_{RHE} = E_{calomel}^0 + E_{calomel} + 0.059pH, \ E_{calomel}^0 = 0.241 \ at \ 20°C \quad (2)$$

The quantitative analysis of M-S data to acquire flat band potential (V_{fb}) is based on the Mott-Schottky law from the plots of C_{sc}^{-2} versus the applied potential bias (V_{app}):

$$\frac{1}{C_{sc}^2} = \frac{2}{A^2 \varepsilon_0 \varepsilon_r e N_d} \left(V_{app} - V_{fb} - \frac{k_B T}{e} \right) \quad (3)$$

where C_{sc}, A, N_d, ε_r and ε_0 are respective to the space capacitance, electrode area (1.0 cm2 in this work), donor density, relative dielectric of semiconductor and vacuum dielectric, while the kB, T and e stand for the Boltzmann constant (1.38x10-23 J/K), system absolute temperature (293 K here) and charge of electron (1.602x10^{-19} C). Extrapolation linear M-S plot to potential bias axis leads to an interception potential (V_{extro}, the corresponding charge energy of E_{extro} =e · V_{extro}), while the slope of the M-S straight plot is proportional inversely to the density of majority carriers (N_d, e- and h+ for n-type and p-type semiconductor, respectively)[122]. The acquired Eextro can be manipulated by the following equations to gain band edges in RHE scale.

$$E_{fb\sim SCE} = E_{extro} - k_B T/e \quad (4)$$

$$E_{fb\sim RHE} = E_{fb\sim SCE} + E_{SCE\sim RHE}^0 + \frac{RT}{nF} pH \quad (5)$$

$$E_{CBM} = E_{fb\sim RHE} - 0.2eV \quad (6)$$

$$E_{VBM} = E_{CBM} + E_g \quad (7)$$

The equations 3~4 were applied to calibrate the potential contributions from temperature T (by $\frac{k_B T}{e}$ in eq. 4) and pH (by $\frac{RT}{nF} pH$ in eq.5), where R, n and F represent the universal gas constant, the number of electrons involved in the electrode reaction and the Faraday constant, respectively. In the equation (6), 0.2 eV was applied because the CBM potential is typical 0.2 V more negative than flat-band for most n-type semiconductors [122, 152]. The E_g, E_{CBM} and E_{VBM} are bandgap, energy positions of CBM and VBM, respectively.

3.3   Results and Discussion

3.3.1   Crystal structure and Morphology

The X-ray diffraction results confirmed the presence of the layered BiOBr in the materials. All the detailed patterns from BiOBr and Zn-doped BiOBr in the Figure 3-2(a) are well matched the pure tetragonal phase BiOBr (JCPDS 73-2061), which indicates the zinc dopant did not significantly change lattice structure of BiOBr. However, a slightly shift of (110) and (102) peaks can be observed in the Figure 3-2(b). Peak (110) is shifted to higher degree in Zn-doped BiOBr, while (102) is shifted to smaller degree. The lattice parameters derived from XRD results and computational simulation are compared and presented in the Table 3-1. In the Table 3-1, the lattice parameters a, b and c derived from XRD are gradually reduced, which are in a good agreement with the results of CASTEP. By introducing Zn into the BiOBr, Bi ions with radius of 1.03Å were partly replaced by smaller Zn ions 0.74Å, which would directly leads to a decrease in the lattice parameters a and b.[153] At the same time, in the c-axis, Van der Walls force between the $[Bi_2O_2]^{2+}$ and Br^- layers were gradually reduced as more Zn^{2+} took the place of Bi^{3+} in crystal structure. In general, the influence of zinc dopant on the lattice parameters can be observed through peaks shifts in the XRD patterns, which implies that inner built electric filed by layered structure could be affected when zinc was introduced into the system. In the BiOBr, it is of importance to retain its layered structure for its photocatalytic properties, because the dipoles induced by the layered structure will contribute to the charge separation in the photocatalytic process.
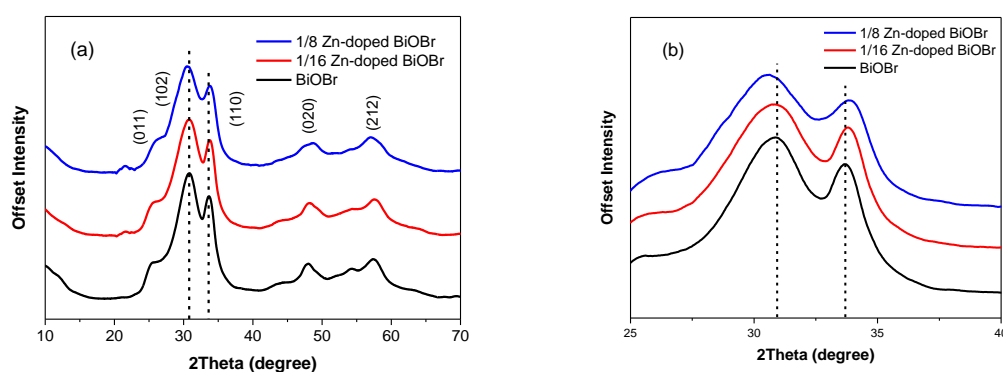
Figure 3-2 XRD patterns of pure BiOBr sample, 16Zn-BiOBr and 1/8Zn-BiOBr

Table 3-1 Lattice parameters and band gap derived from XRD results and CASTEP calculations

	a=b/Å	c/Å	V/Å³	E_g/eV	c/a
BiOBr (CASTEP)	3.7573	9.7672	137.6224	2.42	2.5995
	(3.8377)	(9.4045)	(138.5089)	(2.60)	(2.4506)
1/16 Zn-BiOBr (CASTEP)	3.7421	9.2882	130.0656	2.76	2.4821
	(3.8133)	(9.3998)	(136.6849)	(2.67)	(2.4650)
1/8 Zn-BiOBr (CASTEP)	3.7273	9.3503	129.9015	2.87	2.5086
	(3.7945)	(9.3595)	(134.7602)	(2.88)	(2.4666)

3.3.2   XPS analysis

The BiOBr core level X-ray photoemission spectroscopy (XPS) was conducted on the surface of BiOBr and Zn-doped BiOBr. In Figure 3-3(a), the peaks of 159.4 eV and 164.8 eV are corresponding to Bi $4f_{7/2}$ and Bi $4f_{5/2}$, respectively. The fitted peaks centring at 159.4 eV can be attributed to Bi^{3+} bonded with O. Meanwhile, minor peaks of 160.5 eV and 165.5 eV can be ascribed to the Bi^{5+} in the materials. When Zn amount in the materials increased, a clear red shift of the peaks of the Bi 4f can be observed, in which the BE (Binding Energy) of Bi is reduced as Zn dopant was introduced into the system to replace the position of Bi in the materials. The Figure 3-3(b) presents the O1s XPS of all three samples. The spectroscopy of O1s in pure BiOBr is composed of three peaks centring at: 532.8 eV, 531.1 eV and 530 eV. The peak at 532.8 eV is corresponding to the surface attached oxygen species such as OH groups, which is result of alkane synthesis condition. The peak at 531.1 eV is corresponding to the Bi-O bond in the BiOBr, and the peak at 530 eV is reasonably assigned to the oxygen vacancies. Comparing O1s peaks of different BiOBr samples, all the peaks are shifted to lower energy as In Figure 3-3(c), the peak located at 69.5 eV and 68.5 eV are corresponding to the contribution from Br $3d_{3/2}$ and Br $3d_{5/2}$. Again, all the peaks of Br are shifted to lower binding energy. The red-shifted peaks

Chapter 3

of Br are due to the gradually weakened Van de Walls force between the $[Bi_2O_2]^{2+}$ and Br⁻ labs as Bi^{3+} was replaced by Zn^{2+}. In the spectroscopy of Zn, the intensity peaks of Zn 2p gradually increased with increasing amount of Zn in the materials.

The overall VBM (valence band maximum) of three samples are compared in the Figure 3-3(e). The width of the valence band is broadened when zinc incorporated into the structure. The rising of the VBM in the Zn-doped BiOBr can be ascribed to the influence of Zn dopants in the materials.

50
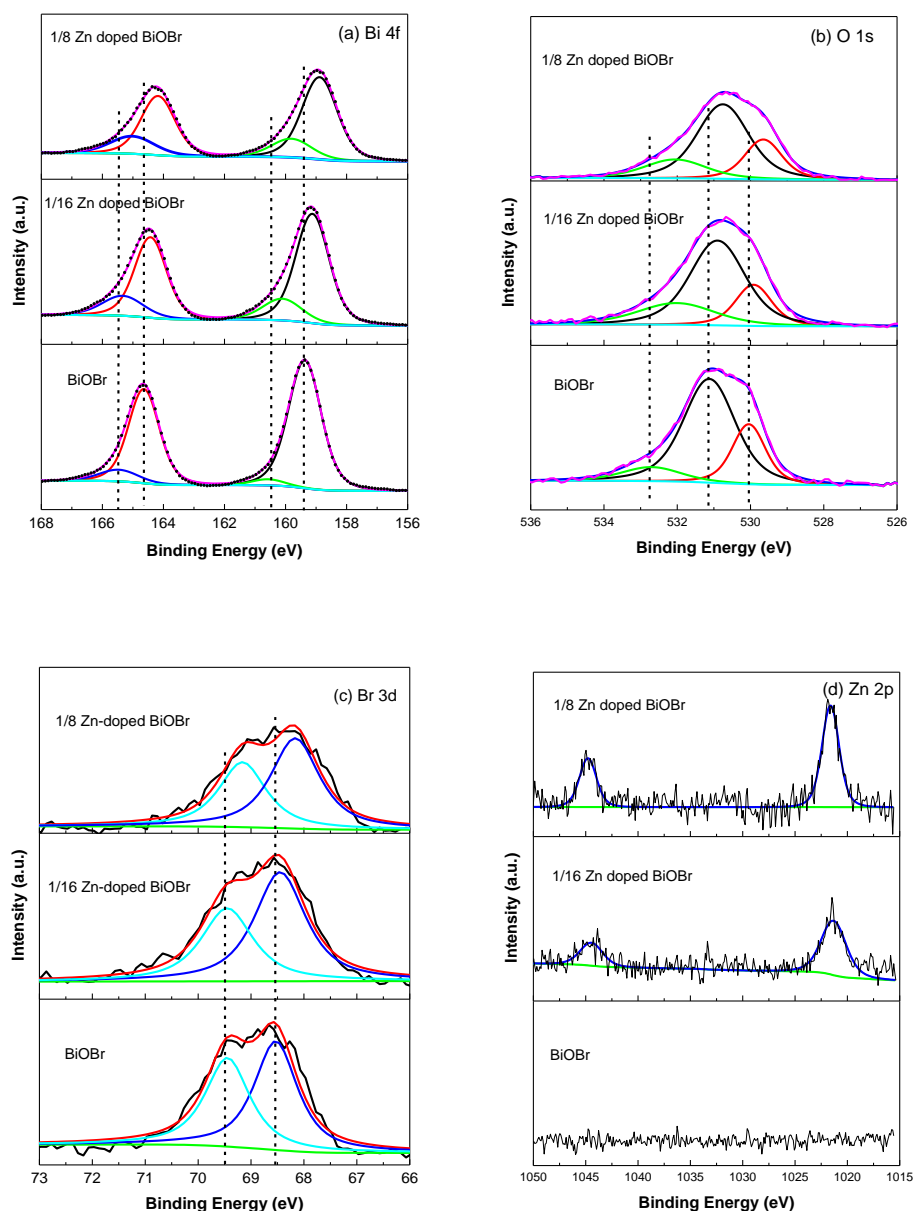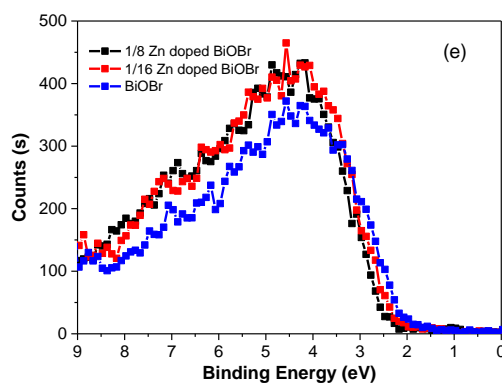
Figure 3-3 Core level XPS of (a) Bi 4f, (b) O1s, (c) Br 3d, (d) Zn 2p and (e) valence band maxium of BiOBr and Zn-doped BiOBr

3.3.3   Computational simulations

The crystal structure of BiOBr belongs to tetragonal matlockite PbFCl-type structure, with symmetry of P4/nmm (space group). This is a layered intergrowth structure that is constructed by the combination of double bromine ions layers and bismuth oxygen layers. A Bi atom is coordinated to with four O atoms; O atom is tetrahedral coordinated to four Bi atoms, and the bromine atom is localized at the vertex of the pyramid that is formed with four Bi atoms in a planer square. Nevertheless, the Bi and Br bonds are very long, so there are no bonds between Bi and Br atoms. Its layered structure is exhibited by an ordered packing of Bi_2O_4 alternating with Br atoms along the c axis direction, through the van der Waals interaction. Using the above-mentioned computational method, the lattice parameters of BiOBr were obtained and listed in table 1: $a=b=3.8377$ Å and $c=9.4045$ Å in BiOBr, $a=b=3.8133$ Å and $c=9.3998$ Å in 1/16 Zn-doped BiOBr; For 1/8 Zn-doped BiOBr, the optimized parameters are $a=b=3.7945$ Å and $c=9.3595$ Å. In the simulation results, the lattice parameters (a, b, c) as well as cell volume (V) are slightly suppressed with increasing the zinc dopant in BiOBr, which reflex similar trend with the XRD result. However, the lattice distortion induced by the Zn doping is not obvious in the simulation. On the contrary, the lattice parameters derived from XRD reveals considerable distortion had taken place in the crystal structure. The distortion and displacement in cells would change the inner built electric field, thereby probably impacting the photocatalytic performance of the materials.

The electronic bandstructures of both BiOBr and Zn-doped BiOBr are calculated and ploted in the Figure 3-4. The energy zero (i.e., the Fermi energy level, E_f) is set at the VBM (valence band maximum). The VBM of pristine BiOBr and Zn-doped BiOBr

are located at the k-point line of Z-R, while the CBMs (valence band maximum) are located at the k-point of Z, which unquestionably indicating Zn-doped BiOBrs are still indirect band gap semiconductor. At the same time, the spin-up sates and the spin-down states are completely coincident. The spin-up and spin-down states are in the same in the cases of pure BiOBr calculation and Zn-doped BiOBr. The calculation shows the band gap of the BiOBr is 2.60 eV which is in a good agreement with the previous report, and the band gap of 1/16 Zn-doped BiOBr and 1/8 Zn-doped BiOBr are 2.68 and 2.88 eV respectively. By Zn doping, the value of E_g is obviously increased, while the type of the band gaps of Zn-doped BiOBr remain indirect. In the Figure 3-4, there is no obvious impurity energy level in the band gap of 1/16 Zn-doped BiOBr and 1/8 Zn-doped BiOBr.

The calculated total and partial density of states of BiOBr and 1/8 Zn-BiOBr are compared in the Figure 3-5. The Bi and Zn mainly contribute to the conduction band, whereas Bi, Br and O contribute to valence band. In the detailed plot of the density of states in the Figure 3-6, the Bi 6p is the major contribution to the conduction band in the BiOBr, while Zn 4s and Bi 6p contributes to the conduction band in 1/8 Zn-doped BiOBr. Compared with Zn, Bi mainly concentrated in the upper part of conduction band, while the Zn contributes to the bottom of conduction band of Zn-doped BiOBr. Comparing the conduction bands of BiOBr and Zn-BiOBr in Figure 3-6, when Zn dopants were introduced into the system, the density of states of the CBM was increased by Zn dopant, yet a clear up-shift of CBM can be observed.

The valence bands, on the other hand, consist of the electrons from Br 4p, O 2p and Bi 6s, among which the electrons from Br 4p hold the majority states of the upper valence band. Meanwhile, it is also noteworthy that the states of Br 4p, O 2p as well as Bi 6s in top of valence band are reduced in terms of density of states as Zn introduced into the system. And overall area of VBM of Zn-doped BiOBr declines compared with pure BiOBr, indicating that number of photoexcited holes will be reduced. However, the width of the valence band of Zn-doped BiOBr is slightly increased, which is also evidenced by the results from valence band XPS in Figure 3-3(e). From the view of kinetics and thermodynamic, the width of the valence band governs the mobility of photoexcited h^+ (holes or positive charges), the widened valence band implies a higher mobility of the holes generated. By Zn doping, the more electrons will be introduced into the CBM and at the same time the positive charged defects will be produced as a result of Bi^{3+} replaced by Zn^{2+} in the BiOBr. When zinc incorporated into the crystal structure of BiOBr, it not only gives a raise to the conduction band edge of BiOBr, but also extends the width of valence band as well as reduces the states of valence band top. Besides that, in order to keep the

charge balance in the materials, extra negatively charged oxygen vacancies and bromide may also have introduced into the materials. As a result, the lattice parameters of the materials will therefore change because size of anions is relatively lager than that of cations.
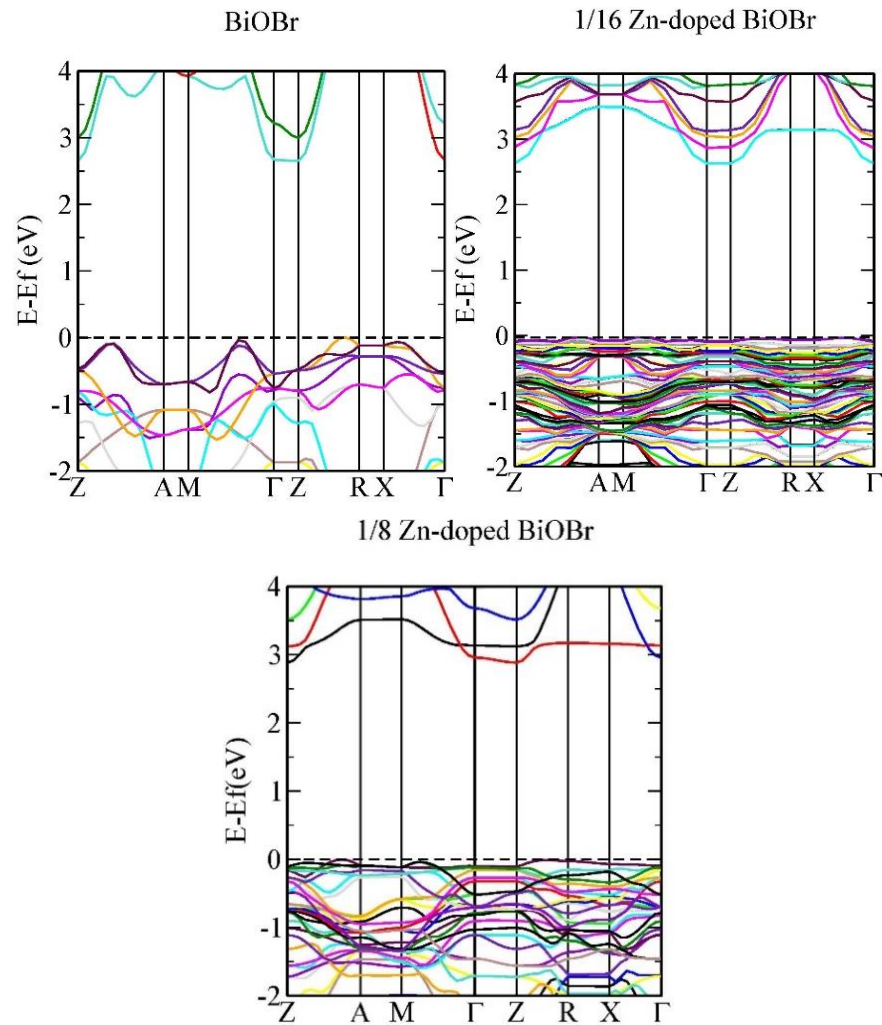
Figure 3-4 Plot of simulation shows the details of the conduction band and valence band of the 1/8 Zn-doped BiOBr, 1/16 Zn-doped BiOBr and BiOBr
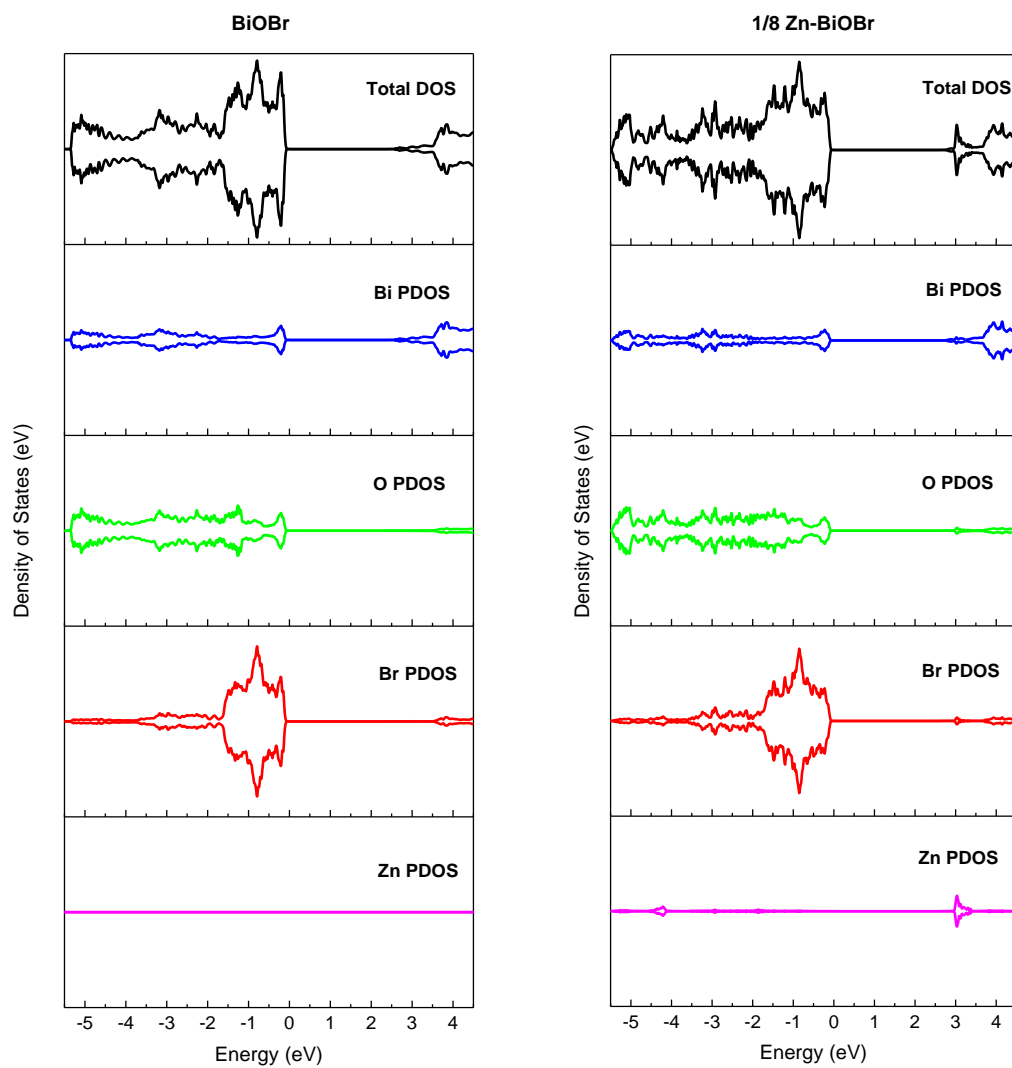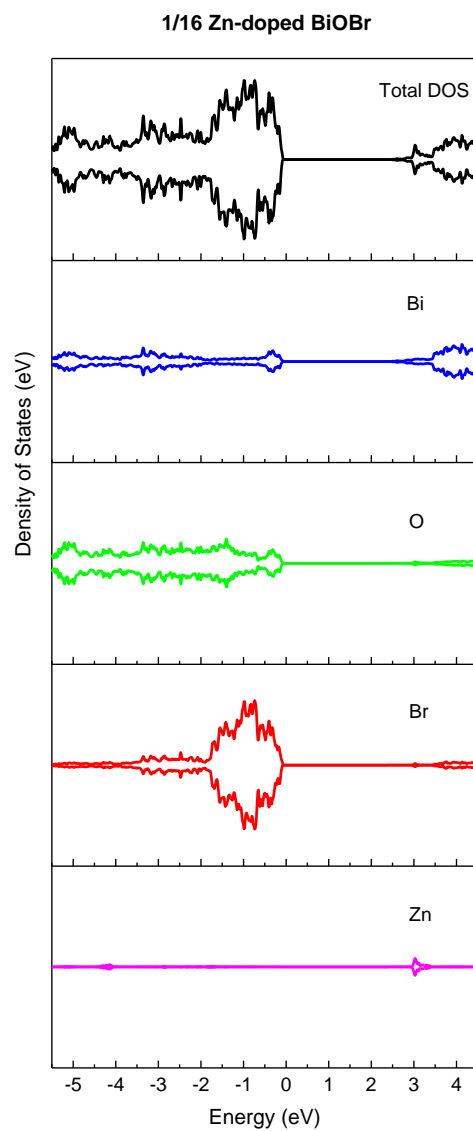
1/16 Zn-doped BiOBr

Figure 3-5 DOS (electronic density of states) of 1/8 Zn-doped BiOBr, 1/16 Zn-doped BiOBr and pure BiOBr
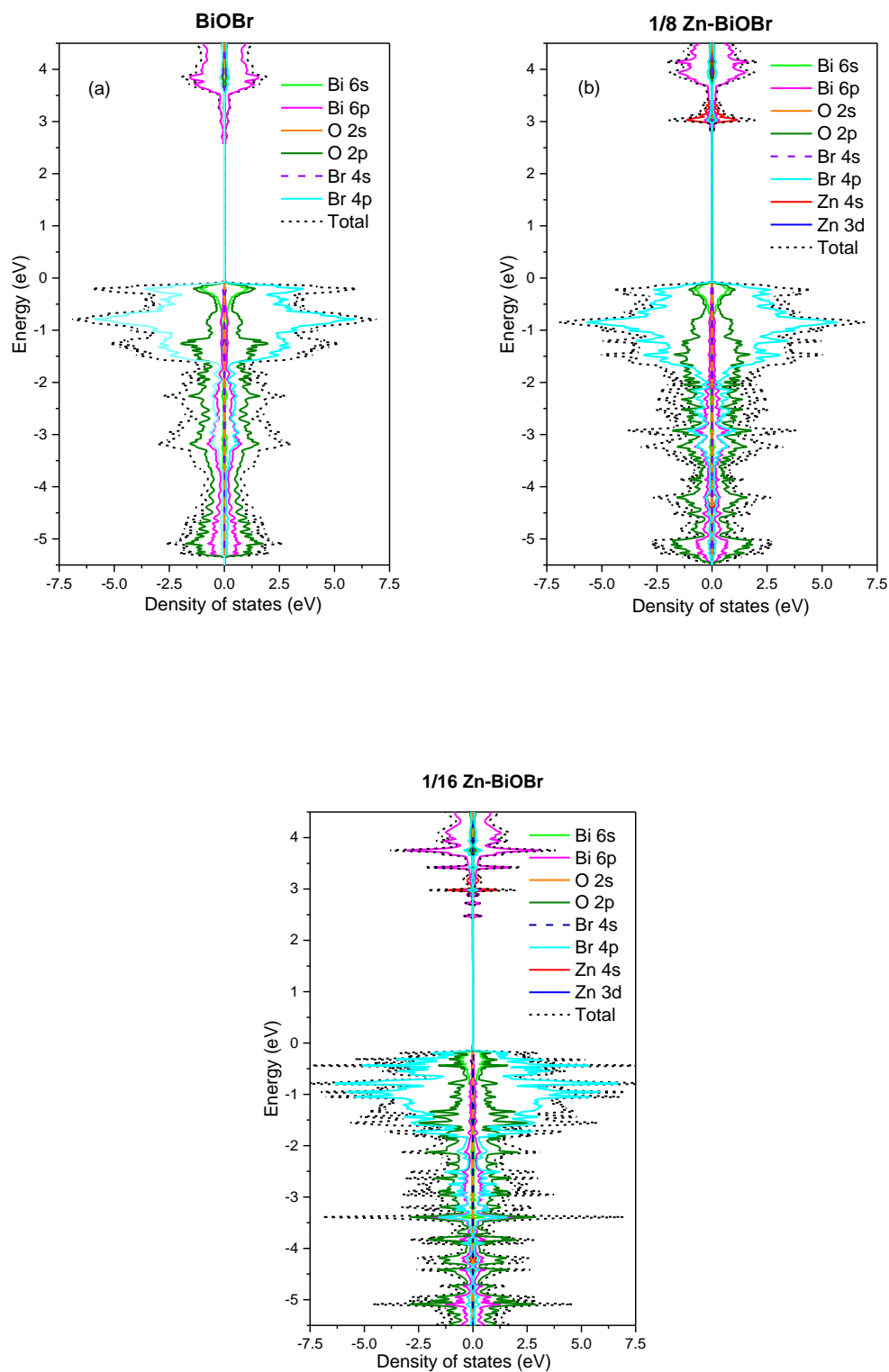
Figure 3-6 PDOS of pure BiOBr, 1/8 Zn-doped BiOBr and 1/16 Zn-doped BiOBr

3.3.4   Optical properties

UV–Vis diffuse absorbance or reflection spectra of a photocatalyst may reflect its ability to harvesting solar radiation and its bandgap energy can be calculated from

the corresponding spectrum. Figure 3-7(a) compares the absorbance of the BiOBr and Zn-doped BiOBr. The absorbance spectrum of pristine BiOBr extends to 600nm, while 1/16 Zn-BiOBr tails at 550nm and 1/8Zn-BiOBr tails at 530nm. BiOBr shows much higher absorption than Zn-doped BiOBr in the range of 400nm-600nm. shows higher absorption than Zn-doped BiOBr from 400nm to 600nm. The 1/8 Zn-doped BiOBr exhibits the lowest absorption compared with BiOBr and 1/16 Zn-doped BiOBr. The data collected from the UV-Vis reflectance was transformed into the Tauc plot in Figure 3-7(b), where the optical band gap of the materials can be obtained. The optical band gap of BiOBr, 1/16 Zn-deoped BiOBr and 1/8 Zn-doped BiOBr are 2.42 eV, 2.74 eV and 2.87 eV respectively. An obvious increase of the gap can be observed. The UV diffusion results identify the computer simulation that the both materials are in a similar band gap. The broaden band gap of the semiconductor can be attributed to the influence of Zn dopant on the energy bands and crystal structure of BiOBr.
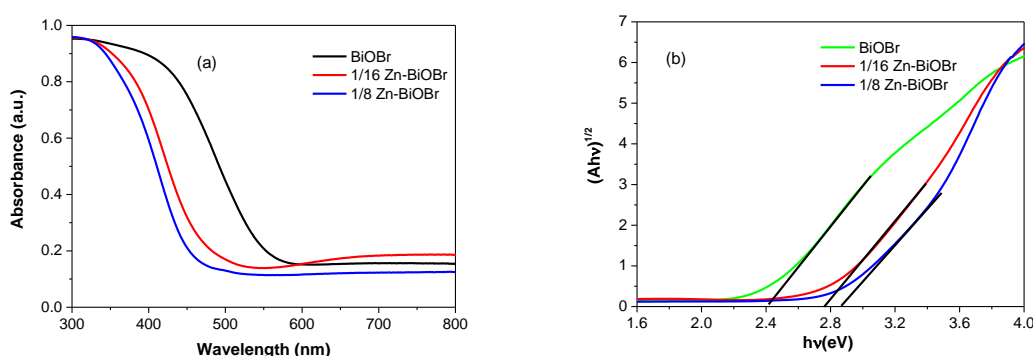
Figure 3-7 UV-Vis absorbance spectra and tauc plot using the data from UV-vis diffuse reflectance spectra of pure BiOBr, 1/16 Zn-BiOBr and 1/8 Zn-BiOBr samples

3.3.5 Photocatalytic activity

During the degradation test, catalyst (0.1g) was added in 20ppm RhB solution with a filter of 400nm cut-off. In the Figure 3-8(c), the photocatalytic performance of BiOBr is superior to the Zn-doped BiOBr in the degradation of RhB. The activity of the photocatalytic degradation decreased with increase of zinc amount in BiOBr. The degradation of RhB on BiOBr and Zn-doped BiOBr follows the pseudo-first-order kinetics model, $ln(C/C_0) = -kt$, where the C and C_0 are the concentration of RhB in the solution during the reaction and the beginning, respectively, and k is the rate constant of the kinetics model. The k of degradation of RhB was calculated from $-ln(C/C_0)/t$ and listed in the Table 3-2. Among three samples, pristine BiOBr shows the highest photocatalytic activity with k=0.1528, which followed by k=0.1357 of

1/16 Zn-BiOBr and k=0.1028 of 1/8 Zn-BiOBr. The difference in photocatalytic reactions activity can be ascribed to the broadened the optical band gap in the Zn doped BiOBr. Reduced the light absorption in the Zn-doped BiOBr suggest less energy can be utilised in the reaction process. Thus, energy dependant photocatalytic reaction was influenced. Furthermore, increase of charge recombination in the materials due to the unbalanced internal electric field by Zn dopants will also have a negative impact on the photocatalytic performance.
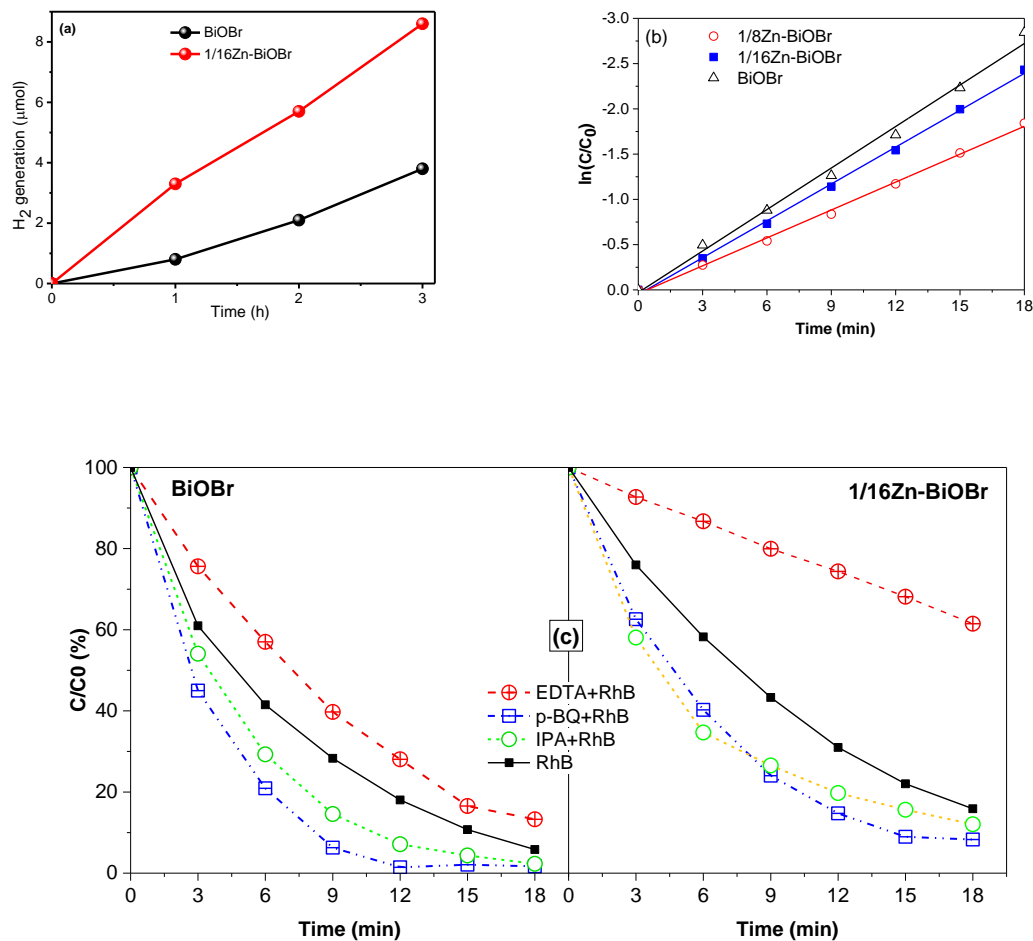
Figure 3-8 Visible-light photocatalytic water splitting (a) and RhB photodegradation on BiOBr and Zn-BiOBr samples: (b) apparent kinetic curves and (c) effects of adding radical scaverngers

Table 3-2 Kinetics constants of photodegradation from BiOBr and Zn-BiOBr

	BiOBr	1/16 Zn-doped BiOBr	1/8 Zn-doped BiOBr
K	0.1528	0.1357	0.1028

3.3.6   Photoelectrochemical performance of ZnBiOBr and BiOBr

In order to understand the influence of transition metal doping on the photocatalytic performance, M-S (Mott-Schottky) plot was recorded in order to discuss the charge density and conduction behaviour in the BiOBr and Zn-doped BiOBr. As shown in Figure 3-9, all the M-S plots display clear n type semiconductor, due to negative slopes in the linear area. The flat band of each sample can be derived by extrapolating the linear area to x-axis, where intercept on x-axis is flat band potential of the materials. In the Figure 3-9, the flat band of BiOBr sample was gradually declined from -0.45V *vs* SCE (calomel electrode) to -0.66V (1/8 Zn doped), while the flat band of pure BiOBr is locate as low as -0.45V. According to the equation:

$$\frac{1}{C^2} = \frac{2}{\varepsilon_0 \varepsilon_r e N_A}\left(V - V_{fb} - \frac{k_B T}{e}\right) \qquad (8)$$

The flat-band values of different samples were determined by the intercepts on the potentials, where the plots were extrapolated to the *x*-axis. The flat-band potentials of BiOBr and Zn-doped BiOBr are listed in the Table 3-3. Taking the typical difference between the CBM and flatband as *ca.*0.3v, the CBM of BiOBr therefore approximately locates at -0.15 V *vs.* RHE. Thus, the VBM (valence band maximum) can be derived by V_{CBM}-E_g, where Eg is band gap from UV-Vis results. The calculated the CBM and VBM are presented in the table 3. Therefore, the band diagram of BiOBr and Zn-doped BiOBr were constructed in the Figure 3-12 with potentials reference of water splitting. The CBM of BiOBr was gradually raised to higher level with increasing amount Zn, which is ascribed to the contribution of Zn dopant in the conduction band. In contrast, the VBM of BiOBr was reduced to lower level with an increase of Zn in the materials, which is in a good agreement with the XPS valence spectrum and can be attributed to the electron localization of Zn in the materials.

Table 3-3 the energy band postion of BiOBr and Zn-BiOBr

Sample	V_{fb}(*vs.* calomel)	CBM (*vs.* RHE)	VBM (*vs.* RHE)	Slope
BiOBr	-0.45V	-0.15V	2.27V	0.9570×10^9
Zn-BiOBr 1/16	-0.56V	-0.26V	2.50V	3.7783×10^9
Zn-BiOBr 1/8	-0.62V	-0.32V	2.55V	3.2109×10^9
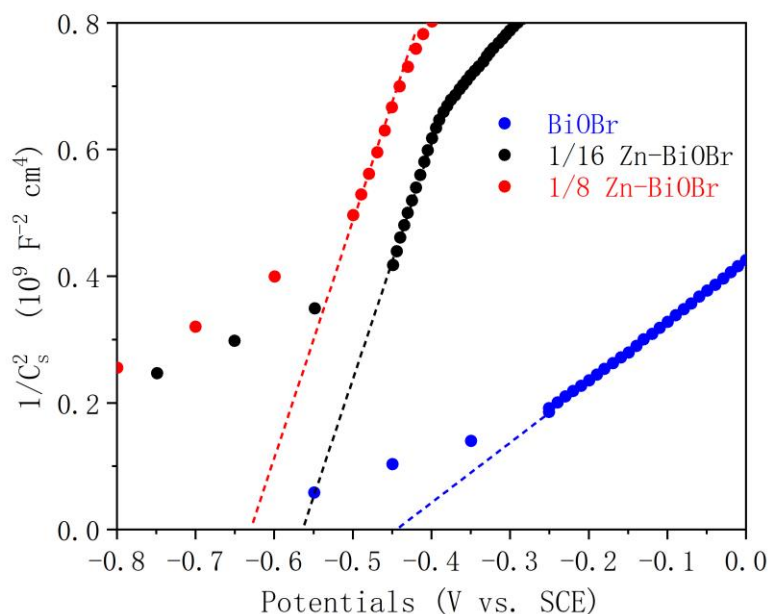
Figure 3-9 Mott-Schottky plots of BiOBr and Zn-doped BiOBr

The photo-current response was measured by the chronoamperometry test under Xe lamp with a filter of 400nm cut-off. In order to have a better understanding of the mechanism of the reaction in the photocatalytic reaction on the surface, dye solution and electron/hole scavengers were also added into the electrolyte. The concentration of EDTA-Na, isopropanol and RhB was kept at 20ppm which is the same concentration of the RhB in the photodegradation test. Comparing with the plots of different samples in Na_2SO_4 shown in Figure 3-10, the pure BiOBr exhibited the highest light response among all three samples, but the light current attenuated as increasing the amount of Zn dopants in the materials. No matter in Na_2SO_4, Na_2SO_4+isopropanol, Na_2SO_4+EDTA-Na or Na_2SO_4+RhB solution, the light current intensity of BiOBr remains highest in all three samples, followed by 1/16 Zn-doped BiOBr and 1/8 Zn-doped BiOBr in terms of peak intensity of current. On the other hand, comparing the light response of a same material in different electrolytes, it is obvious that the peaks of light current intensity are in the order of Na_2SO_4+RhB> Na_2SO_4> Na_2SO_4+EDTA-Na> Na_2SO_4+isopropanol. The materials sensitised by the dye molecules processes the highest activity light response. Furthermore, the individual contribution of electrons, holes and dye molecules can be extracted by calculating the difference between the Na_2SO_4+X and Na_2SO_4. Accordingly, we can propose that it is dye sensitization plays most important role in the degradation of RhB as current response in the dye mixed electrolyte exhibits the highest intensity. In the electrolyte of RhB, the pure BiOBr remains the highest light response, while the light current of Zn doped BiOBr is gradually decreased

with increasing amount of zinc in the materials. It is in a good agreement with the photo-degradation test above. The EDTA-Na and isopropanol here were acted as electrons and holes scavengers respectively during the test, which consumed the electrons or holes during the photocatalytic reactions. Apparently, the huge difference between the current response of materials in the EDTA-Na and isopropanol clarified that the photoexcited electrons other than photoexcited holes contribute most to the photocatalytic process of BiOBr and Zn-doped BiOBr. When comparing the values of the photocurrent in different electrolyte, the sum of the current values in EDTA-Na and isopropanol perfectly match the current values in the Na_2SO_4, which indicates that electrons and holes are the two major parts participating in the photocatalytic reactions.

The comparison of photocurrents arising from solely photogenerated h+ (Figure 3-10, using p-BQ to scavenge e-) and e- (Figure 3-10, using EDTA to scavenge h+) enable us to define their contributions and infer the influences of Zn-dopant on photocatalysis:

1.) The photogenerated e- contributes more than holes on generating photocurrents, which is a typical characteristic of n-type semiconductors (confirmed by Mott-Schottky characterisations, Figure 3-9). Such semiconductor photogenerated e- combined with the e- injected from photoexcited dye predominate their photocatalytic activity;

2.) Relative to BiOBr, the increase of Zn-doping of Zn-BiOBr samples considerably reduce photocurrents of semiconductors and their photogenerated e- and h+, which may be mainly due to attenuated light absorption by Zn-dopants.

3.) The sums of photocurrents arisen from the respective photogenerated e- and h+ on 1/16Zn-BiOBr and 1/8Zn-BiOBr are approximately 20 % and 15% greater (~20%) than that acquired from Na_2SO_4 solution. Such photocurrent difference may be ascribed to the recombination of photogenerated e- and h+ when scavengers are absent. However, the sum of photocurrents induced by e- and h+ for BiOBr photoelectrode are almost identical to its intrinsic photocurrent in Na_2SO_4 electrolyte solution. Apparently, Zn-doping does enhance the recombination of e- and h+ for Zn-BiOBr samples in comparison to BiOBr, though the Zn-dopant induced recombination doesn't contribute significantly to the detrimental photocatalytic activity, at least, much weaker than the dye-sensitisation effects.
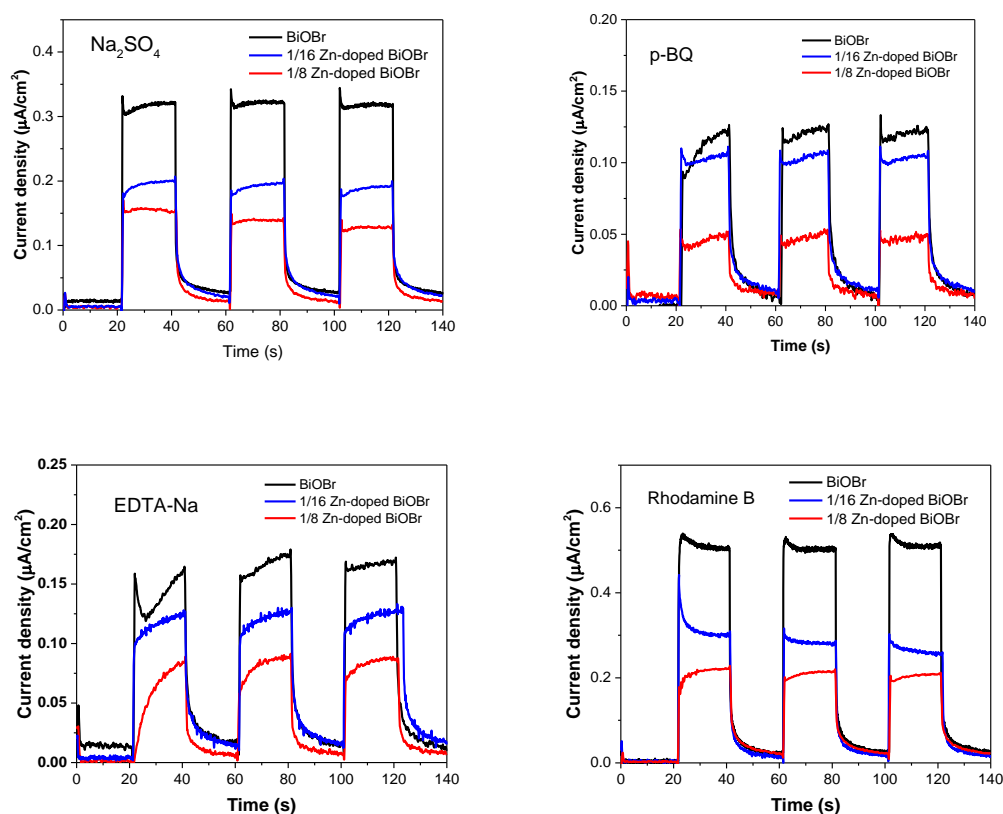
Figure 3-10 Chronoamperometry test of BiOBr, 1/16 Zn doped BiOBr and 1/8 Zn doped BiOBr in Na$_2$SO$_4$, Na$_2$SO$_4$+Isopropanol, Na$_2$SO$_4$+EDTA-Na and Na$_2$SO$_4$+RhB
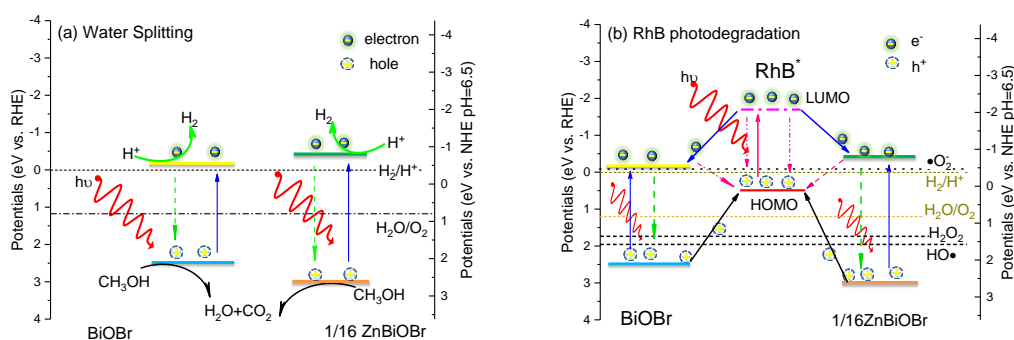
Figure 3-11 Schematic mechanisms of photocatalytic water splitting (a) and RhB degradation (b)

Table 3-4 Steady state photocurrents on the pristine and Zn-doped BiOBr
photoelectrodes

Photocatalysts	Photocurrent density ($\mu A/cm^2$) in the electrolyte solutions [a]			
	Na_2SO_4	Na_2SO_4 + RhB[b]	Na_2SO_4 + EDTA[c]	Na_2SO_4 + p-BQ[d]
BiOBr	0.32	0.51 (+59.4%)	0.17 (~53.1%)	0.15 (~46.9%)
1/16Zn-BiOBr	0.19	0.30 (+57.9%)	0.13 (~68.4%)	0.10 (~52.6%)
1/8Zn-BiOBr	0.13	0.21 (+61.5%)	0.09 (~69.2%)	0.06 (~46.2%)

The photocatalytic degradation of BiOBr was heavily influenced by the participation of the dye molecules. Obviously, the dye molecules RhB was sensitized by adsorbed dye molecules could more effectively inject their photoexcited electrons into the CB of the semiconductor, which then react with surface-adsorbed molecular oxygen to generate active species for pollutant degradation. The ejected electron reacts with adsorbed oxidants (usually O_2) to produce active oxygen radicals (e.g., $O_2^{\cdot-}$, $^{\cdot}OOH$, $^{\cdot}OH$), which subsequently degrade or mineralize the dyes. In the photocatalytic reactions without dye molecules, the photoexcited electrons contribute most to the photocatalytic reactions compared with holes in the electrolyte. On the other hand, the defects in the structure account for the low efficiency of the Zn-doped BiOBr. In order to compromise the positive charge introduced by the Zn, a number of negative ions, such as Br^- and oxygen vacancies, were incorporated into the lattice. These large diameter negative ions inevitably changed the regular layered slabs of the BiOBr. Therefore, the original featured internal layered static electric field between the $[Bi_2O_2]^{2+}$ slabs and double $[Br]^-$ slabs will be heavily weakened by introducing extra negative ions in the structures. More importantly, in the BiOBr photocatalytic degradation test, the internal layered electric field could be advantageous because it is believed to induce efficient separation of the photo-generated electron-hole pairs. As a result of the change in energy band and internal structure, the performance of Zn-doped BiOBr in the photocatalytic activities shows inferior to the pure BiOBr.

The band structures of the BiOBr and Zn-doped BiOBr are ploted out according to data from the XPS and Mott-Schottky plot with the reference of water splitting potentials in the diagrams as well. All the CBM is more negative than H_2 evolution potentials, which shows promising potential for the water splitting. However, with the increase amount of zinc dopant in the materials, the CBM is upshifted and the VBM become lower. The overall band gap of BiOBr is gradually widened with the

increase of zinc content in the materials, which lead to an inevitably decrease of the photo-degradation performance and photoelectrochemical response. The decrease of the photocatalytic light response and degradation performance in Zn-doped BiOBr is mainly assigned to weakened light absorption and fewer valence electrons brought by zinc dopant in BiOBr, which is evidenced by the result in the DFT calculation and XPS spectroscopy of overall valence band.
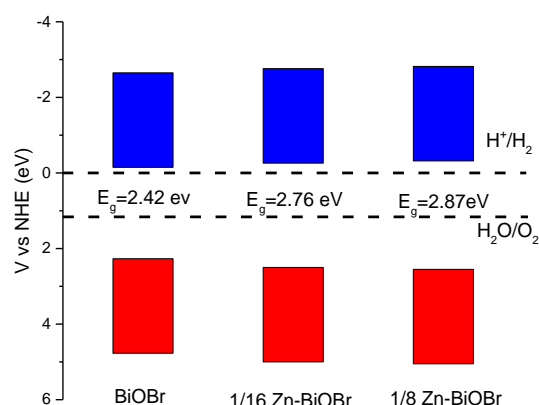
Figure 3-12 Band positions of the BiOBr compared to the potentials of water splitting at pH 0

3.4   Conclusion

Detrimental visible-light photocatalytic activity is observed on the Zn-doped BiOBr samples relative to the pristine BiOBr which were synthesised via a simple alkaline co-precipitation method. The nature of Zn-doping effects on the RhB photodegradation is convincingly clarified from energy perspectives with respect to band structure and photoactive particles (e$^-$ and h$^+$), through a comprehensive spectral, DFT and photoelectrochemical investigation on the crystal structure, optoelectronic properties and photoelectrochemical performance of pristine and Zn-doped BiOBr.

The experimental and DFT characterisations of pure and Zn-doped BiOBr reveal that Zn-doping shrinks the lattice of BiOBr but expands the bandgap due to more negative CBM and more positive VBM, which is different from the doping effects of other metals with open d or f electronic shells. The CBM of BiOBr is predominated Bi 6p state, the CBMs of Zn-BiOBr is found much denser and mainly composing of Zn 4s electron state with a little contribution from Bi 6p state via hybridisation. Very similar to BiOBr, the VBM of Zn-BiOBr comprises Br 3d, O 2p and Bi 6s states but has reduced density. Zn-dopant also expands CB and VB band widths. Although

the band structures of Zn-doped BiOBr samples are changed significantly relative to BiOBr, their bandgap transitions remain indirect. The closed Zn 3d10 electrons are found locating in deeper band far from VBM. The donation of core electrons from Zn to other component atoms has been identified.

The increase of Zn-doping reduces the activity of visible-light-responsive photodegration of RhB. The detrimental photocatalytic activities on Zn-doped BiOBr samples are clearly attributed to the weaker light absorption due to broadened bandgap, reduced dye-sensitisation effects and the ineffectiveness of photogenerated electrons and holes, whereas the Zn-dopant caused recombination of photogenerated e^--h^+ plays marginal roles. The research provides a convincingly quantitative methodology to investigate photocatalysts from optoelectronic energy perspectives, in particular defining the roles of light adsorption, dye sensitisation and photogenerated active particles (e^- and h^+).

Chapter 4   Develop Hierarchically Zn-doped BiOBr Architectures for Enhanced Photoelectrocatalytical Energy Recovery

4.1   Introduction

The previous chapter has clearly proven that the Zn-doped BiOBr with suitable doping level may enhance the water splitting performance because the Zn-dopant promoted conduction band minimum (CBM) position and thus increases the driving force of hydrogen evolution. However, the Zn-doping also broadens the bandgap of BiOBr that decrease the absorption within the sunlight spectrum. Moreover, the Zn-doped BiOBr materials possess low surface areas, which is not satisfactory with the photocatalysis or photoelectrocatalysis because high-performed photocatalysts require large surface areas.

Hierarchical architectures of pristine and doped BiOBr photocatalysts have been reported usually exhibiting enhanced photocatalysis performance in environment remediation, for example photocatalytic degradation of organics or NOx. It has been widely accepted that hierarchical architectures of photocatalysts can not only enhance the absorption of incident light due to attenuated light scattering but also can provide larger surface areas because of the spatial assemblage of constituent nano-blocks. Since photocatalytic reaction is a surface reaction, the large surface area will not only provide more active site for the reactions, but also improve charge transfer in the materials.

Numerous attempts had been made to develop hierarchically assembled pristine and modified BiOBr photocatalysts. However, most of the reported methodologies are either using expensive organic solvent or surfactants which increase the cost of synthesis and bring about environment concerns. Moreover, the conventional synthesis routes also exert different effects on its particle size and morphology, which remarkably influence on their photocatalytic activity [154, 155].

Therefore, it is a necessity to discover a cheaper and environment friendly synthesis method. For example, the micro-emulsion synthesis has been employed to prepare nano-sized BiOBr, nevertheless, the preparation process is costly and time-consuming [156]. The widely applied solvothermal synthesis can easily create the hierarchically assembled architectures of BiOBr nanoflasks, while it requires of

large amount of organic solvent, normally ethylene glycol [157]. In contrast, hydrothermal synthesis is a versatile, low-cost method, which has been used to prepare bismuth oxyhalide in alkaline atmosphere with the assistance of surfactants, such as environment concerned CTAB [158].

This chapter reports a facile hydrothermal method for preparation of hierarchical micro-flowers of Zn-doped BiOBr photocatalysts, which not only preserve the intrinsic photocatalytic properties of Zn-BiOBr but also enhanced the surface areas as compared to randomly aligned Zn-BiOBr photocatalysts. The assembly of the construction nano-blocks may be adjusted by a cheap and environment-degradable surfactant, PEG. Such novel structured Zn-BiOBr photocatalyst are applied in photocatalysis and photoelectricocatalytic energy recovery from wastewater.

4.2   Experimental details

4.2.1   Materials Synthesis

The different ratios Zn-doped BiOBr was prepared via a simple hydrothermal synthesis. Typically, 1.48g $Bi(NO_3)_3 \cdot 5H_2O$ was dissolved in 3 ml acetic acid (HAc) and diluted with 17 ml deionised water. Then various amount of $Zn(NO_3)_2 \cdot 6H_2O$ was added into the solution of $Bi(NO_3)_3$, with the elaborated mole ratios between Zn and Bi were in 0:1, 1:8 and 1:16. The co-precipiting agent is a mixed solution containing 2.035g NaOH and 0.415g KBr in 20ml deionised water with pH of 9.5. The above solutions are mixed together under rigorous stirring for 6h, then transferred to 100ml Teflon-lined stainless autoclave, followed by hydrothermal treatment at 120℃ for 6 hours. After cooling to room temperature naturally, the precipitates are washed with ethanol and deionised water prior to drying in an oven under 60 ℃ overnight to obtain the desired photocatalysts.

4.2.2   Materials Characterisation

All the X-ray diffraction data were collected from the Rigaku SmartLab X-ray diffractometer, using Cu-Kα1 radiation (λ=0.154056 nm) and a scan rate of 0.05° 2θ/s, to determine the crystal phases of the samples. The UV-vis diffuse reflectance spectra were obtained on Perkin Elmer Lambda 950 UV/Vis/NIR spectrophotometer equipped with a 150 mm snap-in integrating sphere for capturing diffuse and specular reflectance, where $BaSO_4$ was used as standard reflectance.

X-ray photoelectron spectroscopy (XPS) was performed on a Thermo Scientific Escaplab 250 K-alpha photoelectron spectrometer using monochromatic Al-Kα radiation. Survey and Valence band spectra were collected in the range 0–1100 eV (binding energy) at pass energy of 160 eV. Peak positions were calibrated to carbon and fitted using CasaXPS software. The morphologies of the samples were measured on JSM59 SEM manufactured by JEOL on which Energy Dispersive X-Ray (EDX) analyser was installed to analyse the composition of specimens in question.

4.2.3 Photocatalytic degradation of RhB and water splitting

The photodegradation of Rhodamine B (RhB) on the as-prepared samples was performed at ambient temperature under visible-light irradiation. A 300 W Xe lamp equipped with a 400 nm cut-off filter to remove UV light was used as light source, irradiating atop with light intensity of 30mW/cm^2 and 15 cm distance away from the beaker containing photocatalyst and RhB aqueous solution. In a typical photocatalysis experiment, 0.1 g of the photocatalyst powder was dispersed into 100 mL 20 ppm RhB aqueous solution. Before light irradiation, the mixed system was remained in dark for one hour to establish RhB adsorption-desorption equilibrium on catalyst surface. The initial concentration (C_0) was defined as the concentration of RhB upon adsorption-desorption equilibrium rather than the original concentration of RhB solution because the photocatalysis occurs on catalyst surface. In order to determine the temporal RhB concentration (C_t) at certain photo-reaction time (t) during photocatalysis, 4 mL liquid suspension was taken out every 3 mins and centrifuged under 6000 rmp to obtain supernatant solution for sampling by a UV-visible spectrophotometer (PerkinElmer Lampda 750s). Since photodegradation of dilute RhB in the aqueous solution is a pseudo-first-order reaction, the apparent kinetic coefficient (k) can be calculated form using the equation below:

$$-\ln\left(\frac{C_t}{C_0}\right) = kt \tag{1}$$

Radical scavenging experiments were conducted to identify the rate-limiting reactive species. Because ethylenediaminetetraacetic acid (EDTA), isopropanol (IPA) and p-benzoquinone (p-BQ) are effective scavengers with respective to h$^+$ at VBM, hydroxyl radical ($\cdot$OH) and superoxygen radical due to e$^-$ at CBM, they were mixed into RhB solution respectively to acquire corresponding photodegradation activities for comparing and assessing the contributions of photogenerated e$^-$ [159] and h$^+$ [160] at band edges into photodegradation.

The experiments of photocatalytic hydrogen from water splitting were carried out in the similar procedure presented in the previous report [161]. Briefly, 100 mg of as-prepared photocatalysts was taken into a homemade reactor containing 80 mL deionized water and 20 mL methanol, to which $H_2PtCl_6 \cdot 6H_2O$ (0.5 wt% to photocatalysts) was added as a co-catalyst. Before photocatalytic testing, the reactor and the entire gas circulating system were de-aerated using a vacuum pump for 30 min. All photocatalytic H_2 generation tests were under continuous illumination using an Autolight CEL-HXF300 xenon lamp (300 W, 100 mW/cm^2) equipped with optical cut-off filters to realize visible light irradiation. The photocatalytic H_2 production was determined using Agilent gas chromatography (GC, 7900) at the sampling interval of 60 mins per test.

4.2.4   Electrochemical measurements

Photoelectrochemistry measurements of the as-prepared BiOBr and Zn-doped BiOBr photoelectrodes were carried out at room temperature in a standard three-electrode cell using the AUTOLAB PGSTAT 302N equipped with FRA spectroscopy. The as-prepared film electrodes, a platinum disk and a saturated calomel electrode (SCE) were used as working electrodes, counter electrode and reference electrode, respectively. The electrolyte supporting solution was 100 mL 0.5 M Na_2SO_4 solution with constant pH of 6.5. The Mott-Schottky (M-S) data were acquired at the optimised frequency of 3000 Hz in dark, with 10 mV/s scan rate and 10 mV AC amplitude. The acquired potentials were transformed to reversible hydrogen electrode scale (RHE) to pH of 0.

The retrieved data of BiOBr and the Zn-doped BiOBr were listed in **Error! Reference s ource not found.**. The chronoamperometry tests (I-t plots) were recorded at light on-off cycle operation (on-off time interval of 20 s) at open circuit potentials (VOC). The photocurrents acquired from Na_2SO_4 electrolyte solution containing RhB were applied to assess the dye-sensitisation effects.

4.3   Results and discussion

4.3.1   Materials structures and morphologies

4.3.1.1   XRD
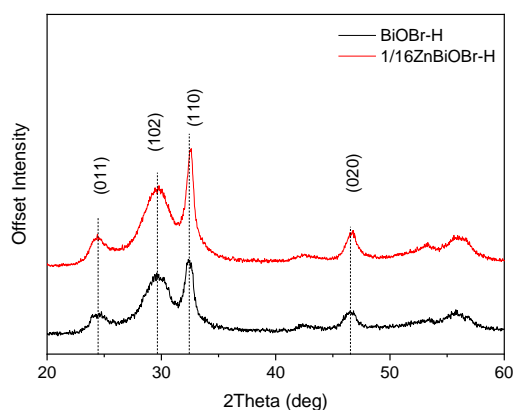
Figure 4-1 XRD pattern of hierarchical BiOBr and Zn-doped BiOBr samples

The XRD patterns shown in the Figure 4-1 are in good match with BiOBr diffraction pattern (JCPDS 73-2061). The indexed peaks exhibited clear tetragonal BiOBr phase with no impurity peaks was identified. However, the shift of the characteristic Bragg diffraction peaks can be ascribed to the incorporation of Zn dopants in the materials. The lattice parameters of the pristine BiOBr and Zn-doped BiOBr were calculated and listed in the Table 4-1. The decrease of lattice parameters of Zn-doped samples relative to the pristine BiOBr can be associated to the substitution of larger Bi^{3+} (radius of 1.03 Å) by Zn^{2+} with smaller radius (0.74 Å).

Table 4-1 Lattice parameters and band gap of BiOBr and Zn-doped BiOBr

	a=b/Å	c/Å	c/a	V/Å^3	E_g/eV
BiOBr-H	3.7621	9.7692	2.5967	138.2673	2.68
BiOBr	(3.7573)	(9.7672)	(2.4506)	(137.6224)	(2.79)
1/16 Zn-BiOBr-H	3.7475	9.5621	2.5516	134.2878	2.80
1/16 Zn-BiOBr	(3.7421)	(9.2882)	(2.4650)	(130.0656)	(2.92)

4.3.1.2   SEM & EDS

The SEM images of the pure BiOBr and Zn-doped BiOBr synthesised through the PEG-assisted hydrothermal method show they both possessed self-aggregated hierarchical structures. It can be clearly observed in Figure 4-2 (a) that the pure BiOBr-H consists of many microspheres with an inhomogeneous size ranging from 3 μm to 10 μm, whereas the size of 1/16ZnBiOBr-H samples shown in Figure 4-2 (c) are more uniform, with the diameters ranging from 3 μm to 5 μm. The detailed morphology unveiled in the Figure 4-2 (b) and (d) suggest that the 1/16ZnBiOBr-H architectures possessed regular microsphere structure, in contrast to the pristine BiOBr-H are randomly assembled randomly platelets of BiOBr. The results suggest Zn-dopant can not only rectified the lattice parameters of the BiOBr crystals, but also influence their self-assembling process.

Moreover, the composition mappings were depicted by EDS characterisation presented in Figure 4-3. According to the mappings, the Zn-dopants are uniformly distributed across the microspheric structures of the photocatalysts. The Zn/Bi molar ratio is roughly 1:15, indicating that Zn ions has been successfully incorporated into the structure of BiOBr, otherwise the Zn would be localised in some parts of the materials [162].
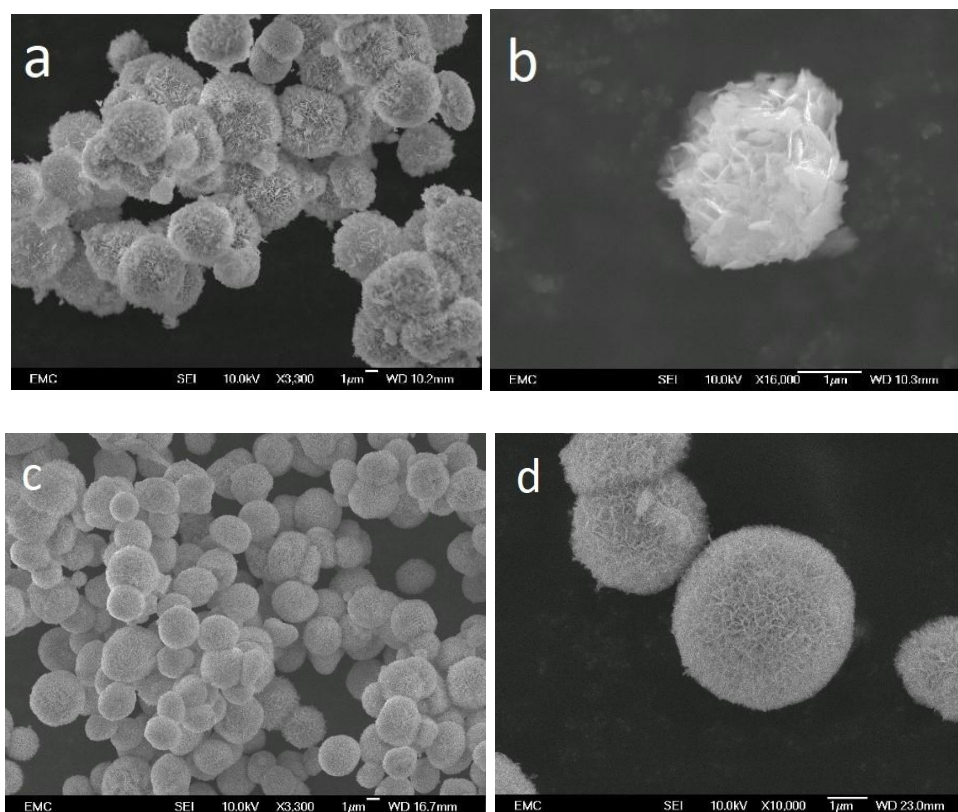
Figure 4-2 SEM images of pure BiOBr-H (a), (b) and 1/16ZnBiOBr-H (c), (d)

Pure BiOBr-H
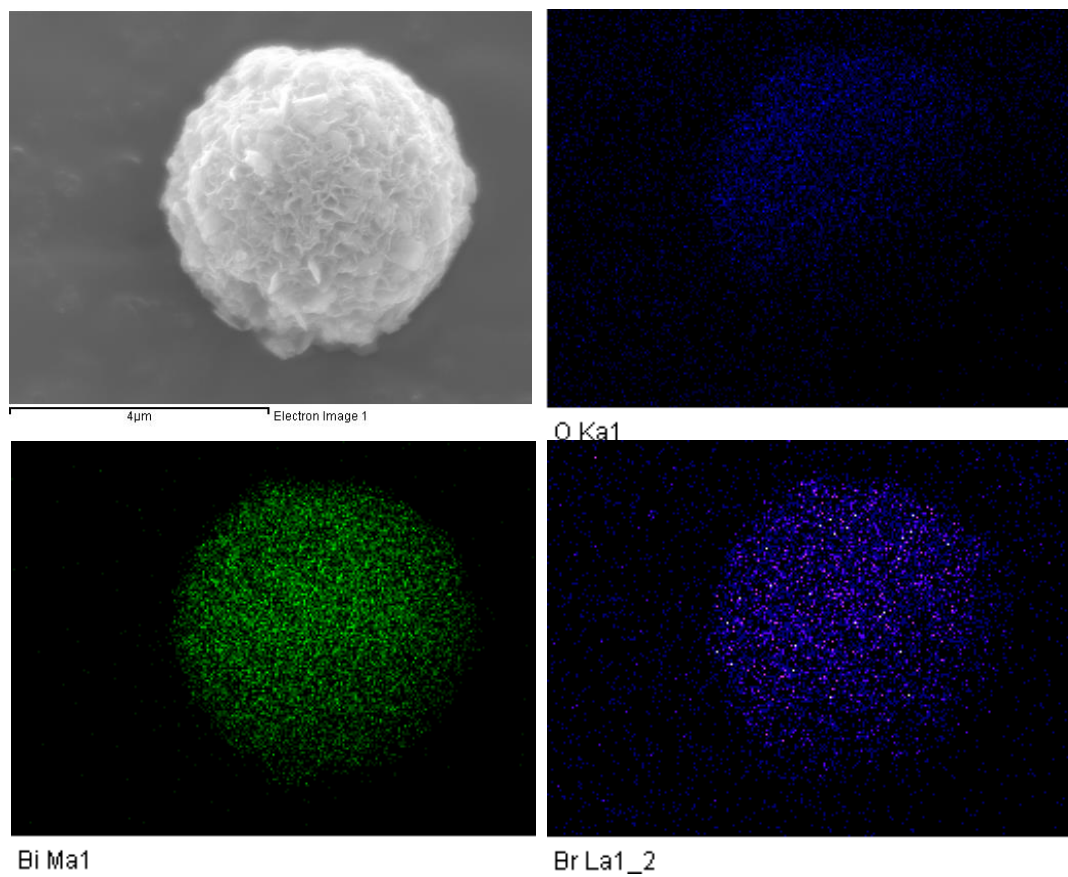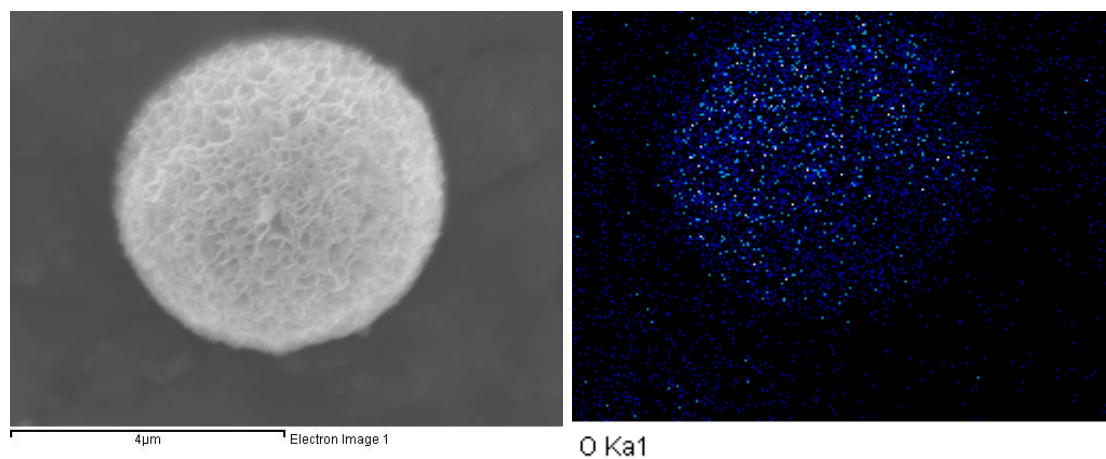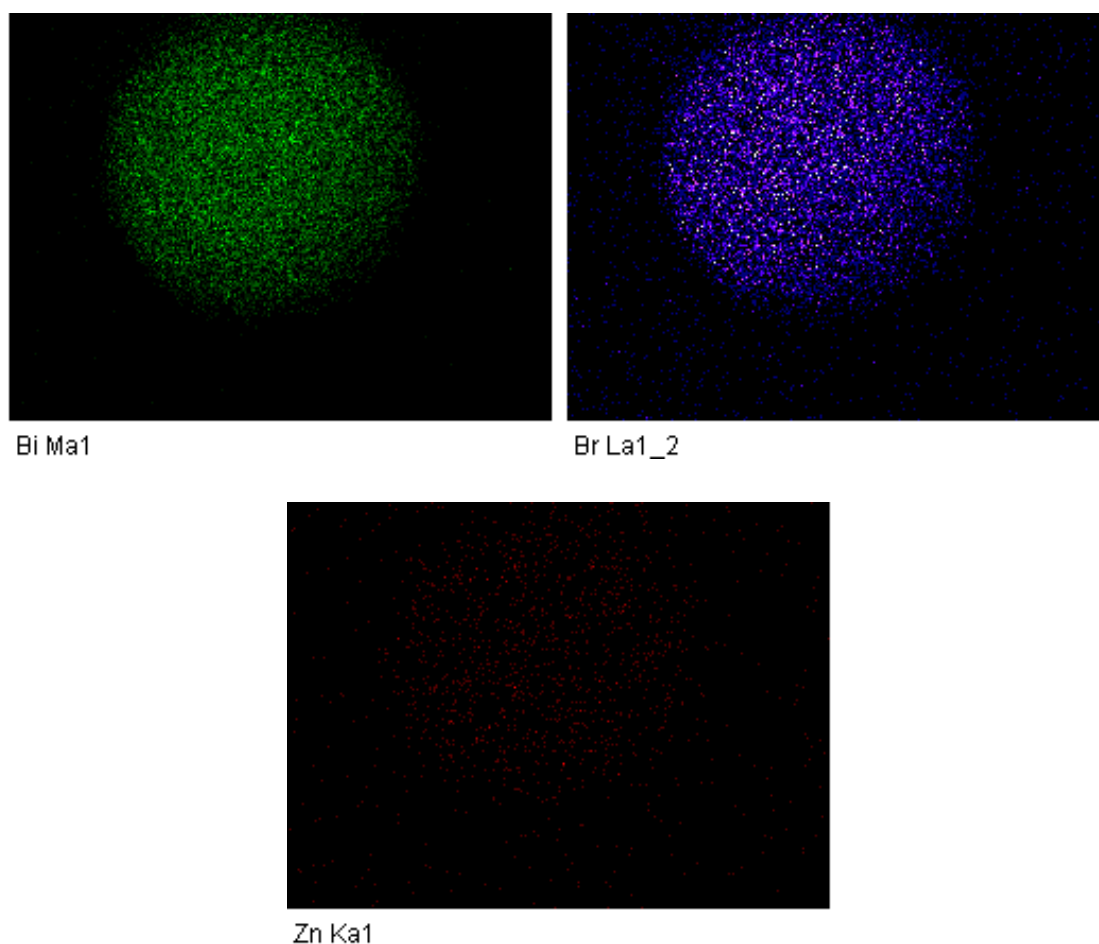
1/16 ZnBiOBr-H

Figure 4-3 EDS mapping of pure BiOBr-H and 1/16 ZnBiOBr-H

4.3.2   Optical properties

The optical absorption of BiOBr and Zn-doped BiOBr were investigated by the UV-Vis spectrometer. The absorbance of BiOBr samples transformed from diffuse reflectance spectra (DRS) was presented in Figure 4-4 in comparison with 1/16 ZnBiOBr. Although the hierarchical Zn-doped BiOBr-H still exhibited inferior light absorption to that of BiOBr, though their absorbance edges, terminated respectively at 500nm and 550nm, are more red-shifted compared with those of the irregular counterparts. The improved light absorption of hydrothermal prepared BiOBr-H and Zn-BiOBr-H can be ascribed to the hierarchical structured morphologies, because more internal-reflection among the constituent nano-flakes, in other word enhanced light trapping within the structure.
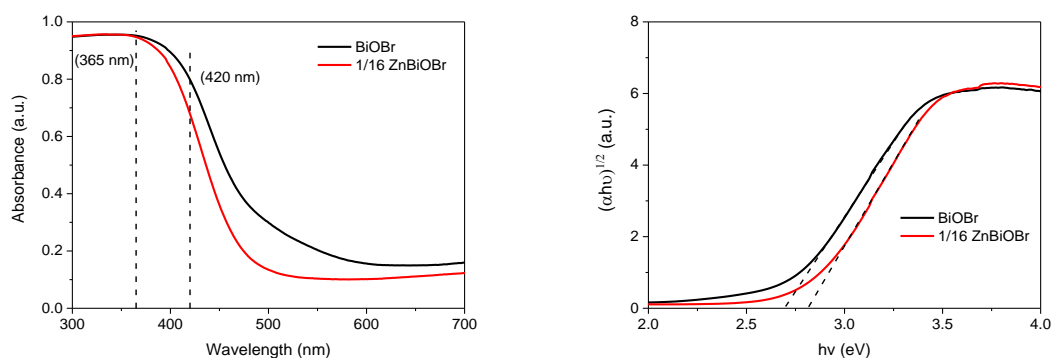
Figure 4-4 UV-vis absorbance spectrum of BiOBr-H and 1/16 ZnBiOBr-H (a) and the Tauc plots of two samples (b)

4.3.3 Photocatalytic performance

The photocatalytic degradation is an effective measurement to evaluate the overall performance of the photocatalysts. It is well known that the morphology, energy band structure and light absorption will have important influence on the degradation process. Prior to light-on degradation, there was a 75-min quiet time in the dark for the establishment of the equilibrium of RhB adsorption-desorption on the surface of samples. During the process, the changes of the RhB concentration in the solution were recorded. As presented in Figure 4-5, more RhB molecules are adsorbed onto 1/16 ZnBiOBr-H than BiOBr-H, which are both more than that on the irregular BiOBr. Normally, the amount of molecule absorption can be related to the surface area of absorbent. Assuming only one-layer RhB adsorbed on the photocatalyst's surfaces, the whole surface area of the material can be calculated by dividing adsorbate mass. Given that the diameter of RhB molecule is 1.5nm, the surface areas of both BiOBr and ZnBiOBr can therefore be estimated in terms of absorption amount presented in Table 4-2. The calculated specific surface areas of BiOBr and ZnBiOBr are listed in Table 4-2.
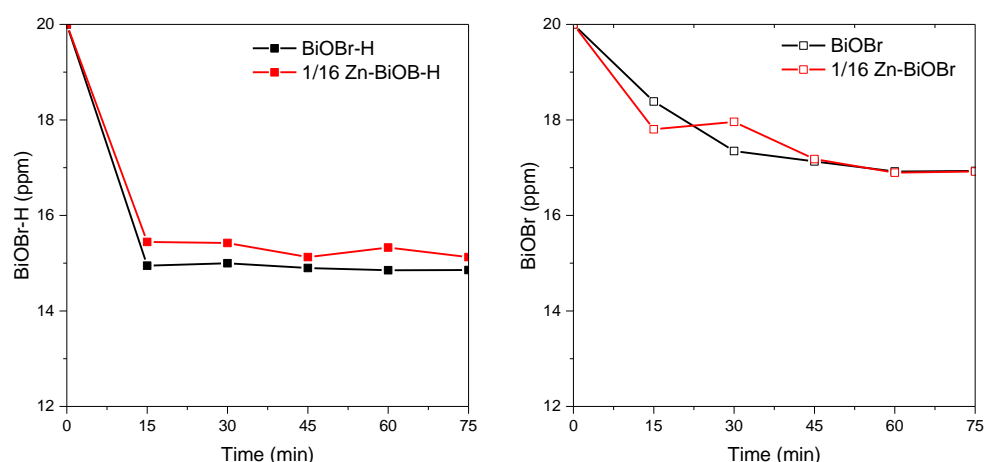
Figure 4-5 RhB adsorption-desoprtion eqilibirum on the surface of BiOBr-H and ZnBiOBr-H samples

The photocatalytic degradation is an intrinsic surface reaction; the surface area is closely related to the rate of the reaction. According to Figure 4-6 (a), pure BiOBr-H exhibits a higher photocatalytic activity over 1/16ZnBiOBr-H in RhB degradation. Moreover, comparing the results shown in Figure 4-6 (b), the hierarchically structured samples outperformed the degradation performance of irregular samples. The kinetics plots presented in Figure 4-6 (c) and (d) indicate that RhB degradation on BiOBr-H and ZnBiOBr-H follows the pseudo-first-order kinetics model, $\ln(C/C_0)=-kt$, where C and C_0 are the concentration of the dye in solution at time t and beginning, respectively; k here is the reaction rate constant. Comparing the kinetic constants (k) and the photodegradation performance, the hierarchical BiOBr and ZnBiOBr are more active photocatalysts over irregular ones, which can be ascribed to the difference in two aspects: the enhanced light absorption and larger surface areas.

To identify the contribution of each aspect, the specific kinetics constant k' were also calculated through dividing the k values by the adsorption amount of RhB, which is proportional to the absorbent surface area. Here the specific kinetics k' represents the photocatalytic reaction rate per unit area suggesting the influence from the light absorption. Comparing the k' list in Table 4-2, BiOBr-H shows the highest k', followed by BiOBr, 1/16ZnBiOBr-H and 1/16 ZnBiOBr, which is in the same sequence of their light absorption results. Moreover, it is worth noticing that the k' of hierarchical samples is almost twice of irregular ones, while the difference of k' between the hierarchical and the irregular is dramatically narrowed down. It is clear that the large surface area due to the hierarchical structures play a dominant role in the photocatalytic degradations.
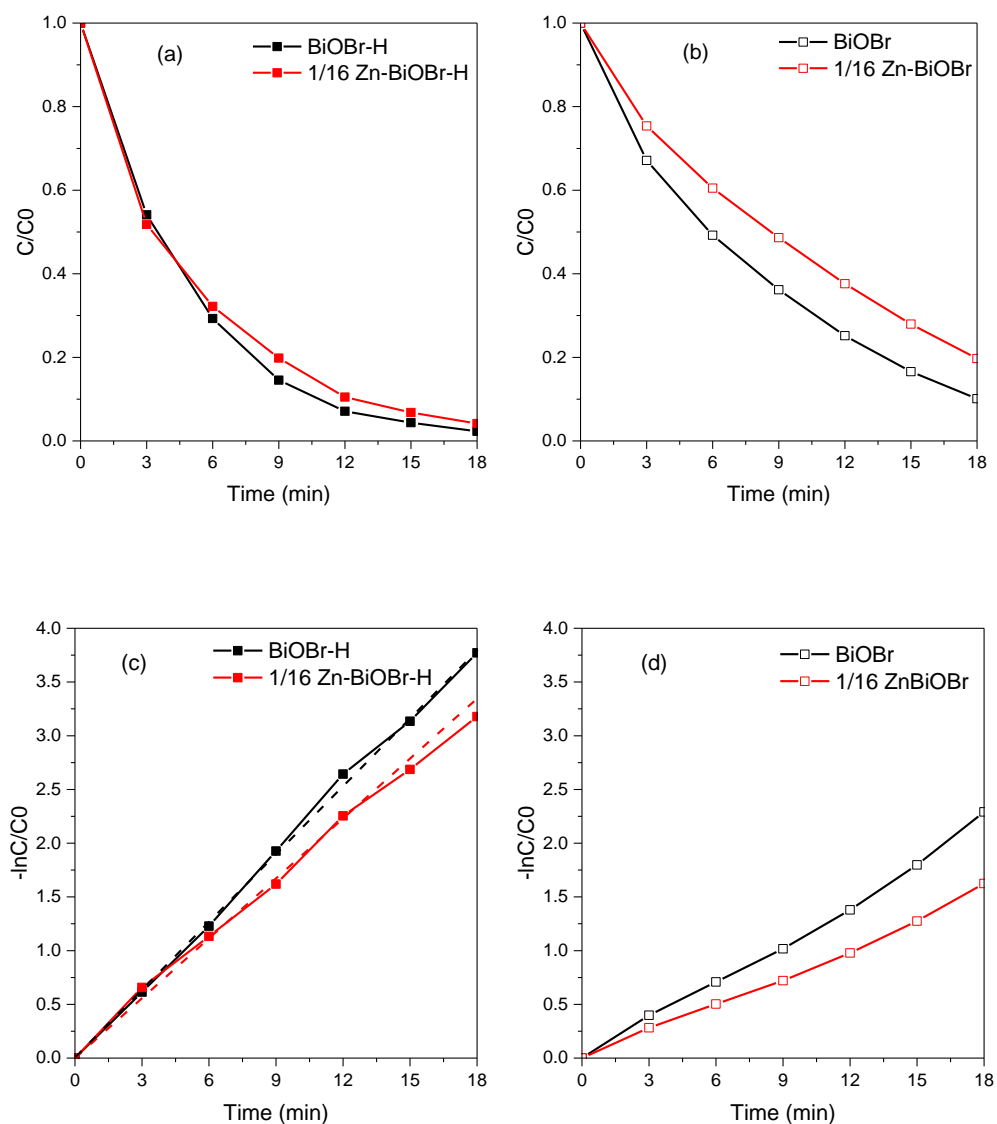
Figure 4-6 Photocatalytic performance of BiOBr and ZnBiOBr in heirarchical and irregular structures: (a), (b) Photocatalytic degradation performance of BiOBr and ZnBiOBr in hierarchical structures and structures; (c),(d) the reaction kinetics plots of BiOBr and ZnBiOBr in hierarchical structures and structures

Table 4-2 Specific surface area and photodegradation constant rate of hierarchical and irregular BiOBr and ZnBiOBr

Samples	BiOBr-H	BiOBr	1/16 Zn-BiOBr-H	1/16 ZnBiOBr
Dye absorption (mg/g)	4.75	2.96	5.14	2.97
Specific area (m^2/g)	10.55	6.57	12.53	6.57
k	0.2174	0.1231	0.1876	0.0962
k' (=k/SSA)	0.0457	0.0416	0.0365	0.0324

4.3.4   Photoluminescence

The large specific surface areas of hierarchical samples are often associated with rich surface defects that exert tremendous influences on the charge recombination and thus photocatalytic performance of the BiOBr-H and Zn-BiOBr-H. In principle, large amount of defects may result in deep intra-band gap states that impede carrier transport, whereas shallow traps may promote carrier transport via the rather inefficient process of diffusion [163]. It's important to understand the chemical nature of these traps so that they could be manipulated for a particular application.

The photoluminescence (PL) spectra of BiOBr-H and 1/16ZnBiOBr-H shown in Figure 4-7 reflect the charge recombination from the materials under 350nm ultraviolet irradiation. The normal emission of BiOBr nanoparticles is dominated by PL arising from the recombination of trapped electrons with valence band holes, leading to a broad spectrum with a peak in the black. However, when Zn was introduced into the materials, a higher energy emission ("green PL") was observed in the spectrum, arising from the recombination of mobile electrons with trapped holes, which we assign to oxygen-vacancy centres. Because both types of recombination depend on the spatial coincidence of trapped and mobile charges, the PL intensity is greater

when transport is hindered, while lower as the charges are more mobile (as in sintered porous films used for solar energy conversion). The PL is quenched by oxygen at the surface, the PL of porous films is much more strongly affected by oxygen than that of dense films. Here, the higher intensity PL response from pristine BiOBr-H indicates a higher charge recombination within the pristine materials and more well-ordered porous structure in 1/16ZnBiOBr-H.
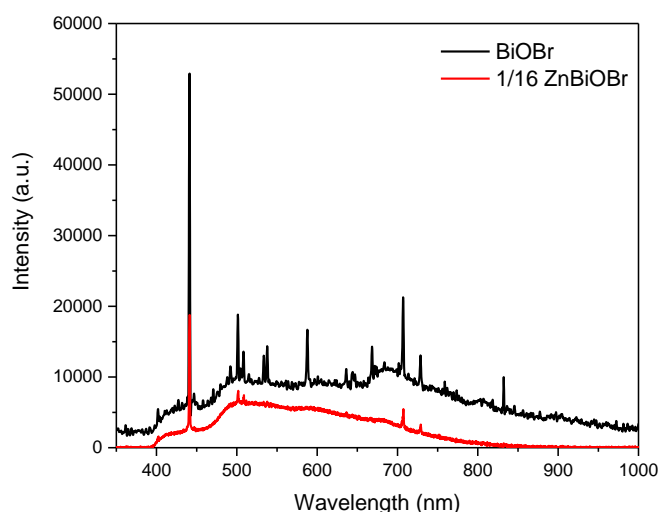
Figure 4-7 Plots of photoluminescence spectra of BiOBr-H and 1/16ZnBiOBr-H

4.3.5 Photoelectrochemical characterisations and energy recovery from wastewater

4.3.5.1 Mott-Schottky

The energy band position is the key factor of photocatalysts for energy recovery, because the position of the VBM and CBM determine their Redox ability in the photocatalysis and/or photoelectric catalysis. In this work, for recovering energy from organics in wastewater, the VBM of the photocatalyst should be strong enough to oxidise the organics in the solution. Consequently, analysis of energy band position is critical in understanding its photoelectrochemical reaction process. Mott-Schottky spectrum offers a mean to investigate the flat band potentials of the as-prepared materials. According to Figure 4-8, the M-S plots of pure and Zn-doped BiOBr display negative slopes in their linear regions, indicating they are n-type semiconductors.

The energy band positions of the samples can be further calculated according to the Mott-Schottky equation:

$$\frac{1}{C^2} = \frac{2}{A^2 e \varepsilon \varepsilon_0 N_D}\left(E - E_{fb} - \frac{k_B T}{e}\right) \tag{2}$$

where N_D is the charge carrier density, ε_0 is the permittivity in a vacuum, ε is the dielectric constant of the material, E is applied potential, T is the absolute temperature, e represents the elementary charge and k_B is the Boltzmann constant. The flat-band potentials can then be determined by extrapolating the straight line to the x-axis to obtain intercept which corresponds to the value of $E_{fb} + \frac{k_B T}{e}$. As an n-type semiconductor, the conduction band potential is close the flat-band potential (E_{fb}). Typically taking the difference between conduction band bottom (CBM) and E_{fb} as ca. 0.2 eV, therefore the edge of conduction band was calculated and displayed in Table 4-3. The E_{fb} of the BiOBr-H located at -0.43 eV (vs. SCE), while the E_{fb} of 1/16ZnBiOBr-H extended to deeper -0.48 eV (vs. SCE).
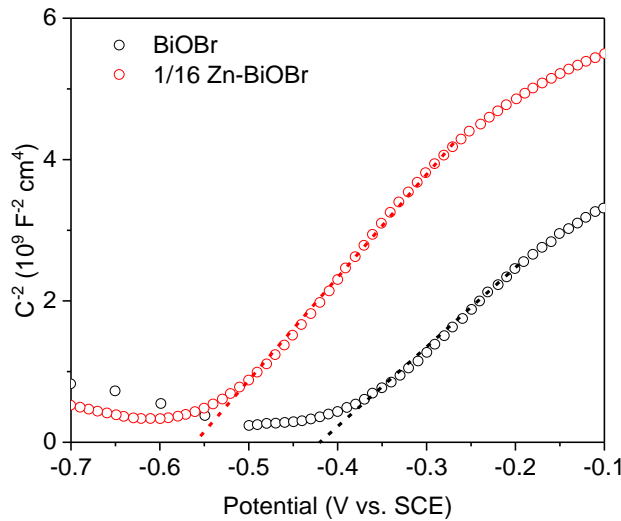
Figure 4-8 Mott-Schottky plots of BiOBr-H and 1/16ZnBiOBr-H

The shift of the flat band corresponded to the shift of the conduction band, indicating uprising of the conduction band when Zn dopant was incorporated into the material. And according to the band gap given by the UV-Vis spectra, the valence band bottoms (VBM) were also calculated in Table 4-3. The VBM of 1/16ZnBiOBr-H becomes slightly more positive than the pure BiOBr. The detail band structure diagram of the materials was depicted in Figure 4-9 based on the obtained result with respect to the potentials of water splitting (at pH=0). From Figure 4-9, both pure BiOBr-H and 1/16ZnBiOBr-H showed more negative potential than the H$_2$ evolution exhibited potential for water splitting.
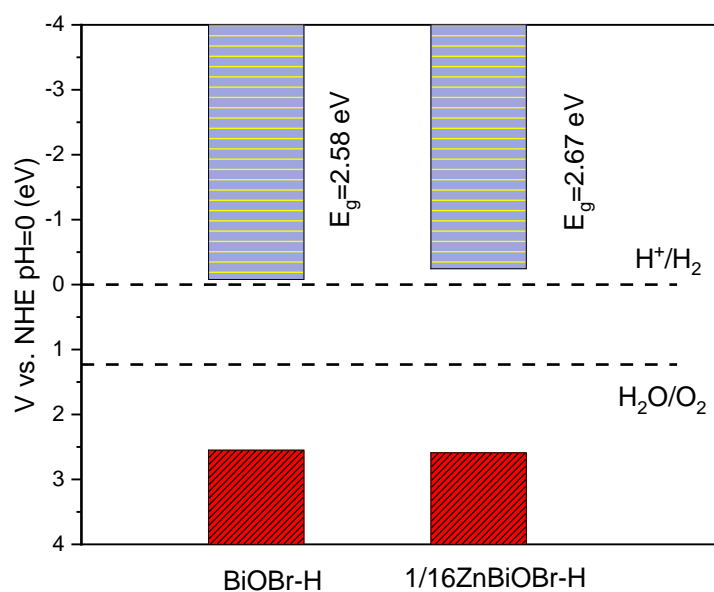
Figure 4-9 band position of the pure BiOBr-H and 1/16ZnBiOBr-H with the reference to the NHE at pH=0

Table 4-3 Electronic band position of BiOBr-H and 1/16ZnBiOBr-H

Samples	E_g (eV)	E_{fb}(eV vs. SCE)	E_c(eV vs. NHE)	E_v(eV vs. NHE)
BiOBr-H	2.68	-0.43	-0.03	2.65
1/16Zn-BiOBr-H	2.81	-0.55	-0.15	2.66

4.3.5.2   Hydrogen evolution
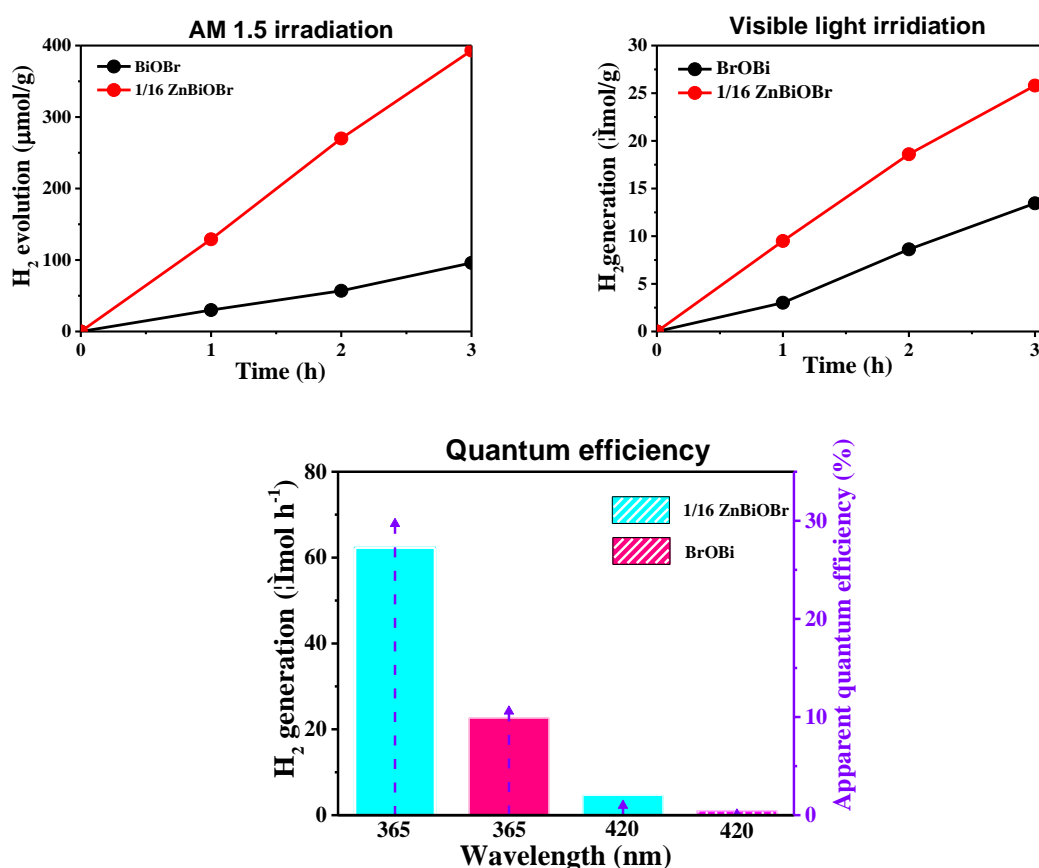
Figure 4-10 Photocatalytic hydrogen evolution of BiOBr and 1/16 ZnBiOBr under AM1.5 (a) and visible (b) irradiation, the photocatalytic hydrogen evolution rates under single-wavelength light and the corresponding QE.

The hydrogen evolution of BiOBr–H and 1/16 ZnBiOBr-H was carried out under AM 1.5 and visible light irradiation for 3 hours, respectively.As shown in Figure 4-10 (a) and (b), the H_2 production performance under full arc is 131 $\mu molg^{-1}h^{-1}$, which is apparently higher than that under the visible light. The apparent quantum efficiencies (QEs) of the hydrogen production were calculated to evaluate the solar energy conversion ability of the materials using Equation:

$$QE = \frac{2\times(evolved\ H_2\ molecules)}{(incident\ photons)} \times 100\% \qquad (3)$$

The QEs of BiOBr-H and 1/16ZnBiOBr-H were respective 22.6 % and 62.3 % under full arc irradiation of 300W Xenon lamp, which dropped dramatically down to 0.84 % and 4.6 % under visible light. The results suggest that these hierarchical architectures are more effective under UV light. Here the enhancement of hydrogen evolution of 1/16ZnBiOBr-H compared to BiOBr-H can be attributed to the upshifted CBM arisen from Zn doping which promotes the reducibility of the

photo-excited electrons of ZnBiOBr-H. On the other hand, the VBM of ZnBiOBr is more positive than that of pristine BiOBr, namely more oxidative in photocatalytic oxidation.

4.3.5.3   Chronoamperometry

The temporal photocurrents were measured at open circuit potential (OCP) in various electrolyte solutions, which contain different organics to model the conditions of typical wastewaters. The acquired plots of photocurrent against irradiation time (I~t) under light on-off cycles on the pristine and Zn-doped BiOBr-H photoanodes are compiled in Figure 4-11. The I-t plots clearly show the Zn-BiOBr-H specimen displays weaker temporal photocurrent than that of BiOBr photoanode under all the adopted conditions. Since the photocurrent at OCP is related to the surface effective photogenerated charge carriers [164, 165], the photocurrent values under designed electrolyte solutions allow weighing the impact factors to photoelectrocatalytic activities.

The photocurrents acquired from 0.5M Na_2SO_4 electrolyte solution reflect the intrinsic photoelectrochemical nature of the samples. It can be seen from Figure 4-11 (a) that the photocurrent of the 1/16ZnBiOBr-H is significantly lower than that of BiOBr-H, which may be due to its relatively weaker light absorption of 1/16ZnBiOBr-H. The photocurrent ratios between BiOBr-H and 1/16Zn-BiOBr-H is about 9:5, suggesting the extractable photogenerated charge carriers are reduced 55 % because of Zn substitution of 1/16 in the BiOBr matrix.

It is noticeable that the photocurrent ratio is much higher than the surface photocatalytic kinetic constants in dye photodegradation, which inspires us to investigate how the dye would contribute to the photocurrents on each sample. The photocurrents measured in the RhB-containing (20 ppm) 0.5M Na_2SO_4 solutions enable to identify the dye sensitisation effects on the photoelectrodes. Greatly enhanced photocurrents induced by RhB can be observed on the both photoelectrodes (Figure 4-11b). The photocurrent enhancements relative to those acquired from RhB-free 0.5 M Na_2SO_4 electrolyte solutions are increased 54.3% and 22.7% on the pristine BiOBr and 1/16ZnBiOBr-H photoanodes, respectively. Such enhancements are due to electron injection from excited RhB to CBM of the photocatalysts and then exiting to the external circuit. The results clearly reveal the RhB photosensitisation exerts profound influences on the photocatalysis of the

catalysts, whereas the intrinsic photogenerated charge carriers remain the core factor to determine their apparent photocatalytic activities.

Moreover, it is worth noting that the photocurrent sparkles for the photo-anodes under dye sensitisation conditions are distinct from those without dye, mainly longer discharging spans, suggesting the dye sensitisation also prolong the charge decay time [166]. The in-depth investigation to the lifetime of the surface charge carriers is ongoing.
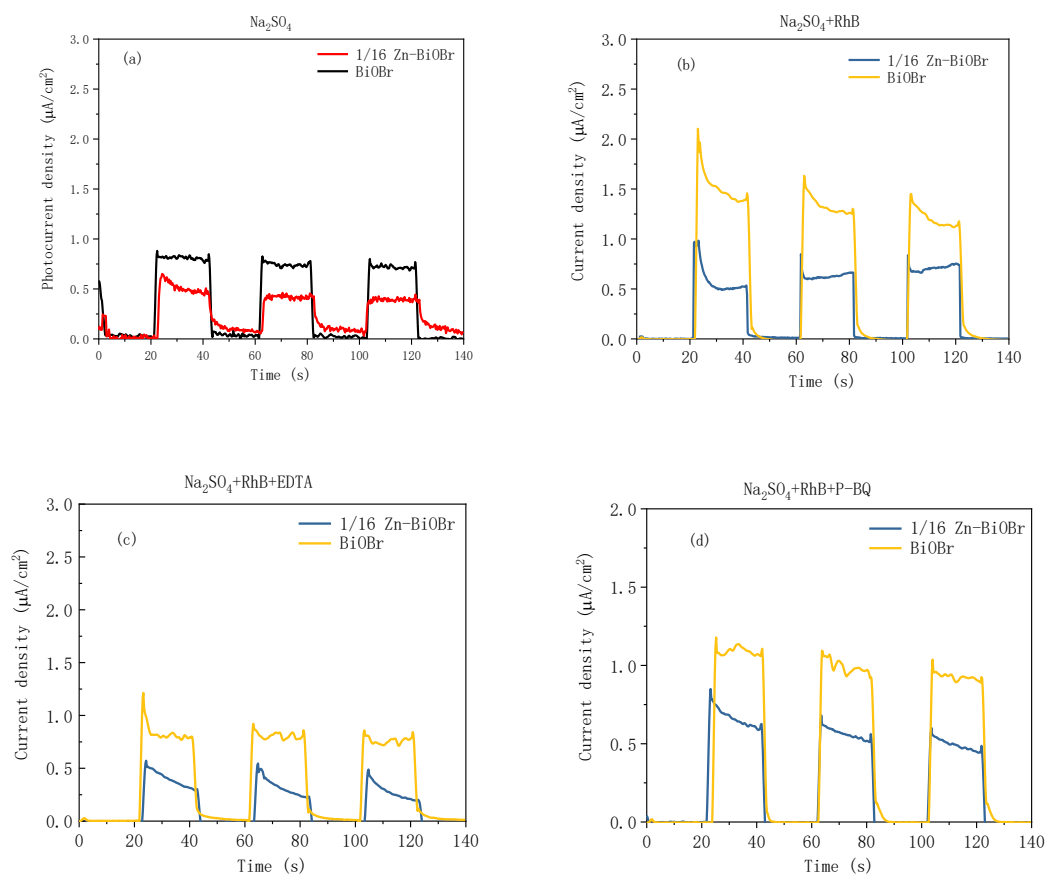
Figure 4-11 Photocurrent response of BiOBr and ZnBiOBr with hierarchical structures and irregular structures
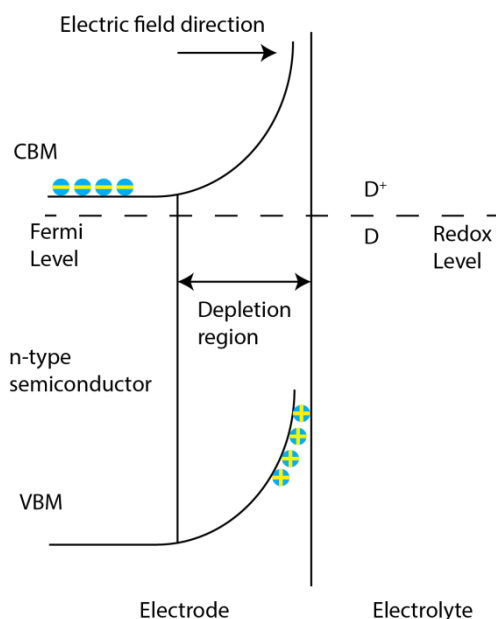
Figure 4-12 Electron flow in n-type semiconductor electrode under irradiation with solution containing redox couple D/D$^+$

4.3.5.4   Energy recovery

In order to evaluate their potentials for energy extraction from aqueous organic wastes, a series of photocatalytic electricity generation tests on the BiOBr-H and 1/16ZnBiOBr-H were carried out in two electrode systems, where a Pt cathode was used as counter electrode without involving of reference electrode. In photo electrochemistry cells, the semiconductor electrodes act as electron pump, converting the light to electrons flow. As shown in Figure 4-12, the photon induced charge carriers was separated on the surface of electrode which is similar to what occurs at p-n junctions. However, in the liquid junction cells, because electrons and holes are normally not stable in the solution, their transportation through the liquid rest with occurrence of chemical reactions on the electrode-solution interface. In this case, it provides a means of energy conversion from storable chemicals to electricity [167]. The results presented in Figure 4-13 illustrate their photocurrent differences under the visible light. The photocurrent response in Na_2SO_4 reflected corresponds to the intrinsic solar energy conversion on the materials, while the respective addition of RhB, glucose and citric acid into the Na_2SO_4 solution, stronger current responses are observed on both BiOBr-H and 1/16ZnBiOBr-H systems, suggesting more energy has been pumped into the circuit.

The results in Figure 4-13 show a slightly stronger photocurrent response on the BiOBr-H than that of 1/16ZnBiOBr-H system in Na_2SO_4 solution. This is due to the fact that the photoelectrical energy recovery is not determined by the band position

but the light absorbance of the photocatalysts. Meanwhile, the photoluminescence spectra shown in Figure 4-7 suggest that the charge recombination on BiOBr-H is more significant than that on ZnBiOBr in wide spectrum range. Therefore, there are no significant difference in the photocurrent responses of the two hierarchical samples in Na_2SO_4 solution. Meanwhile, the calculated specific kinetics constant k' values (Table 4-2) also verified the influence of light absorption in the photocatalytic degradation.

The additional energy release can be ascribed to the photo-driven reactions with the organics as "fuels" on the surface of BiOBr-H and 1/16ZnBiOBr-H samples. These are due to the fact that the organics can be hole scavengers, leading to more photo-excited electrons pumping into the Pt cathode. The electrons can reduce H_2O to generate H_2 or reduce O_2 to generate superoxygen radicals which subsequently converts to hydrogen peroxide (H_2O_2). Therefore, in the photoelectrocatalytic energy recovery process, more current responses can be obtained by photodegradation of the "fuel" on the photoanodes. According to the band structure diagrams shown in Figure 4-9, the VBM of 1/16Zn-BiOBr-H is slightly lower (more positive) than that of BiOBr-H, indicating the higher oxidation power of the former sample in the photocatalytic organic oxidation reactions.

The dependence of temporal photocurrents of the BiOBr-H and 1/16ZnBiOBr-H on the organics are compared systematically in Figure 4-13. It can be seen that the existence of organics did enhance the photocurrent responses, though they are acidic organic, citric acid in this study, is more effective than the neutral organics. More interestingly, the ratios of photocurrent on BiOBr-H to that on 1/16ZnBiOBr-H are almost same to that without organic in the Na_2SO_4 solution, suggesting that the light absorption is still the crucial factor in determining the energy recovery. This is different from that in water splitting.
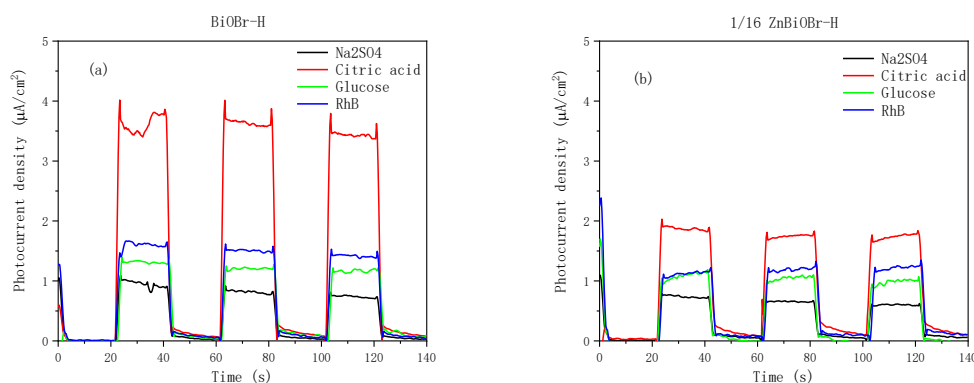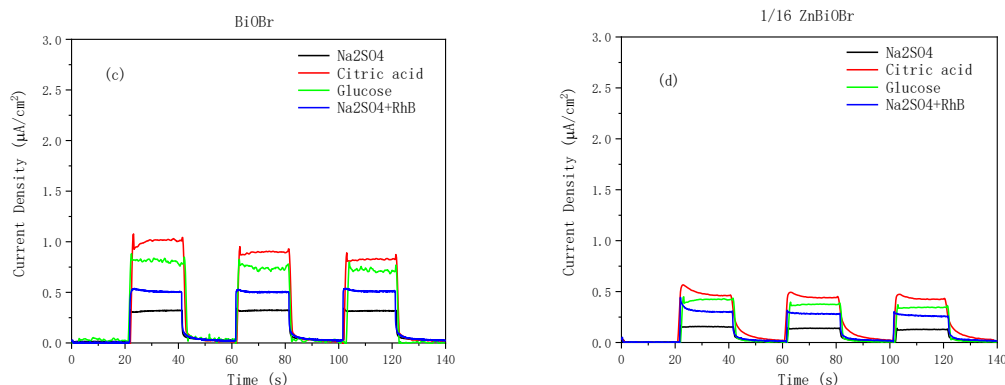
Figure 4-13 Photo-current density transient with light on/off for hierarchical and
irregular BiOBr and ZnBiOBr

The stability of the energy recovery is also of utmost importance in the practical applications. On that account, photocatalytic stability of each sample was characterised in the long-time chronoamperometry tests in the dual-electrode system. The results presented in Figure 4-14 show that the photocurrent generated from the "fuels" is gradually declined over time, which is due to the consumption of the "fuels" during the photocatalytic reactions.
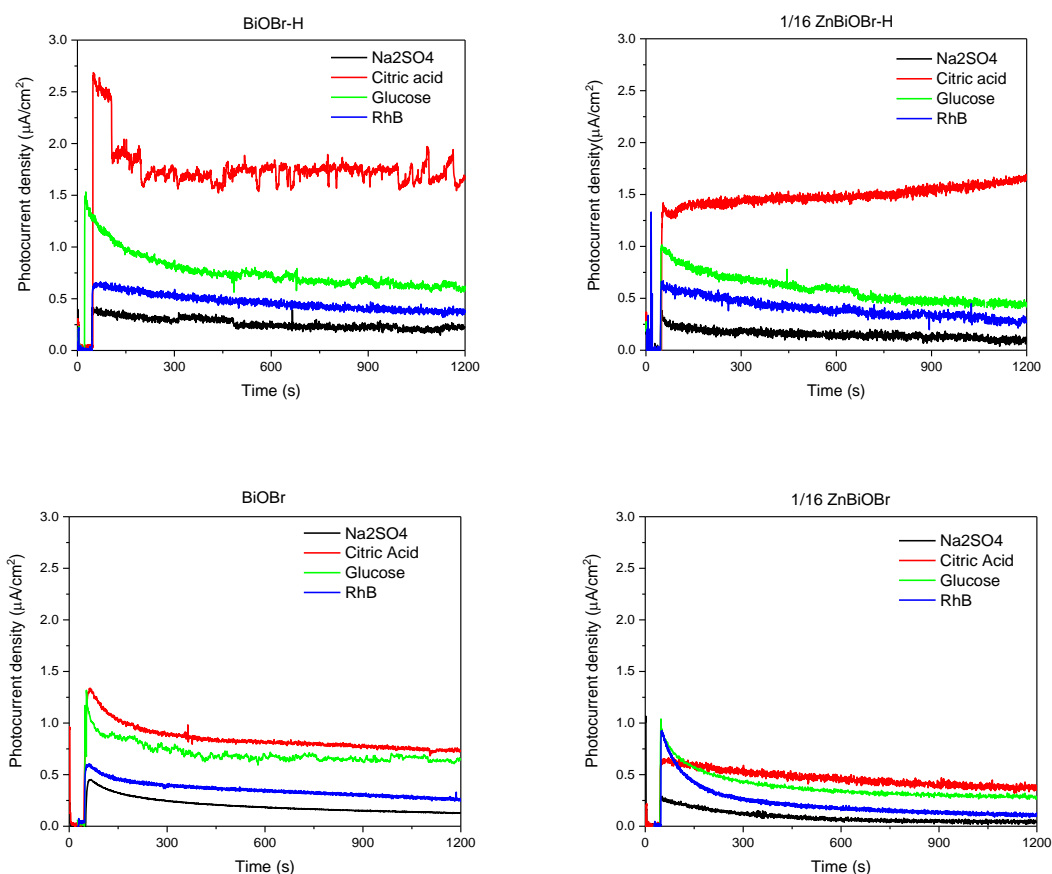
Figure 4-14 Photocurrent response under long-time irradiation

Moreover, the intrinsic efficiency of the photocatalysts in the cells with various "fuels" can be evaluated via the current-voltage (J-V) plots acquired from the linear sweep voltammetry (LSV). The obtained LSV plots were then transformed into the current-power (J-V) plots and presented in Figure 4-16 according to the composition of the electrolyte. The fill factor (FF) was also calculated according the following equation:

$$FF = \frac{P_{max}}{J_{sc} \times V_{oc}} \tag{4}$$

Where P_{max} stands for maximum power density, J_{sc} is short-circuit current density and V_{oc} is the open-circuit voltage under the irradiation. The FF represents the difference between the actual maximum power density output from the cell and theoretical maximum power, which is an important index describing the overall efficiency of the photovoltaics device. The calculated values listed in Table 4-6 shows the energy extraction efficiency of the catalyst from different type of chemicals.

Under the darkness, the V_{oc} between the working electrode (WE) pure BiOBr and the counter electrode (CE) Pt was -0.43 V and the J_{sc} was 0.15 µA/cm^2. Because the as-prepared BiOBr-H and 1/16Zn-BiOBr-H are n-type semiconductors, the inner built electric field is in the direction from bulk of the materials toward the interface with electrolyte. Thus, when photo-induced electrons hole pairs (e$^-$-h$^+$) forms on the WE, the electrons will exit the WE through external circuit and flow to the CE, meanwhile the holes will migrate towards the WE surface to reaction with organics or dissolved oxygen.

According to the results shown in the Table 4-4 and Table 4-5, the light excitation had made potential of WE more negative so that more electrons can be separated and move to the CE for the reactions. Also, it is worth noting that the J_{sc} of both BiOBr and ZnBiOBr are promoted when extra chemical "fuels" were brought into the electrolyte. As a photoelectrochemical cell, magnitude of the J_{sc} and V_{oc} stands for the maximum output voltage and current can be reached during the reactions.

BiOBr-H
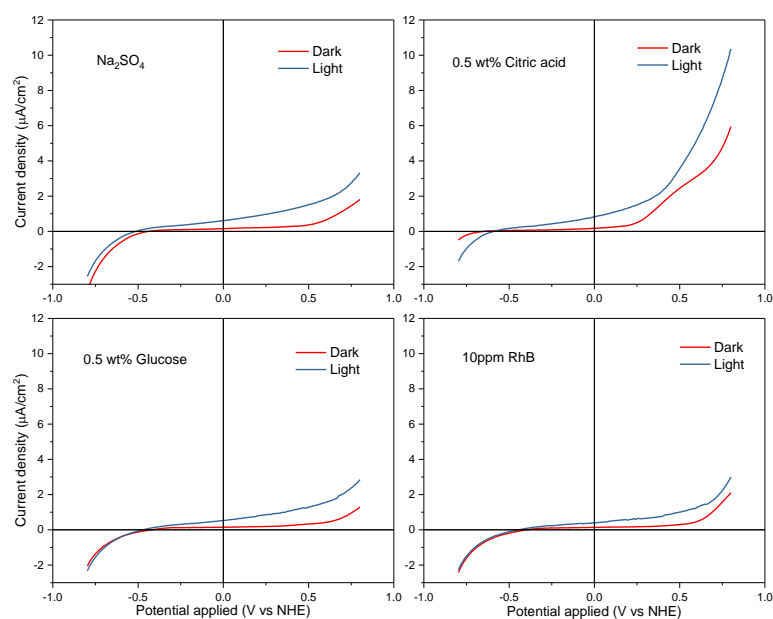
1/16 ZnBiOBr-H
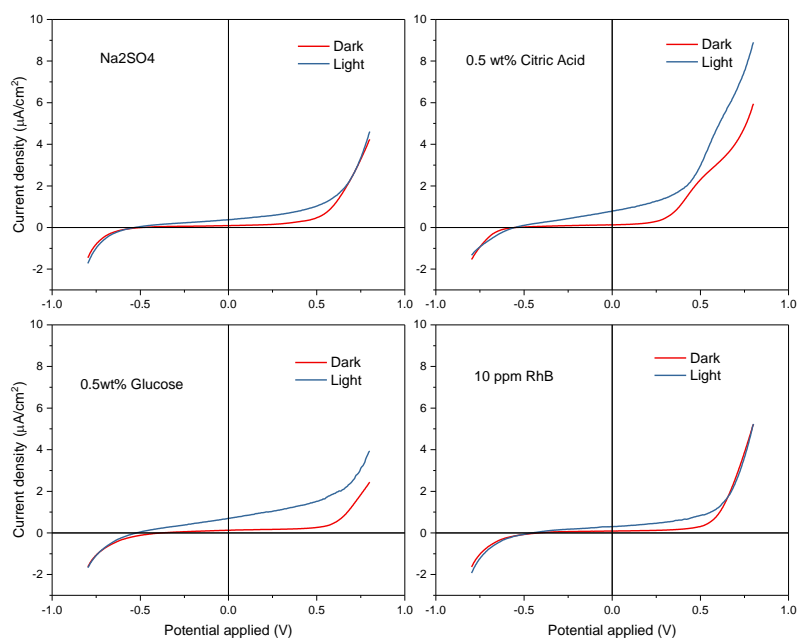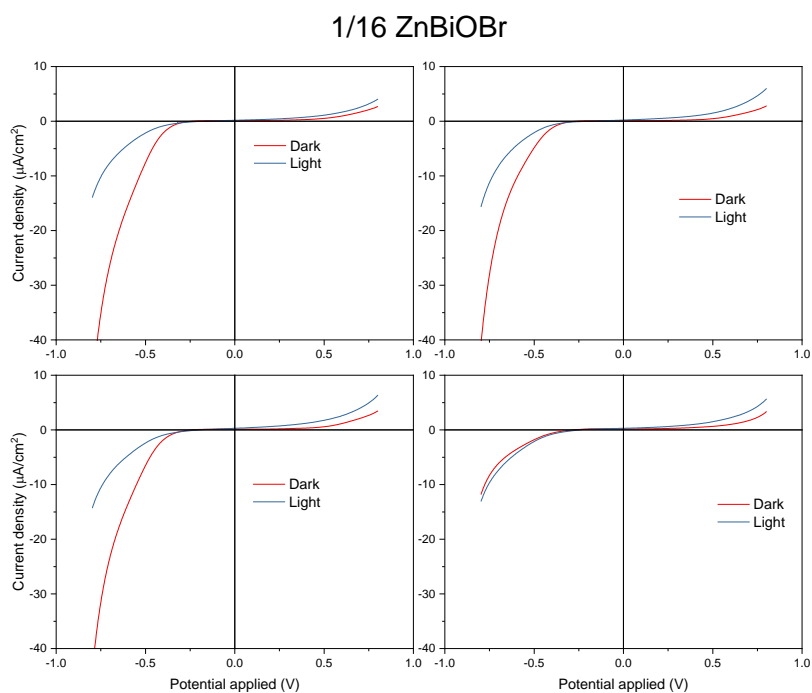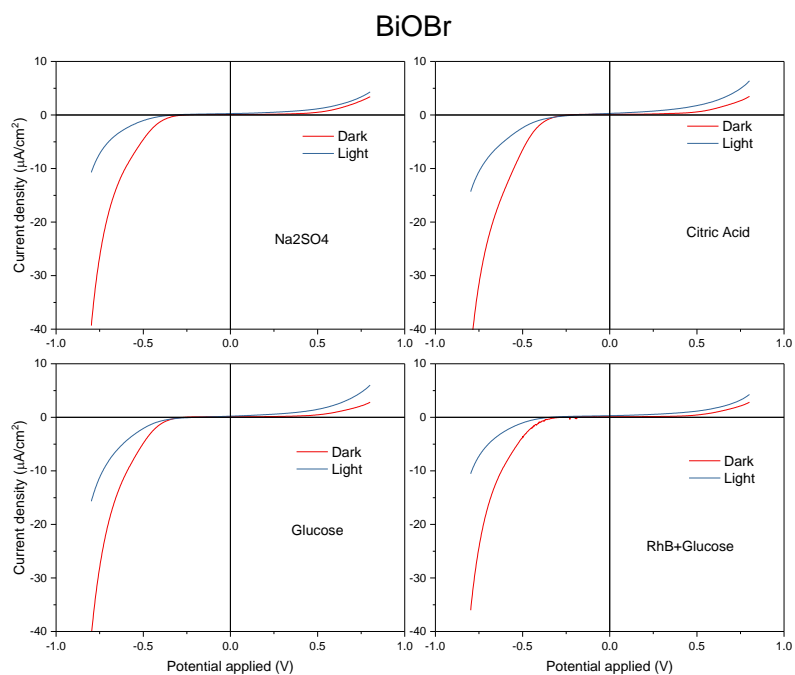
BiOBr

1/16 ZnBiOBr

Figure 4-15 Linear sweep voltammetry of BiOBr and 1/16ZnBiOBr (in hierarchical and irregular structures) under visible light irradiation in different fuels added electrolyte
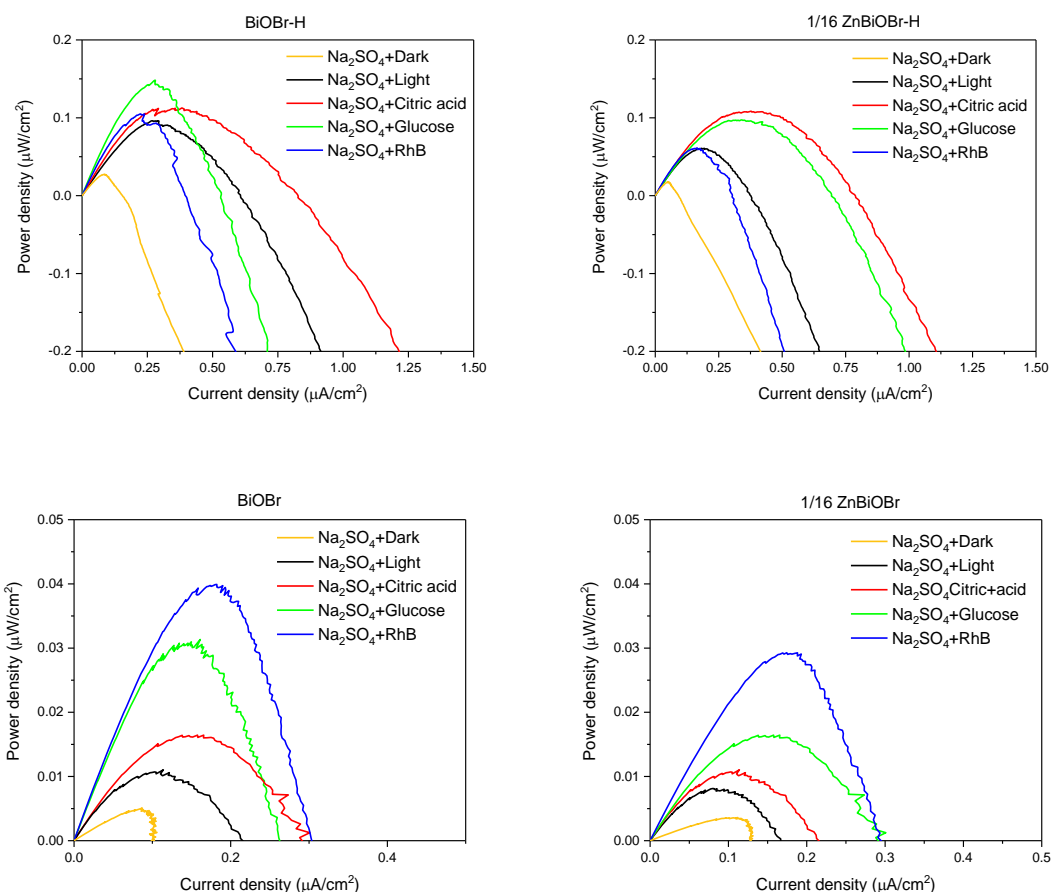
Figure 4-16 Current-power (J-V) plots for pure BiOBr and ZnBiOBr under visible light irradiation

Table 4-4 Open-circuit voltage of BiOBr and ZnBiOBr in different electrolyte under visible light irradiation

Test Conditions	Voc (V)			
	BiOBr-H	BiOBr	1/16 ZnBiOBr-H	1/16 ZnBiOBr
Na_2SO_4 Dark	-0.4387	-0.2629	-0.4948	-0.1409
Na_2SO_4 Light	-0.5119	-0.3215	-0.5314	-0.1726
Na_2SO_4+Citric acid Light	-0.5876	-0.1970	-0.5510	-0.1946
Na_2SO_4+Glucose Light	-0.4704	-0.1946	-0.5193	-0.1970
Na_2SO_4+RhB Light	-0.4436	-0.3386	-0.4489	-0.2434

Table 4-5 Short-circuit current density of BiOBr and ZnBiOBr in different
electrolyte under visible light irradiation

Electrolyte/ Conditions	Jsc ($\mu A/cm^2$)			
	BiOBr-H	BiOBr	1/ 16 ZnBiOBr-H	1/16 ZnBiOBr
Na_2SO_4 /Dark	0.1549	0.0988	0.0915	0.1278
Na_2SO_4 /Light	0.6071	0.2631	0.3768	0.1668
Na_2SO_4+Citric acid /Light	0.8280	0.2762	0.7889	0.2166
Na_2SO_4+Glucose /Light	0.5315	0.2853	0.6938	0.2927
Na_2SO_4+RhB /Light	0.3967	0.304	0.3037	0.2967

Table 4-6 Fill factors of various BiOBr and ZnBiOBr in different electrolyte under
visible light irradiation

Electrolyte/ Condition	Fill factor			
	BiOBr-H	BiOBr	1/16 ZnBiOBr-H	1/16 Zn-BiOBr
Na_2SO_4 /Light	0.3041	0.1267	0.3070	0.2672
Na_2SO_4+Citric acid/Light	0.2293	0.2825	0.2394	0.2565
Na_2SO_4+Glucose/Light	0.3737	0.3662	0.5928	0.2834
Na_2SO_4+RhB/Light	0.4511	0.3970	0.5938	0.4053

Conclusion

Hierarchically structured BiOBr and Zn-doped BiOBr were successfully prepared via a facile hydrothermal synthesis using PEG2000 as structure-direct agent. In contrast with previous prepared irregular BiOBr and Zn-doped BiOBr, the self-assembled microsphere structures not only possessed higher specific surface area, but also increased the light absorbance of the materials. The photocatalytic performance of the samples was evaluated in hydrogen evolution and photodegradation of RhB.

When Zn incorporated into the materials, an enhanced performance of BiOBr was observed in the hydrogen evolution, which can be ascribed to the uprising of the CBM of the ZnBiOBr due to the Zn-dopants. However, for the RhB photodegradation, the BiOBr showed superior photocatalytic activity to Zn-doped BiOBr. In a dual electrode photoelectrochemical cell, the energy recovery from photocatalytic degradation of dissolved organics, including glucose and citric acid, were also tested to evaluate the applications on the electricity generation from the wastewater. During the test, due to large surface area, the surface potentials of the hierarchical BiOBr and ZnBiOBr were remarkably changed by the adsorbed species in the solution. The results suggested that BiOBr-H benefited from the large light absorbance and large specific surface area displayed a more efficient energy conversion capability.

Chapter 5 PEG-Assisted Hydrothermal Synthesis of Hierarchical BiOBr/ZnO Heterojunction with Abnormal Photoelectrical Responses

5.1 Introduction

In the Chapters 4 and 5, the influences of Zn-doping on the structure and photo(electro)catalytic performance of BiOBr photocatalysts were clarified and rationalised. However, the Zn-doping levels are very restricted and higher Zn-doping amount will lead to isolation and segment of ZnO on the surface of BiOBr to form heterojunction. This phenomenon inspires us to further investigate the heterojunction of ZnO and BiOBr, in particular their hierarchical architectures due to the beneficial effects of the built-in electrical field across their interface and convenient fabrication.

ZnO is one of the most promising semiconductors, intensive efforts have been devoted to extending its application in the electrical and chemical engineering. Zinc oxide (ZnO) is a versatile semiconductor with a wide direct band gap (3.37eV) and large excitation binding energy (60 meV) [74]. In the past decade, researchers have endeavoured to synthesise nanoscaled ZnO materials with diverse morphologies, such as nanorod, nanowire, nanotube, quantum dot, nano spring, nano-helix, triangle, disk and ring, etc [168, 169]. Among them, ZnO nano-flakes have drawn special attention for their improving molecular transportation, enhancing light harvesting and large surface area, which increase the number of active sites and accelerate the surface photocatalytic reactions [170-172]. Additionally, the CB and VB of hierarchically structured ZnO can be engineered by reducing the size of building blocks to the nanoscale level and taking advantage of the quantum size effect [173].

However, ZnO, as a wide band gap semiconductor, is only ultraviolet light responsive. In consequence, it couldn't be harvest ~95% solar energy during the photocatalytic reactions. To improve the light harvesting on ZnO, heterojunction of ZnO and a narrow band gap semiconductor will be an effective approach to optimize the photovoltaic properties of ZnO. In fact, the combination of ZnO and second semiconductor will not only improve light absorption of ZnO, but aslo

reduce the charge recombination within the materials [13, 31, 174]. BiOBr, as described in the previous chapters, may be a promising option as the second semiconductor to form heterojunction with ZnO [14, 50, 175].

Based on the previous research progress reported in literature, we have successfully obtained hierarchical ZnO and BiOBr/ZnO-PEG heterojunctions. To achieve a hierarchically assembly structure in the materials, the hydrothermal synthesis was carried out in the preparation. The previous papers reported that nanostructured ZnO can be obtained preferentially through hydrothermal synthesis in a broad mild temperature range with the assistance of surfactant [58, 176]. Once surfactant is introduced into the hydrothermal system, the surface energy of individual crystal surface will be tuned and thus allow oriented growth to form different morphology of resultant ZnO nanomaterials.

The work in this chapter aims to develop a facile template-assisted synthesis of ZnO flakes and their heterojunctions with BiOBr nanoflakes[177], in which the polyethylene glycol (PEG) is adopted because it is able to guide the orientation of ZnO crystals in synthesis and is environmentally friendly[178]. Moreover, in order to further increase the photocatalytic performance of ZnO-PEG, ZnO-PEG coupling with varied amount of BiOBr was also prepared for investigation on physicochemical properties in solar energy conversion.

5.1.1   Materials synthesis

The preparation was via the following process: 1.10g $Zn(Ac)_2 \cdot 2H_2O$ and various amount of PEG-20000 dissolved in 15 ml distilled water and 60ml ethanol, 5 ml concentrated ammonia solution was then added under intensively stirring before addition of 0.4g sodium hydroxide. The obtained clear solution was directly transferred to oven to dry up for 5 hours under 120℃. After cooling down to room temperature, the precipitation was collected and washed alternatively with distilled water and absolute ethanol and dried in the air at 120℃ overnight to receive the hierarchical ZnO, denoted as ZnO-PEG (ZnO+0%BiOBr).

The as-prepared ZnO-PEG samples were then mixed with 40ml 0.05M KBr solution according to mole ratio between ZnO-PEG and BiOBr (5%, 10%, 15%). Under vigorous stirring for 3 hours in the beaker, 0.05M $Bi(NO_3)_3$ was dropwise added into the mixed solution. The obtained suspensions were aged overnight before filtration. The precipitation was collected and then rinsed with water and ethanol separately and transferred to the oven for drying under 80℃/4 hours. The received samples

are denoted as xBiOBr/ZnO, where x represents loading percent of BiOBr, of 5, 10 and 15 in wt%, respectively.

5.1.2 Characterisation

The morphology and structure of the as-prepared products were characterized by using Quanta 200 FEG field-emission scanning electronic microscopy (FESEM) operated at an accelerating voltage of 10.0 kV, JEOL-2010 transmission electron microscopy (TEM) operated at 200 kV, Rigaku Smartlab Pro X-ray diffractometer (XRD) with Cu Kα radiation (1.5418 Å).

The photocatalytic activity of the prepared samples was evaluated by photocatalytic decolourization of methylene blue (MB) aqueous solution under visible-light irradiation using a 300WXe lamp (15 cm above the testing dishes) equipped with a 400 nm cut-off filter to remove UV. In the typical photocatalysis experiments, 0.1 g of the prepared photocatalyst powder was dispersed in a 100 mL MB aqueous solution with a concentration of 10 ppm in a beaker.

5.2 Results and discussion

5.2.1 The crystallinity and morphology

In Figure 5-1, the XRD patterns indicate a wurtzite zinc oxide (hexagonal phase, space group P63mc, JCPDS: 890511) with high crystallinity. The calculated lattice constant is a=3.2490A, c=5.2040A, respectively. In comparison with XRD pattern from ZnO-Ref, ZnO-PEG sample displays stronger relative intensity of (101) surface, suggesting the (101) facet constructs the most exposed surface. In addition, XRD patterns of BiOBr/ZnO-PEG samples were gradually broadened their FWHMs (full width at half maximum): The XRD patterns of the ZnO-PEG sample show rather broader FWHMs than ZnO-Ref which are lower as well. The differences of the XRD patterns for ZnO-Ref (JCPDS: 890511) and ZnO-PEG should be caused by the PEG surfactant: In the synthesis, the long-chain PEG surfactant can be selectively adsorbed onto the ZnO crystal seeds as they formed initially. We propose the zinc coordinates $[Zn(NH_3)_4]^{2+}$ well coordinate with –OH chain of the surfactant PEG, hence, once adding NaOH into the precursor solution, zinc oxide precipitation took place on the PEG which guides the formation of ZnO-PEG nanospheres in the hydrothermal treatment.

However, when varied amount of BiOBr was loaded onto ZnO-PEG, the peak from BiOBr can be observed in the ZnO-PEG heterojunctions. The intensity of the peaks from BiOBr becomes stronger as increasing loading amount of BiOBr on ZnO-PEG
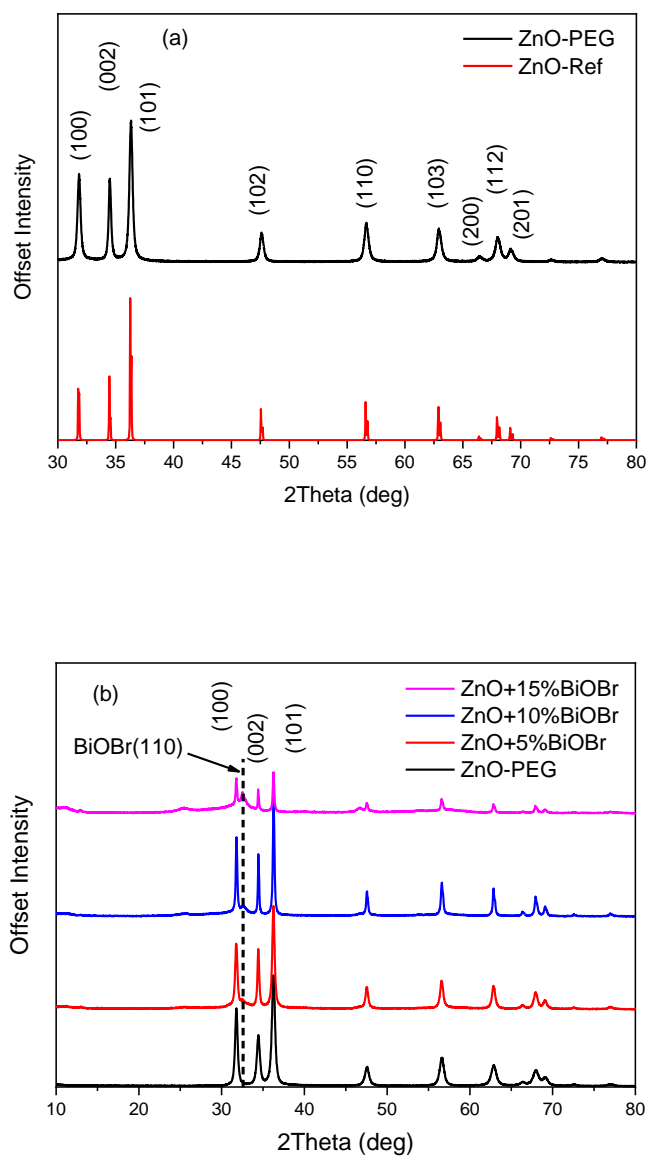
Figure 5-1 XRD patterns of ZnO-PEG and BiOBr/ZnO couplings: (a) XRD patterns of hierarchically assembled ZnO; (b) the XRD patterns of ZnO with varied amount of BiOBr loading
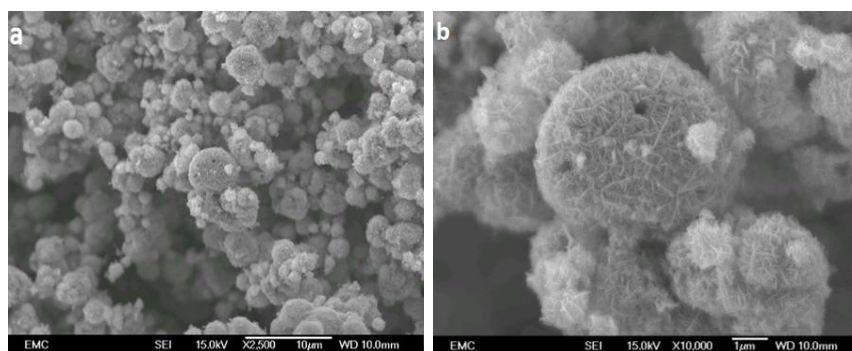
Figure 5-2 SEM images of ZnO-PEG and BiOBr/ZnO-PEG couplings(a),(b)the SEM images of prepared ZnO with PEG; (c),(d) the SEM images of ZnO with PEG
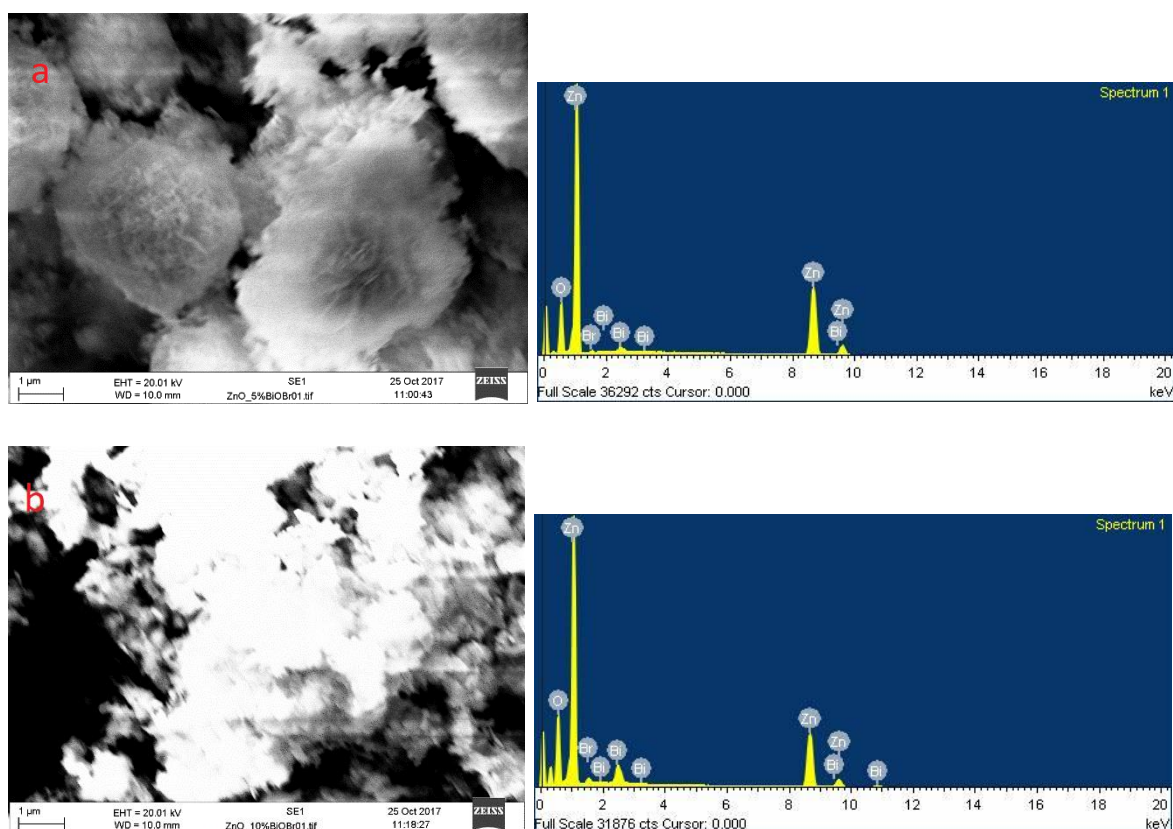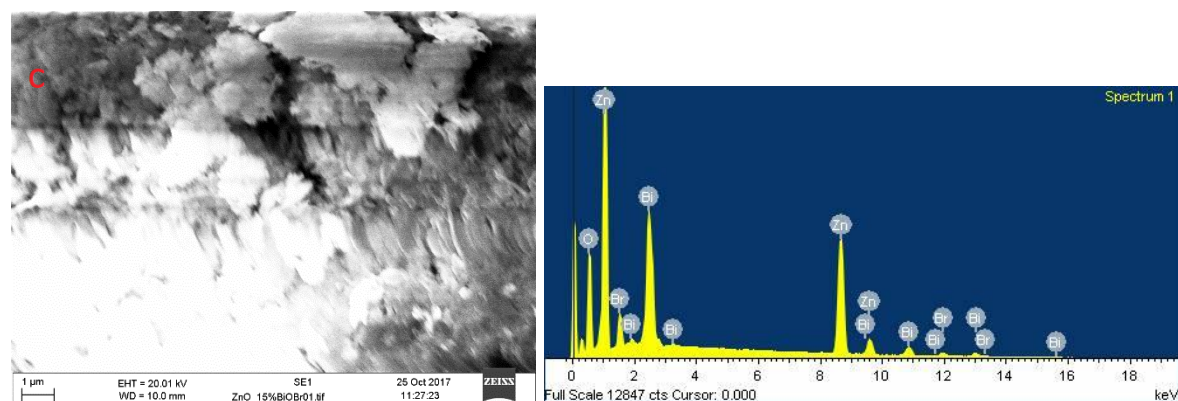
Figure 5-3 SEM image and EDX patterns of ZnO-PEG after loading with BiOBr: (a) ZnO-PEG with 5% BiOBr loading; (b) ZnO-PEG with 10% BiOBr loading; (c) ZnO-PEG with 15% BiOBr loading

Figure 5-2 shows the SEM images of the ZnO samples synthesised with existence of PEG-20000. These pictures unveil the overall appearance of the materials and the right-hand side show the enlarged details of each group. (a) and (b) are ZnO-PEG under the SEM. As it shown in the Figure 5-2, ZnO prepared with PEG shows nanorods co-existing with the flakes. In the Figure 5-2 (b), sphere with a diameter of 3 μm were presented in a closer examination of this sample. Some holes in the surface may a hollow interior of this nano structure. According to Figure 5-2**Error! Reference source not found.** (a), the diameters of these nano-spheres are not evenly distributed, which ranges from 0.5 μm to 5 μm. After loading with BiOBr as shown in Figure 5-3, the hierarchical structures of ZnO was gradually covered up by the random aligned BiOBr particles. In Figure 5-3 (a), (b), (c), the SEM images became pale and blurred with increasing BiOBr loading amount, which probably is due to surface charging because the SEM images were taken in BSE mode.

In addition, the quantitative elemental composition of the materials was analysed using EDX (Energy Dispersive X-ray), which confirmed existence of the increasing amount of BiOBr was combined with ZnO-PEG in the BiOBr/ZnO-PEG.

5.2.2 Optical properties

Figure 5-4 (a) depicts the UV-vis diffuse absorption spectra of the ZnO-PEG and BiOBr/ZnO-PEG heterojunctions. As shown in Figure 5-4, a sharp reduce in the light absorption can be observed in the spectra of all the samples at the wavelength region around 400nm, indicating a strong ultraviolet absorption of ZnO-PEG and BiOBr/ZnO-PEG composites. With increasing of BiOBr loading amount, the light absorption of the BiOBr/ZnO-PEG composites are slightly reduced within the region from 200nm to 400nm. However, the light absorbance of these samples is nearly the same in visible light region.

The band gaps of ZnO-PEG and BiOBr/ZnO-PEG samples are calculated according to the Tauc plot equation $\alpha h\nu = A(h\nu - E_g)^{n/2}$ and presented in Figure 5-4 (b), (c), where α, $h\nu$, E_g and A are the optical absorption coefficient, photonic energy, optical band gap and proportionality constant. ZnO-PEG is found a direct-band-gap semiconductor and BiOBr an indirect semiconductor. Both direct and indirect-band-gap behaviour of BiOBr/ZnO-PEG heterojunctions were presented in the Tauc plots (Figure 5-4). Applying the Kubella-Monk relationship, the retrieved band gap of ZnO-PEG and BiOBr from their Tauc plots are 3.0 eV and 2.8eV, respectively. Considering the band gap of BiOBr/ZnO can be direct or indirect, the band gaps were calculated in both conditions and listed in Table 5-1. In either case, the band gaps of BiOBr/ZnO-PEG are apparently larger than ZnO-PEG or BiOBr. Moreover, it is interesting to find that the bandgaps of BiOBr/ZnO-PEG were gradually broadened with increasing loading amount BiOBr. It is noteworthy that the ZnO-PEG shows significant light absorption in the visible light region (400-800 nm) as shown in Figure 5-4 (a). The extended tailed spectra can be ascribed to bulky doping impurity levels or existence of N-doped ZnO-PEG on the surface.
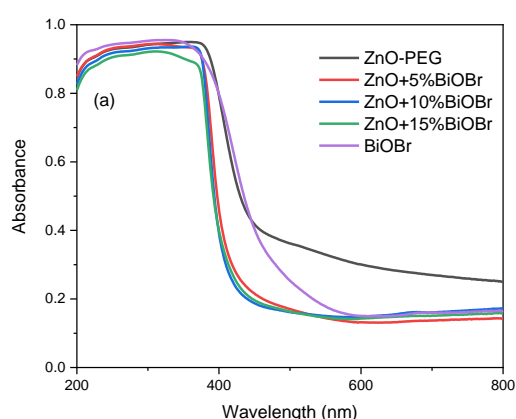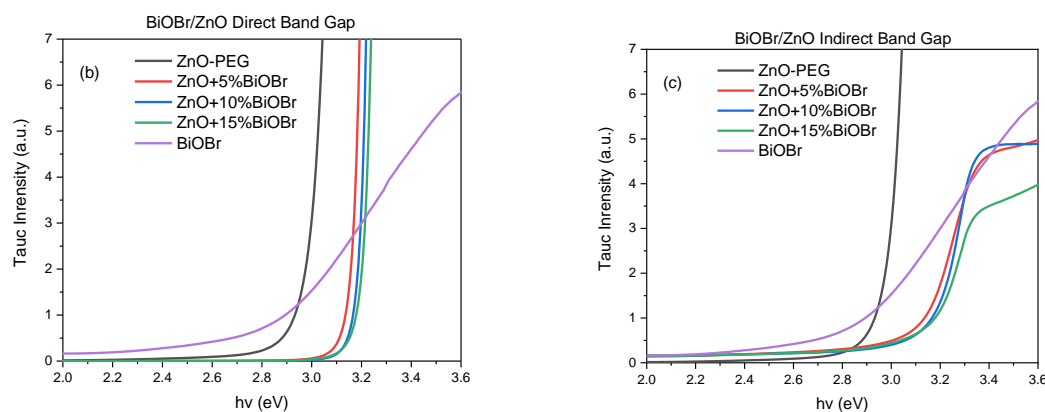
Figure 5-4 (a) UV-Vis absorbance spectra of BiOBr/ZnO-PEG; (b) Tauc plots of BiOBr/ZnO-PEG with direct band gap; (c) Tauc plots of BiOBr/ZnO-PEG with indirect band gap

Table 5-1 Direct and indirect band gap BiOBr/ZnO-PEG in comparison with ZnO-PEG and BiOBr

	Direct band gap (eV)	Indirect band gap (eV)
ZnO-PEG	3.0	
ZnO+5%BiOBr	3.24	3.10
ZnO+10%BiOBr	3.26	3.12
ZnO+15%BiOBr	3.28	3.15
BiOBr		2.8

5.2.3   Electrochemistry characterisation

EIS (Electrochemical Impedance Spectroscopy, including Mott-Schottky and Nyquist plots) of the prepared materials is a powerful measure to determine the electronic properties of the semiconductor photocatalysts and their charge transfer process between the electrolyte and electrode. The EIS Electrochemical impedance spectra were measured in a standard three-electrode system consisting of a platinum counter electrode, a saturated calomel electrode (SCE) reference electrode and the thin film of the as-prepared materials as working electrodes. In the electrochemical characterisations, Mott-Schottky (M-S) scan was firstly recorded to determine the charge density and conduction behaviour in the ZnO-PEG and BiOBr/ZnO-PEG heterojunctions.

As shown in Figure 5-5, the negative slopes in the linear areas of all the M-S plots clearly suggest they are n type semiconductor. Their flat band potentials can be derived from extrapolating the linear area to x-axis, where intercepts on x-axis are the flat band potentials of the materials. According to the equation:

$$\frac{1}{C^2} = \frac{2}{\varepsilon_0 \varepsilon_r e N_D A^2}\left(V - V_{fb} - \frac{k_B T}{e}\right) \tag{1}$$

Where the C is the interface capacitance, A the area of interface, N_D the donor density, V the applied voltage, k_B is Boltzmann's constant, T the absolute temperature and e is the charge of an electron.
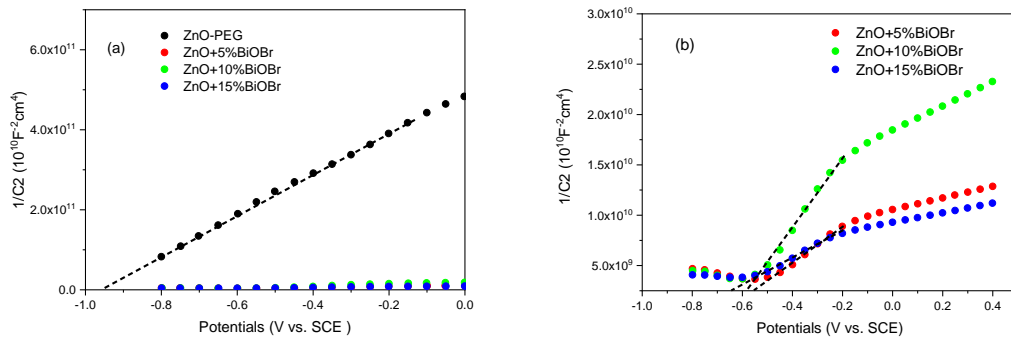
Figure 5-5 Mott-Schottky plots of BiOBr/ZnO heterojunction and ZnO-PEG; (a)Mott-Schottky plot of BiOBr/ZnO in comparison with ZnO-PEG; (b) Enlarged picture of Mott-Schottky plots of BiOBr/ZnO heterojunction

As shown in Figure 5-5, the V_{fb} (flat band) of ZnO-PEG sample locates -0.95V *vs* SCE, whereas the flat band potentials of BiOBr/ZnO-PEG samples are dramatically upshifted as BiOBr loaded. In addition, it is worth noting that the V_{fb} of BiOBr/ZnO-PEG heterojunctions shift to positive potentials when gradually increasing the loading amount of BiOBr. The V_{fb} of ZnO with 5% BiOBr, 10% BiOBr and 15% BiOBr loading are located at -0.55 V, -0.58 V and -0.64 V. Taking the 0.2 eV potential difference between the CBM and flat band for many semiconductors and the pH effects into account, the CBM of the BiOBr/ZnO-PEG are converted to the RHE scale. Accordingly, the CBM of ZnO+5%BiOBr, ZnO+10%BiOBr and ZnO+15%BiOBr locates -0.15 eV, -0.18eV and -0.24 eV respectively. With increasing the loading amount of BiOBr, the CBM of BiOBr/ZnO-PEG are upshifted to higher positions.
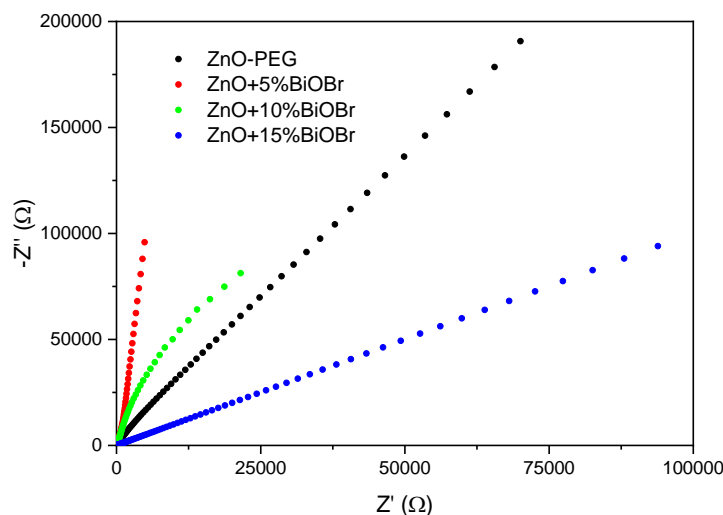
Figure 5-6 Impedance spectra of BiOBr/ZnO-PEG heterojunctions and ZnO-PEG

All the Nyquist plots of the samples were acquired under at OCP (Open Circuit Potential) of corresponding samples scanned from 0.1Hz to 100kHz. As presented in Figure 5-6, all the spectra of relevant samples show straight lines with slight curvature at low frequency (high impedance), indicating there are no faradic reactions occurring at the electrode surface at OCP conditions.
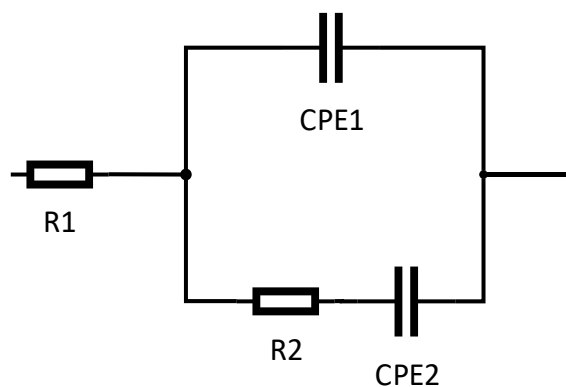
Figure 5-7 Equivalent circuits of BiOBr/ZnO at OCP potentials

The Nyquist data suggest that a capacitor behaviour is dominating, while the tilt reflects a minor contribution of the resistive components. In high frequency region, the Impedance is greatly decreased, and the Nyquist plots bends downwards. The obtained impedance spectra can be interpreted as a three-elements Randel-type electrical equivalent circuit, consisting of CPE (Constant Phase Element), R (Resister) and W (Warburg element). Here, the equivalent circuit model presented in Figure 5-7 was employed to interpret the impedance spectra. The CPE1 in this circuit is the EDL (Electron Double Layer) capacitance and CPE2 it is parallel with charge transfer resistance R2. The Warburg element stands for finite diffusion impedance

in the electrolyte. W contributes both to the real and imaginary parts of impedance. R1 representing the contact resistance between the electrode and substrate ITO glass connect in series with the three-component circuit. The calculated value of each component in the Randles circuits were presented in Table 5-2.

Table 5-2 Calculated value of the components in fitted Randles circuits

Samples	CPE1	CPE2	R1(Ω)	R2(Ω)
ZnO-PEG	621 nF	413nF	33.0	132
ZnO+5%BiOBr	11.1 μF	565aF	32.4	1.05×10^5
ZnO+10%BiOBr	11.9 μF	457nF	36.1	6.10×10^5
ZnO+15%BiOBr	16.1 μF	183nF	33.3	1.10×10^{12}

The capacitance of the CPE obeys the equation:

$$C_\omega = Q\omega^{n-1} \tag{2}$$

Where ω is the angular frequency of the AC voltage, Q is the reciprocal resistance of the CPE. n (ranging from -1 to +1) determine the properties of CPE. When n=1 the CPE is an ideal capacitor; when n=0 CPE becomes ideal resistance; when n=0.5 the CPE act as ideal Warburg diffusion impedance in the electrolyte. According to the results in Table 5-2, the value of R2, due to charge transfer resistance between the electrode and electrolyte, is dramatically increasing with the amount of BiOBr loading on ZnO-PEG [164, 179]. The increasing resistance on the surface will inevitably reduce the charge mobility. Meanwhile, CPE1, the capacitance of the double layer, is reduced as increasing loading amount of BiOBr, which indicate more charge would be accumulated in the double layer [180]. However, comparing with of BiOBr/ZnO-PEG heterojunctions, the ZnO-PEG electrode exhibits the lowest charge transfer resistance and the smallest capacitance of double layer, which means more photo-excited electrons can be delivered to the interface between the electrode surface and electrolyte, where the photocatalytic reaction takes place. As a consequence, more intensive light response current would probably occur on the pure ZnO-PEG electrode under the light.

1.3.4 Photoelectrochemical response
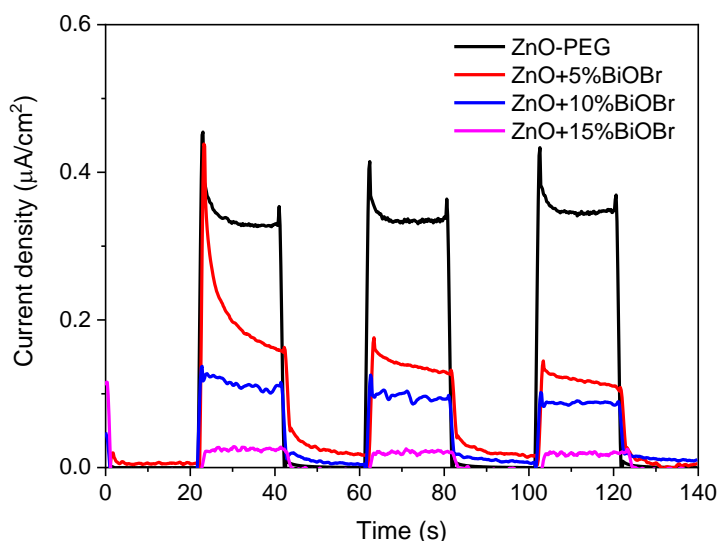
Figure 5-8 Chronoamperometry response of ZnO and BiOBr/ZnO-PEG samples

In order to testify the prediction made in EIS discussion, chronoamperometry was carried out to measure the photo current response from varied BiOBr loading ZnO-PEG. The photo response current can be a direct means to evaluate the photocatalytic performance of BiOBr/ZnO-PEG because it represents the net effective charges across the photoelectrode-electrolyte interface.

In the electrolyte of 0.5M Na_2SO_4, the ZnO-PEG photoelectrode shows the highest photocurrent response followed by 5wt%BiOBr/ZnO, 10wt%BiOBr/ZnO and 15wt%BiOBr/ZnO, respectively. Obviously, the responsive photocurrent on the BiOBr/ZnO-PEG decreases when increasing the BiOBr loading amount. The reduction of the photo current response reveals that the loading of BiOBr deteriorates photocatalytic activity of ZnO-PEG despite that they form BiOBr/ZnO-PEG heterojunctions. Generally, heterojunction exhibits enhanced photovoltaic properties comparing to individual materials. Nonetheless, instead of enhancing the photocatalytic performance of ZnO-PEG, BiOBr/ZnO-PEG shows a poor performance, which may be due to the comprehensive results of their weaker light absorption, lower charge transfer efficiency and smaller surface areas [181].

Considering the drastic transformation in the morphology and structures, these abnormal phenomena can be mainly ascribed to the demolition of the hierarchical structures of original prepared ZnO-PEG. Hierarchically structured nanospheres can enlarge the surface area of ZnO-PEG and increase the light absorption by reducing the reflectance on the surface. In contrast, when BiOBr was loaded onto ZnO-PEG, the hierarchically structured ZnO was gradually covered up by the randomly aligned BiOBr particles. Therefore, more reflectance occurred on the surface and light

absorption is reduced (Figure 5-4). Apart from the influences on light absorption, the hierarchical structures also provide the path for charge transfer and large area for the photocatalytic reaction, which have been confirmed in the Nyquist plots.

In summary, it is of importance to create large surface area on the photocatalyst because all the photocatalytic reactions take place on the surface. Large surface area not only provide place for the reactions but also sufficient photogenerated charge carriers for photocatalytic reactions.

5.3   Conclusion

Hierarchical ZnO-PEG was prepared via hydrothermal synthesis, which exhibit a hierarchically assembled structure. After loading with various amount of BiOBr, the photocurrent responses decrease, which can be ascribed to the cover of the BiOBr over the ZnO. The photocatalytic performance of the BiOBr/ZnO-PEG was evaluated by photoelectrochemistry method, which indicated the performance was also greatly influenced by the increasing amount of BiOBr. Here, the research further confirms that the hierarchical structure is of greater importance than the light absorption in the photocatalytic reactions for the BiOBr/ZnO-PEG heterojunctions and their individual constituent semiconductors.

Chapter 6 **Photo-electrochemistry Performance of Electrode-deposited BiOBr$_x$I$_{1-x}$/CuSCN Heterojunction films**

6.1 Introduction

Solar energy conversion with adequate efficiency is the most challenging aspect in the traditional photovoltaics materials. In the traditional heterojunction photocatalysts are composed of the holes transport layer (HTL) and electrons transport layer (ETL) [182-185]. And in the conventional bulk solar cells, the heterojunctions or PN junctions in the materials are not only generate photo-excited electricity current but also at same time assisting the charge separation [164]. Using heterogeneous deposition on highly structured semiconductor substrates to form heterojunctions has been an attractive component in many electrical, photoelectrical, and catalytic applications where an enlargement of the interface area is generally desirable [46, 186]. This is especially valuable for nanocrystal photovoltaic cells and photo-catalysts, because of the enhancement of the light trapping for the photo-generated carriers and the separation of the excited charges. The previous work from Zhao's group had succeeded in using hierarchical TiO$_2$ nano-tubes and vertical aligned ZnO nano-wires to supply good charge transfer efficiency [187]. However, in order to receive high reaction activities in the performance, p-type semiconductors can be also introduced to form heterojunctions with some n-type semiconductors, such as TiO$_2$, ZnO and BiOBr [33, 188, 189]. As p-type semiconductor, copper thiocyanate (CuSCN) is thought to be one of most promising candidates due to its transparency in the visible light spectrum, reasonable holes conductivity and relative good chemical stability [49]. More importantly, CuSCN works excellent in the solution with appropriate solvent and concentration under room temperature, therefore making CuSCN possible for low-cost, large scale application on flexible substrate applications [45, 46].
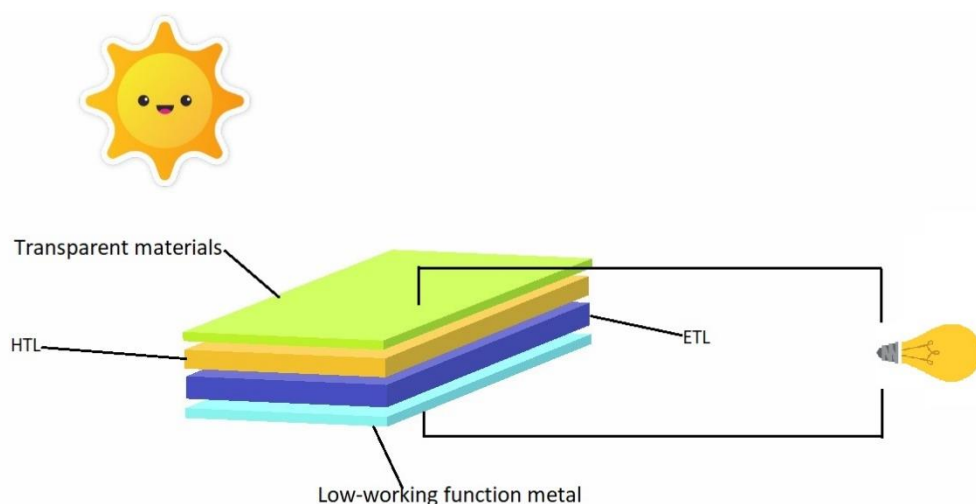
Figure 6-1 Solar cell structure diagram

There are multiple techniques for synthesis CuSCN. Whereas considering its thermal stability, CuSCN film making could be crucial in the device making. In the past papers, CuSCN films were mostly reported to be obtained from CBD, SILAR and electronic deposition process, in which the electronic deposition was recognised as a feasible and reliable process for coating complex structure on the ITO/FTO glass [116, 190]. Up to now, most electronic deposition related synthesis CuSCN were carried out in organic solution because of the instability of Cu (I) cations and SCN anions in aqueous solution. At the same time, the process of the deposition was hampered by poor conductivity of organic solvent [179, 191]. However, using EDTA-chelated copper electrolyte can be solution to the problem. EDTA here will not only protect Cu (I) cations but also act as templates to assist assembling of hierarchical structures on ITO glass. Although CuSCN exhibits good performance as photocatalyts in the reactions, it has a critical limitation, in that its photo-catalytic performance is restricted by its wide band-gap energy (E_g = 3.4~3.9 eV), which make it only ultraviolet response. In order to further increase the light harvesting efficiency, combination with second semiconductor to form heterojunction would open a wide area for the application not only in photocatalyst but also in the photovoltaics and sensor. The hierarchically assembled CuSCN will be a good support for a p-n junction or heterojunction for photovoltaics application. Bismuth oxyhalide (BiOX), with a relatively smaller band gap, will undoubtedly increase the light harvesting during the photocatalytic process[188]. Also, BiOBr, as an active n-type semiconductor, possesses a layered structure, which endows BiOBr with outstanding performance in charge separation and transition [41, 95]. Once BiOBr is coupled with CuSCN forming a heterojunction, the overall optical band gap will be therefore reduced，which correspond to a increase in solar energy absorption. In addition, all BiOX compounds share a similar

structure, which make it possible to produce a solid solution of $BiOX_{1-x}Y_x$ (X, Y=F, Cl, Br and I) by introducing impurity Y into BiOX. $BiOX_{1-x}Y_x$ hybrid system provides another possibility to further modify the photo-electric properties and corresponding photocatalytic performance of the BiOX/CuSCN heterojunction. Iodine with the largest radius in the halogen and abundant electrons in the valence band will probably uplifting the VBM of BiOBr by importing impurity level between the conduction band and valence band, when Iodine is incorporated into the structure [135, 192].
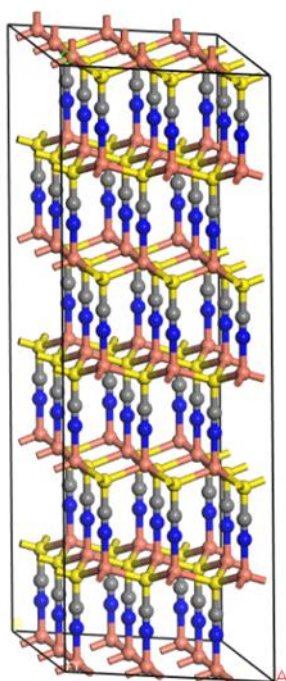
Figure 6-2 Crystal structure of CuSCN [3, 115].

Here a hierarchically aligned $BiOBr_xI_{1-x}$/CuSCN heterojunction were prepared by dip-coating and electrode deposition process. And its photovoltaics properties were discussed in the followings.

6.2   Experimental sections

6.2.1   Materials synthesis

The electrode deposition of CuSCN was carried out in the 250ml beaker with 3 electrodes-systems. Prior to the electrode deposition, the ITO substrates were ultrasonically cleaned in the sequence of acetone, ethanol and water. A platinum rod was used as counter electrode; SCE electrode was set as reference electrode. A solution of 50ml containing 0.025M $CuSO_4$, 0.025M KSCN and 0.025M EDTA was

used as electroplating bath. The potentials bias of the working electrode was set as -0.3V under the room temperature. All the potentials reported in this work were vs. SCE referenced scale. After the deposition process all the samples were cleaned by deionised water and dried in the furnace of 60℃ to remove the templates reagent on the surface of the films.

6.2.2   BiOBr$_x$I$_{1-x}$/CuSCN Dip-coating

In order to investigate the influence of the heterojunction on the photocatalysts, varied layered BiOBr$_x$I$_{1-x}$ was coated onto CuSCN through dip-coating process. Three kinds of solutions: 10mM Bi(NO$_3$)$_3$, 10mM KBr and 10mM KBr/I (K and I in different ratio) were prepared as coating solution. The entire process is illustrated as below in **Error! Reference source not found.**. The films of CuSCN were dipped in the s equence of Bi(NO$_3$)$_3$, H$_2$O, KBr or KBr/I and H$_2$O. H$_2$O dipping here was used to prevent the contamination of coating solution.
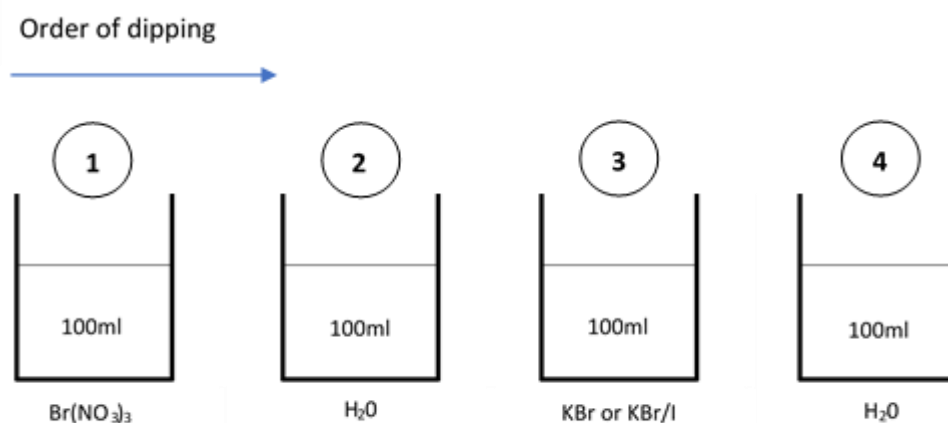
Figure 6-3 Schematic showing the order of dipping used in the dip coating experiments

6.2.3   Characterisation

All the x-ray diffraction data were collected form the Rigaku Smart Lab using Cu-Kα1 radiation (λ=0.154056 nm) at a scan rate of 0.05° 2θ^{-1}s and were used to determine the phase of the structures of the samples. The UV-vis diffuse reflectance spectra were obtained on Perkin Elmer Lambda 950 UV/Vis/NIR spectrophotometer equipped with a 150mm snap-in integrating sphere for capturing diffuse and specular reflectance. BaSO$_4$ was used as a reflectance standard in the UV-visible diffuse reflectance experiment. Scanning electron microscopy (SEM) was performed

to investigate the surface morphology using JEOL JSM-6301F Field Emission SEM at an accelerating voltage of 10kV.

The photo-electro-chemistry tests were conducted by using an AutoLab electrochemical workstation in a three-electrode cell with a Pt rod and a saturated calomel electrode respectively as counter electrode and reference electrode. Prior to measurement, the working electrodes were immersed in Na_2SO_4 solution (0.1 M) for 30 s. A 500 W Xenon arc lamp was utilized as the light-source. Electrochemical Impedance Spectroscopy (EIS) was used to evaluate the properties of the different photocatalysts under AC polarization. EIS experiments were conducted in a 0.5M sodium sulphate (Na_2SO_4) solution and in a frequency range of 100 kHz to 100 mHz for an amplitude of 10 mV in DC potential. In addition, Mott-Schottky experiments were conducted to evaluate the capacitance behaviour under DC potential polarization. The potential range was -0.8 to +1.5V (vs. SCE) with potential steps of 50 mV at a constant frequency of 3000 Hz.

6.3 Results and Discussion

6.3.1 Microstructure, morphology and composition of CuSCN thin films

The XRD patterns of CuSCN shown in the **Error! Reference source not found.** (a) e videnced CuSCN was successfully obtained from electrode deposition. Although some peaks of ITO glass showed on the XRD pattern of CuSCN films, highly crystalline CuSCN can be clearly identified in the diffraction patterns below. The XRD patterns of CuSCN deposited under different ratio of Cu^{2+}/SCN^- are compared in Figure 6-4(a). During all the electrode deposition process, the concentration of Cu^{2+} and EDTA were kept same at 0.12M, while the concentration of SCN^- varied among 0.06M, 0.12M and 0.24M. All the major peaks are indexed, and other peaks can be identified from ITO substrate. The orientation of the CuSCN films is along with the direction of (003) perpendicular to the substrate. When SCN^- was kept at a low concentration, numbers of minor peaks from the impurity phase can be observed in the diffraction patterns; however, with increasing the concentration of SCN^- in the deposition the impurity phases were gradually reduced. The pattern of the CuSCN films which Cu: SCN=1:2 shows best match among three samples. All the peaks are in good match with hexagonal crystal lattice of β-CuSCN (ICSD No. 01-075-2315). The Figure 6-4(b) shows the XRD patterns of $BiOBr_xI_{1-x}$/CuSCN heterojunction with various coating layers of $BiOBr_xI_{1-x}$. Comparing the diffraction patterns of pure CuSCN film and ITO substrate, the peaks of $BiOBr_xI_{1-x}$ can be

identified on the patterns of $BiOBr_xI_{1-x}$/CuSCN film. Although some peaks disappeared after $BiOBr_xI_{1-x}$ was coated onto CuSCN, the characteristic peak (003) of CuSCN remains unchanged in the $BiOBr_xI_{1-x}$/CuSCN patterns. More importantly, with increasing layers of $BiOBr_xI_{1-x}$ coated onto CuSCN, no obvious peak shift or change is observed in the Figure 6-4(b).
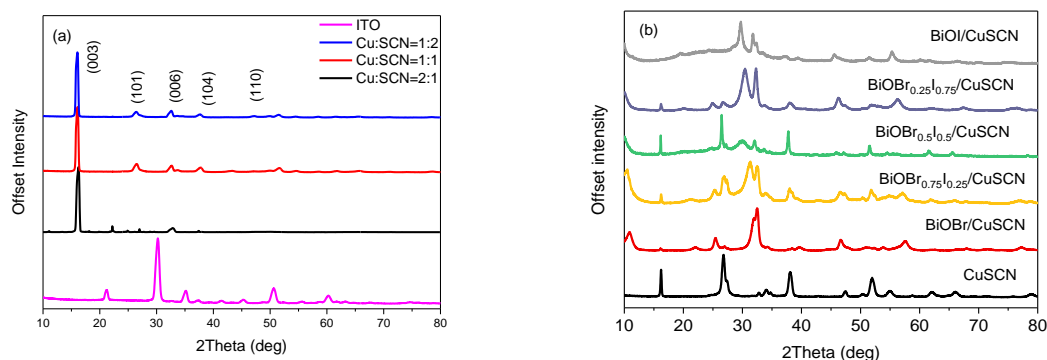
Figure 6-4 XRD patterns of (a) CuSCN films synthesed in different Cu^{2+}/SCN^- ratios;(b) XRD patterns of CuSCN films coated with various layers of BiOBr.

Morphologies of the as-prepared CuSCN and $BiOBr_xI_{1-x}$/CuSCN film are revealed by SEM shown in Figure 6-5. Considering the similar crystal structure of BiOX, multi-layer coated BiOBr/CuSCN was set as an example for morphologies transition discussion. Figure 6-5 are the SEM image of CuSCN prepared in different Cu/SCN concentrations. Figure 6-5 (a) and (b) are the top view of the films prepared in the lower concentration of SCN^-, which display a close-packed vertical aligned nano arrays with diameter of 150nm. The size of nanorods in the (a) and (b) are uniformly distributed. When the concentration of SCN^- was kept same as Cu^{2+}, the deposited CuSCN still displays vertical nanorods shown as in (c) and (d). But the diameter of the nanorods is increased to 220nm. Further increasing the concentration of SCN^-, the morphologies of the CuSCN are nanorods with a diameter increased to 400nm. According to the images delivered by the SEM, all the morphologies of deposited CuSCN exhibit vertically aligned nanorods, and the diameter of nanorods increased with the concentration of SCN^- in the solution. Considering the XRD patterns in Figure 6-5, high ratio of SCN^- are not only contribute to the good crystallinity but also increase the dimension of the deposited CuSCN nanorods on ITO substrate as well. Moreover, some research pointed out that as an intrinsic p-type semiconductor, high concentration of SCN^- in CuSCN creates a stoichiometric deficiency of Cu in the crystal, and hole-transporting character is close related with Cu vacancies in the CuSCN. By introducing Cu vacancies, acceptor impurity level generated close to VBM (valence band maximum) will lower the band gap of CuSCN,

and thus increase the solar energy conversion efficiency in the materials. In order to optimize the dip-coating layers of $BiOBr_xI_{1-x}$, various layers of $BiOBr_xI_{1-x}$ were coated onto CuSCN films. As shown in Figure 6-7, the top view of $BiOBr_xI_{1-x}$-coated CuSCN was listed in the sequence of number of $BiOBr_xI_{1-x}$ coating layers. The pure CuSCN film was presented in the Figure 6-7 (a). The following pictures (b), (c) and (d) display the morphology of CuSCN films with 5 layers of BiOBr, 10 layers of BiOBr and 15 layers of BiOBr respectively. Increasing the coating layers of BiOBr, the nanorods on the surface of CuSCN films were gradually covered by flake-structured coating layers, which can be observed in Figure 6-7. With increasing number of layers of BiOBr on CuSCN, the hierarchical surface was gradually covered by the random deposited particles. On the other hand, the colour appearance of $BiOBr_xI_{1-x}$/CuSCN was also changed by varying I ratios in fixed coatings layers of $BiOBr_xI_{1-x}$. A clear colour transition of films as shown in Figure 6-6 reflects I dopants influence on light absorbance of $BiOBr_xI_{1-x}$/CuSCN under the visible light range.
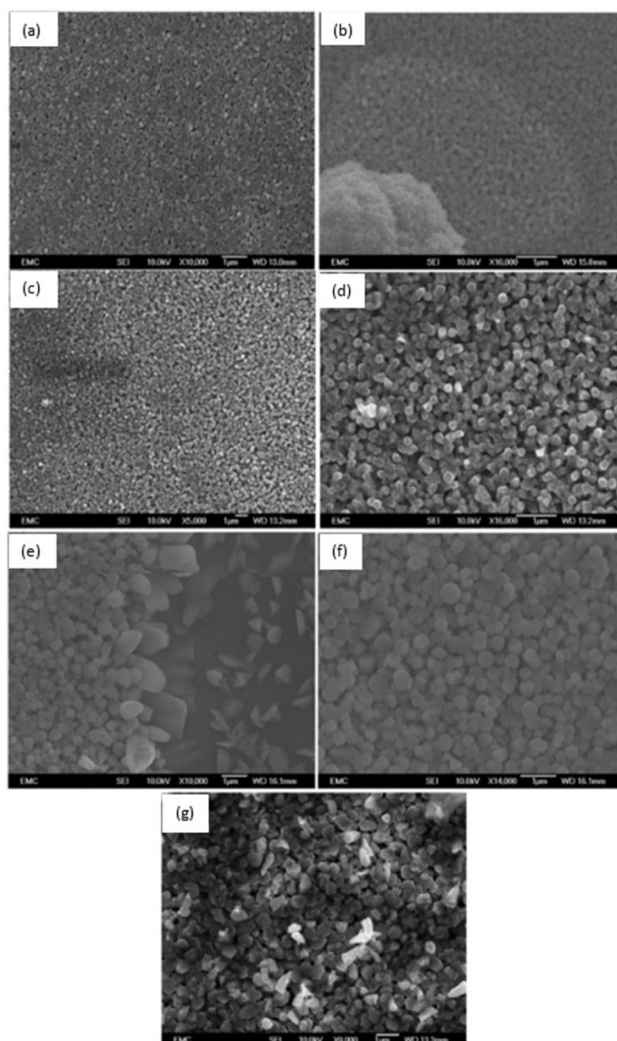
Figure 6-5 SEM images of electrochemical deposited CuSCN on ITO: (a), (b) CuSCN films prepared in Cu/SCN=2:1; (c), (d) CuSCN films prepared in Cu/SCN=1:1; (e), (f) CuSCN films prepared in Cu/SCN=1:2.
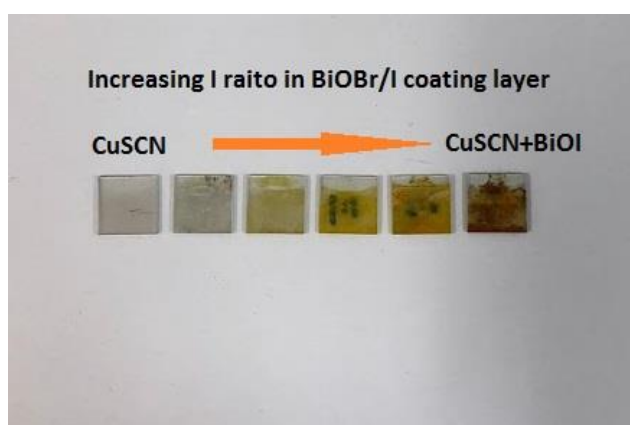
Figure 6-6 Colour change of coated CuSCN films with varied Br/I ratios
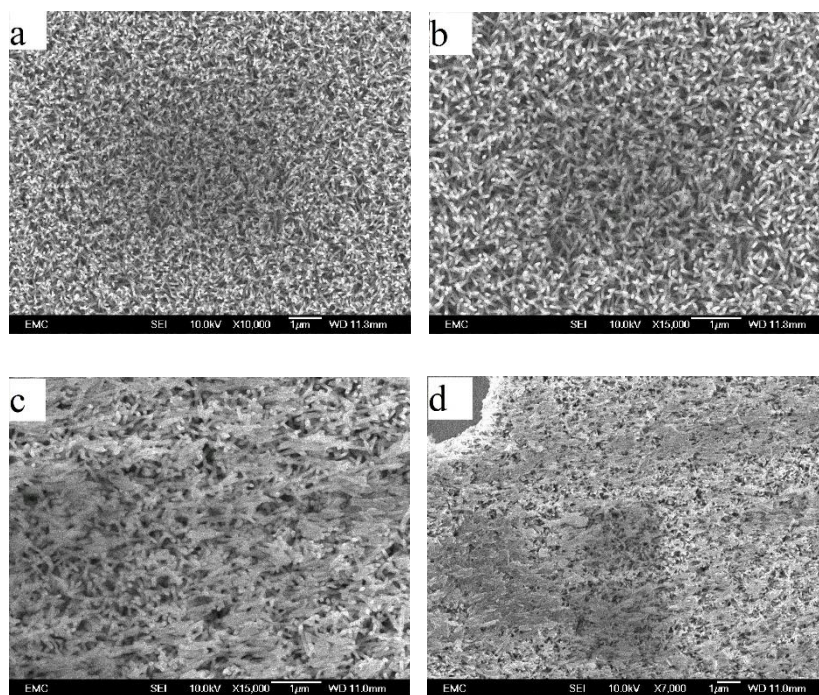
Figure 6-7 SEM images of multi-layer BiOBr coated CuSCN films: (a) Image of CuSCN film for reference; (b) CuSCN coupled with 5 layers of BiOBr; (c) CuSCN coupled with 10 layers of BiOBr; (d) CuSCN coupled with 15 layers of BiOBr.

6.3.2   Optical and electrical properties of CuSCN films

The optical properties of the photocatalyst are crucial factor to determine the light absorption during the photocatalytic process. In this work, the light absorption of $BiOBr_xI_{1-x}$ coated CuSCN films was studies by UV-Vis/DRS shown in Figure 6-8. The reflectance of the $BiOBr_xI_{1-x}$/CuSCN films was converted from absorbance and transmittance spectra. Pristine CuSCN shows an ultraviolet absorption, while the $BiOBr_xI_{1-x}$ dip-coated samples exhibited strong visible light absorbance. Comparing with $BiOBr_xI_{1-x}$ coated films, the light absorbance edge of CuSCN tailed at 350nm, while $BiOBr_xI_{1-x}$/CuSCN heterojunctions had extended their absorbance up to 600nm. It is also worth noting that the light absorption of $BiOBr_xI_{1-x}$/CuSCN expanded with increasing I ratios in $BiOBr_xI_{1-x}$ coating layers, which is good agreement with the results shown in Figure 6-6.

Tauc plots presented in Figure 6-8 (b) shows the band gap of various $BiOBr_{1-a}I_a$ loaded CuSCN films. The corresponding band gap E_g of CuSCN is locates at 3.6 eV and E_g of the $BiOBr_xI_{1-x}$/CuSCN films are approximately in the region of 2.82-1.86 eV dependent on the composition of $BiOBr_{1-x}I_x$ and loading layers, smaller than that of CuSCN. The band gap of CuSCN shows a good agreement with the previous

research results. Because BiOBr process a much lower optical band gap of 2.6-2.8 eV, the band gap and light absorption of the heterojunction $BiOBr_xI_{1-x}/CuSCN$ was eventually narrowed down. According to the calculated band gaps of $BiOBr_xI_{1-x}/CuSCN$ presented in Table 6-1, BiOI/CuSCN possessed the smallest band gap as 1.86eV, which followed by $BiOBr_{0.25}I_{0.75}/CuSCN()$, $BiOBr_{0.5}I_{0.5}/CuSCN$, $BiOBr_{0.75}I_{0.25}/CuSCN$ and BiOBr/CuSCN. Apparently, the band gaps of $BiOBr_xI_{1-x}/CuSCN$ were gradually decreased with increasing I ratio in $BiOBr_xI_{1-x}$ coating layers.
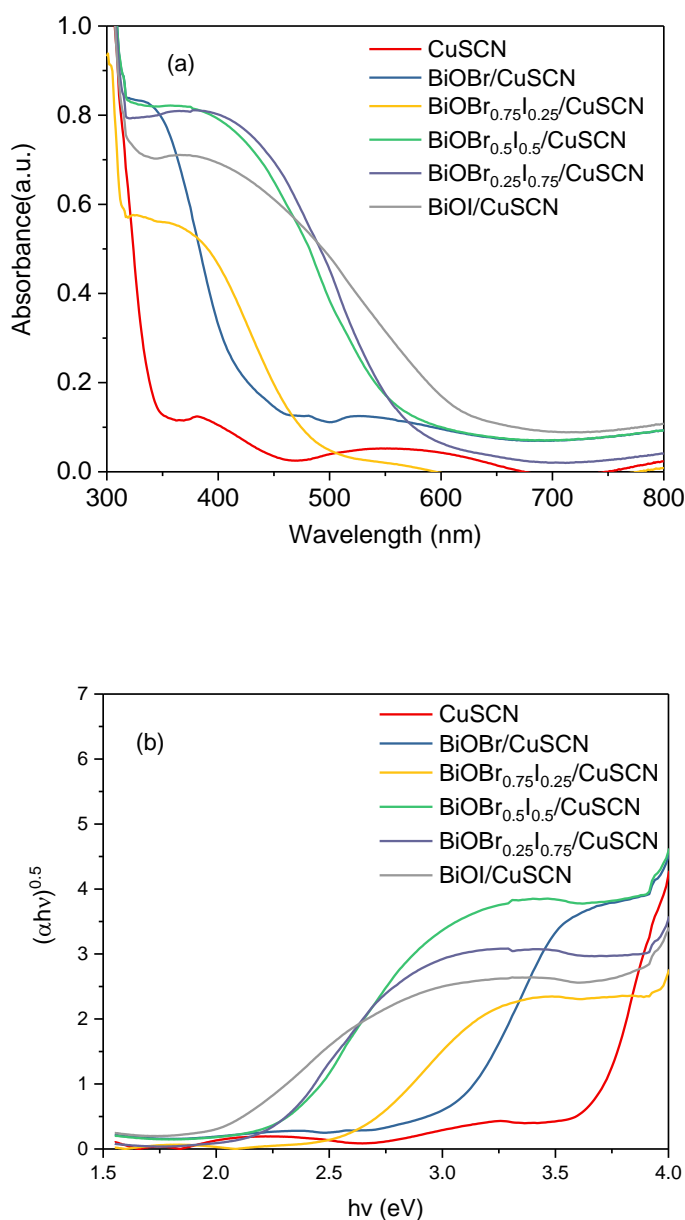
Figure 6-8 UV-Vis/DRS of $BiOBr_xI_{1-x}/CuSCN$ films with vaious Br/I ratios

6.3.3   PEC and electrochemical properties of CuSCN thin films

In order to have a good understanding of the band structure of the CuSCN and $BiOBr_x/I_{1-x}$/CuSCN heterojunctions, the EIS (electrochemical impedance spectroscopy) scan was implemented in the experiments. The Mott-Schottky plots of the materials were obtained from the impedance potential scanning at the frequency of 3000Hz. The $BiOBr_x/I_{1-x}$-coated CuSCN films of different Br/I ratios and layers were both presented in Figure 6-10 (a) and (b) separately. In Figure 6-10 (a), the capacity measurements result from different ratios of Br/I are plotted and compared. In addition, all the sample listed in Figure 6-10 (a) are deposited with 15 layers of $BiOBr_x/I_{1-x}$. According to the equation:

$$\frac{1}{C^2} = \frac{2}{A^2 \varepsilon_0 \varepsilon_r e N_D} \left(V - V_{fb} - \frac{k_B T}{e} \right) \tag{1}$$

$$E_{band\ edge} = \mu \pm q V_{fb} \tag{2}$$

the flat band potentials of these materials can be determined by extrapolation of Mott-Schottky plots, as shown in Figure 6-10 (a) from the depletion layer region of voltage to the intercept. Here μ is derived from solid state physics measurements of the energy difference between bulk conduction band edge and Fermi energy. As μ is generally only order of 0.2 eV from the conduction band or valence band, the measurement of V_{fb} provides a good estimate of the band edge location. The negative slope of the Mott-Schottky plots in Figure 6-10 has confirmed that all the $BiOBr_xI_{1-x}$/CuSCN films exhibit p-type semiconductor behaviour in the electrolyte. In a typical p-type semiconductor, the flat band usually locates close to the valence band maximum. Therefore, the flat band potentials as well as the valence band edges can be calculated and listed in Table 6-1.

Table 6-1 Calculated flat band and VBM of 1-layer coating $BiOBr_xI_{1-x}$/CuSCN films

Sample	V_{fb} vs. NHE (eV)	VBM vs. NHE (eV)	Band gap (eV)
BiOBr/CuSCN	0.90	1.20	2.82
$BiOBr_{0.75}I_{0.25}$/CuSCN	0.84	1.14	2.50
$BiOBr_{0.5}I_{0.5}$/CuSCN	0.82	1.12	2.11
$BiOBr_{0.25}I_{0.75}$/CuSCN	0.85	1.15	2.07
BiOI/CuSCN	0.86	1.16	1.86
CuSCN	0.83	1.13	3.62

According to Table 6-1, varying the ratio between Br and I in the coating layers, the flat band potentials of $BiOBr_xI_{1-x}$/CuSCN is slight increased. As a result, the overall

valence band of the BiOBr$_x$I$_{1-x}$/CuSCN heterojunction shows a lower potential comparing with the valence band in pure CuSCN. The shifts of the valence band can be ascribed to the band alignment in heterojunction. When two types of semiconductors were in contact at the interface, not only the structures of the materials are bonded together, but also the energy bands. When BiOBr$_x$I$_{1-x}$ was coated onto CuSCN, a typical p-n junction was formed on the interface of two materials. As shown in Figure 6-9, BiOBr$_x$I$_{1-x}$/CuSCN heterojunction is an effective architecture for the highly efficient charge collection and separation. Due to the built-in electric filed, the photo-induced electrons and holes were forced to travel in opposite directions. Thus, more charge carriers can be transferred to surface for further photocatalytic reactions. Comparing flat band potentials of the BiOBr$_x$I$_{1-x}$/CuSCN heterojunctions in Table 6-1, BiOBr$_{0.5}$I$_{0.5}$/CuSCN possessed highest flat band potential among all BiOBr$_x$I$_{1-x}$/CuSCN films, which indicating superior oxidation performance in the degradations of chemicals. In addition, by increasing coating layers of BiOBr$_{0.5}$I$_{0.5}$, the flat band potentials of BiOBr$_{0.5}$I$_{0.5}$/CuSCN were gradually reduced as shown in Figure 6-10 (b), because the depletion layer on the electrode interface is decreased as more active electrons was introduced from BiOBr$_{0.5}$I$_{0.5}$ donor layers.
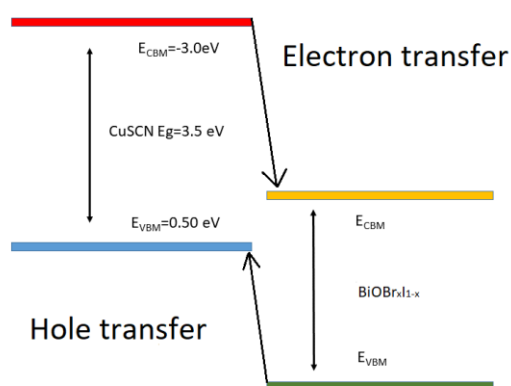
Figure 6-9 Band structure diagram of BiOBr$_x$I$_{1-x}$/CuSCN heterojunctions
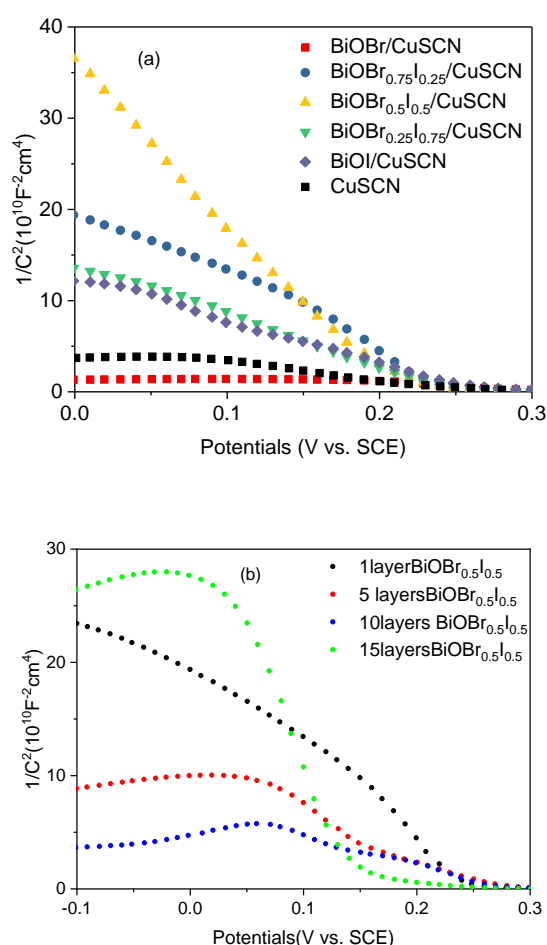
Figure 6-10 Mott-Schottky plot of BiOBr$_x$I$_{1-x}$/CuSCN films: (a) Mott-Schottky plots of BiOBr$_x$I$_{1-x}$/CuSCN films with various Br/I ratios; (b) Mott-Schottky plots of BiOBr$_{0.5}$I$_{0.5}$/CuSCN films with various BiOBr$_{0.5}$I$_{0.5}$ coating layers

The impedance scan was also employed to investigate the charge transport process of photocatalytic materials. The scanning frequency was set from 0.1Hz-100kHz which is capable to describe the wide-range internal resistance of electrochemical process. The impedance at low frequency (0.1-1Hz) corresponds to the Nernst diffusion in the electrolyte [7, 164]. The impedance at high frequency (1-100K) is related with the capacitance and charge transfer resistance at the electrolyte interface. Figure 6-11(a) shows the impedance spectra of pure CuSCN and varied ratio of BiOBr$_x$I$_{1-x}$/CuSCN films. In the experiments, the BiOBr$_x$I$_{1-x}$ coating layers degraded with time, resulting in more complex behaviour. The impedance spectra of the BiOBr$_x$I$_{1-x}$/CuSCN were fitted with equivalent circuits presented in Figure 6-12. As shown in Figure 6-12, the CPE1 stands for capacitance of double layer between the CuSCN and electrolyte. CPE2 stands for the capacitance between the coating layer of BiOBr and electrolyte. R1 represent the serious connected resistance of

electrode, and R3 represent the kinetically controlled charge-transfer resistance of interface between the electrode and electrolyte. The W (Warburg impedance) in the circuit stands for resistance of diffuse layer in the electrolyte [15, 30, 193].According to the equivalent circuit, the value of each component of the circuit was obtained by fitting the impedance spectra. The fitted results are shown in the Table 6-2. According to the simulation results listed in Table 6-2, the series connected resistance R1remain almost same which indicates that electrodes was setup in a similar condition. Also, it is worth noting that the capacitance of $BiOBr_xI_{1-x}$/CuSCN double layer is stabilized at $10\mu F$, showing a limited capacitance behaviour. In the aspect of charge transfer resistance R3, the $BiOBr_xI_{1-x}$/CuSCN with 1:1 Br/I ratio shows the lowest charge-transfer resistance among all the samples, indicating active faradic process occurring on the surface of $BiOBr_{0.5}I_{0.5}$/CuSCN during the photocatalytic reactions. At the same time, the Nyquist plots shown in Figure 6-11 Nyquist plots of the $BiOBr_xI_{1-x}$/CuSCN films: (a) impedance spectra of $BiOBr_xI_{1-x}$/CuSCN with different Br/I ratios; (b) impedance spectra of $BiOBr_{0.5}I_{0.5}$/CuSCN with various $BiOBr_{0.5}I_{0.5}$ coating layers(b), the heterojunction film of 15 layers coating shows smallest radius which correspond to the lowest charge-transfer resistance comparing with the rest of samples.
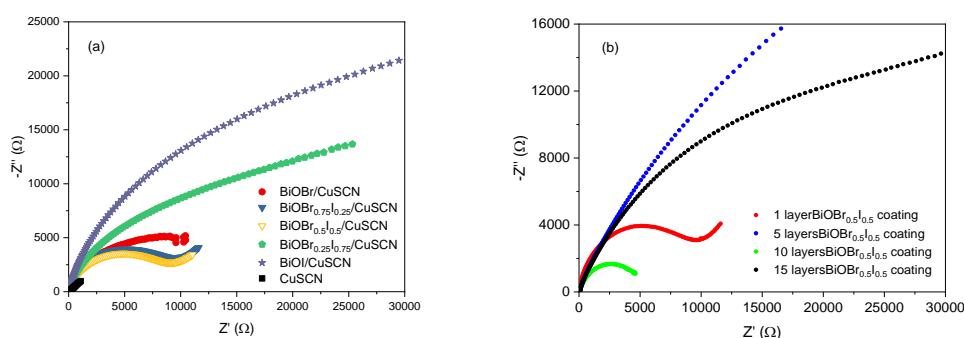
Figure 6-11 Nyquist plots of the $BiOBr_xI_{1-x}$/CuSCN films: (a) impedance spectra of $BiOBr_xI_{1-x}$/CuSCN with different Br/I ratios; (b) impedance spectra of $BiOBr_{0.5}I_{0.5}$/CuSCN with various $BiOBr_{0.5}I_{0.5}$ coating layers
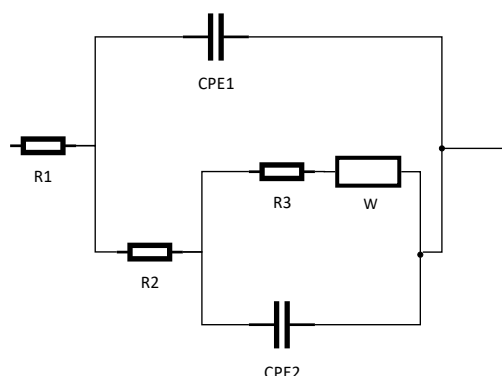
Figure 6-12 Randles circuits used to fit the impedance spectra

Table 6-2 Parameters obtained by fitting the impedance spectra

Samples	R1(Ω)	R2(Ω)	R3(Ω)	CPE1(μF)	CPE2(μF)	W(μMho)
Pure CuSCN	24.1	27.0		7.182		73
Br: I=1: 0	32.0	6.97k	2.55k	19.5	11.3	107
Br: I=3: 1	30.7	6.77k	2.18k	6.11	7.0	264
Br: I=1: 1	28.8	7.86k	684	10.8	9.5	334
Br: I=1: 3	30.9	11.4K	39.9K	10.4	8.9	1000
Br: I=0: 1	36.2	35.2k	1.10T	10.3	8.7	1000
Br: I=1: 1 (5 cycles)	46.6	774	8.15k	18.0	13.1	30.0
Br: I=1: 1 (10 cycles)	35.2	6.52k	1.37k	41.3	28.8	80.0
Br: I=1: 1 (15 cycles)	36.1	4.36k	1.10T	7.14	20.1	90.1

The photocatalytic performances of the $BiOBr_xI_{1-x}$/CuSCN films were measured by chronoamperometry test under the visible light. All the measurement was carried out under the open circuit potential (OCP) and 20 seconds quite time was given to each test to establish the equilibrium in the electrolyte. As shown in Figure 6-13, when lights on, a negative current was generated in all the samples, which indicating all the samples display a p-type semiconductor behaviour. Comparing the light response from different samples, the $BiOBr_{0.5}I_{0.5}$/CuSCN exhibits the highest light response among all the samples represented in Figure 6-13. On the other hand, the $BiOBr_xI_{1-x}$/CuSCN with various coating layers was also measured in Figure 6-13. The $BiOBr_{0.5}I_{0.5}$/CuSCN with 15 coating layers exhibits most active light response, which can be ascribed to the enhancement of light absorbance and charge transfer efficiency in the heterojunctions.
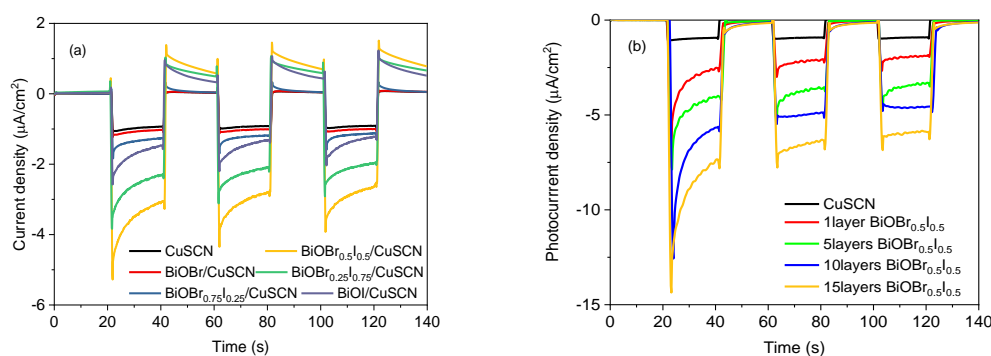
Figure 6-13 Chronoamperometry plots of the $BiOBr_xI_{1-x}/CuSCN$: (a) photocurrent response of $BiOBr_xI_{1-x}/CuSCN$ films in various Br/I ratios; (b) photocurrent response of CuSCN films coated with various layers of $BiOBr_{0.5}I_{0.5}$

6.4   Conclusion

In order to investigate influence of the heterojunction on the photocatalytic performance of CuSCN, $BiOBr_xI_{1-x}$ were coupled with CuSCN via dip-coating process. Various ratios of Br/I and layers of coating were compared in the experiment. Coupling CuSCN with $BiOBr_xI_{1-x}$ not only increased the light absorption of CuSCN films, but also supressed the charge recombination by built-in electric field of $BiOBr_xI_{1-x}/CuSCN$ heterojunctions. As a result, the photocurrent response of the heterojunction was increased compared with pure CuSCN films. Moreover, by controlling the Br/I ratios in the coating layer, the strongest photocurrent was observed at Br:I=1:1. At the same time, the electron-transfer resistance of the interface was increased after coating, which implies that the photo-excited electrons would be reduced as more energy are required to overcome the resistance on the surface of the films. The impedance spectra and UV-vis spectra evidenced the result from light response current in the chronoamperometry test.

Chapter 7 Sulphur Doped Hierarchical ZnO and Application in the Antibiotic

7.1 Introduction

ZnO is recognised as a promising solution to address current environment and energy issues. It is an intrinsic n-type semiconductor with favourable thermal stability and photovoltaic properties [102]. Additionally, the preparation cost of ZnO is up to 75% lower than that of TiO_2 and Al_2O_3 [194]. Therefore, ZnO has received increasing attention on its applications for photocatalysis and energy conversions [137]. However, due to a wide band gap of ZnO (3.37 eV), only ultraviolet light can be utilised during the photocatalytic process. Over the past decades, a variety of attempts has been made to tuning the band gap of ZnO so that more solar energy can be employed in the reactions [32, 55, 173]. Generally, doping with non-metal or transition metal, coupling with other small-bandgap semiconductors or metals, and creating structural vacancies have been proved as good approaches towards energy bands engineering [17, 106]. The band gap modification of ZnO by impurity incorporation is currently an important methodology in the scientific research and industry production. Doping selective elements into the ZnO offers an effective tool not only for energy band engineering, but also dramatic changes in its optical and electrical properties [195].

Inspired by the success in the enhanced visible-light response of non-metal-doped TiO_2 [196], non-metal-doped ZnO photo-catalysts have been recently attempted because the non-metal (S, N or C) dopants can extend visible light absorption significantly and well suppress photo generated charge recombination at suitable doping level [87, 106, 197, 198].

Nitrogen and sulphur doped ZnO are emerging visible light response photo-catalysts with extraordinary performance in the water-splitting, environment cleaning, photo-electrochemical cells [199]. Although N-doped ZnO and S-doped ZnO have been already prepared in the previous studies, the preparation process was complicated and expensive involving several precursors and procedures [106, 112, 114, 139]. Here we are going to present a facile pyrolysis approach to prepare sulphur doped ZnO.

Here, simple one-step combustion synthesis of S-doped ZnO is presented in this chapter. A hierarchically assembled S-doped ZnO was obtained. The structure of

the ZnO was investigated using SEM and XRD. In addition, the photocatalytic performance and antibiotic properties of the ZnO was also examined in the following discussion.

7.2 Experimental section

7.2.1 Materials synthesis

All the chemicals were reagent-grade and were purchased from Sigma-Aldrich Company without any further purification. Deionised water was used in all the experiments. In order to explore the suitable doping level of sulphur and the correlation between the dopant level and photo-catalytic performance, the experiment was set in 5 groups. In the experiment, 4.065 g $Zn(CH_3COO)_2$ was dissolved in the mixture of the 15 ml deionised water, 5ml ethanol and 1 ml acetic acid glacial (HAc) and under rigorous stirring to obtain a clear solution. Then different amount of L-Methionine was added into the beakers. The resulting mixed solutions were then transferred to the oven for drying under 125℃ and heated overnight to vapour solvents. The gel was grounded to powder before calcination in the muffle oven at 450℃ for 3hours at the speed of 2℃/min. In comparison, a pristine ZnO was prepared in the same procedure without adding any Methionine. The detailed recipe is placed below:

Table 7-1 Recipe of S-doped ZnO preparations

	Zn(Ac)₂· 2H₂O (mol)	L-Methionine (mol)	Ethanol+H₂O+HAc
S1	0.02	0	15ml H₂O+5ml Ethanol+1ml Acetic acid
S2	0.02	0.01	
S3	0.02	0.02	
S4	0.02	0.03	
S5	0.02	0.04	

7.2.2 Characterisation

X-Ray diffraction (XRD) patterns were obtained on a Rigaku Smartlab using Cu-Ka1 radiation at a scan rate of 0.05° 2θ⁻¹s and were used to determine the phase structures of the samples. Scanning electron microscopy (SEM) analysis was conducted using a JEM-2100F microscope (JEOL, Japan) at a 20kV accelerating

voltage. The UV-vis diffuse reflectance spectra were obtained on Perkin Elmer Lambda 950 UV/Vis/NIR spectrophotometer equipped with a 150 mm snap-in integrating sphere for capturing diffuse and specular reflectance. $BaSO_4$ was used as a reflectance standard in the UV-visible diffuse reflectance experiment. X-Ray photoelectron spectroscopy (XPS) measurements were performed on the ESCALAB-210 spectrometer (Thermo VG Scientific, UK) with an Mg-Ka source. All the binding energies were referenced to the C1s peak at 284.6 eV of the surface adventitious carbon.

The photocatalytic activity of the prepared samples in terms of the photocatalytic decolourization of methylene blue (MB) aqueous solution was performed at ambient temperature under visible-light irradiation using a 500W Xe lamp (15 cm above the dishes) as a light source. In the photo catalysis experiments, 0.1 g of the prepared photo catalyst powder was dispersed in a 100 mL MB aqueous solution with a concentration of 10 ppm in a beaker. The mixed solution was remained in dark for an hour to establish an MB solution adsorption–desorption equilibrium on the photo catalyst before light irradiation.

7.3   Results and Discussion

7.3.1   Structure and Morphology of S-doped ZnO

All the x-ray diffraction data were collected form the Rigaku Smart Lab using Cu-Kα1 radiation at a scan rate of 0.05° $2\theta^{-1}$s and were used to determine the phase of the structures of the samples. In the Figure 7-1, it shows clear XRD patterns of the prepared 5 samples calcined at 450℃. All the Bragg diffraction peaks of the ZnO and S-doped ZnO can be identified and indexed according to the hexagonal wurtzite ZnO (P63mc, JCPSD: 890511), though the S-doped ZnO shows an obvious weaker diffraction intensity compared with ZnO, which unveils the fact that sulphur doped ZnO possesses lower crystallinity or smaller crystallite size. The shift of the strongest peak in the diffraction shows that the sulphur doping contributes to the change in the parameter of the ZnO cell. As the data listed in Table 7-2, crystal size, lattice parameter and unite cell volume of the S doped ZnO are indeed greater than the ZnO. The difference of the lattice parameter can be attributed to the presence of the sulphur atoms in the structure. Given the fact that radius of the sulphur is greater than the oxygen, the replacement of the sulphur will intrigue expansion of the crystal cell. As for the last group, there is a dramatic fall in the parameter which is probably the result of the transformation of the crystal phase.
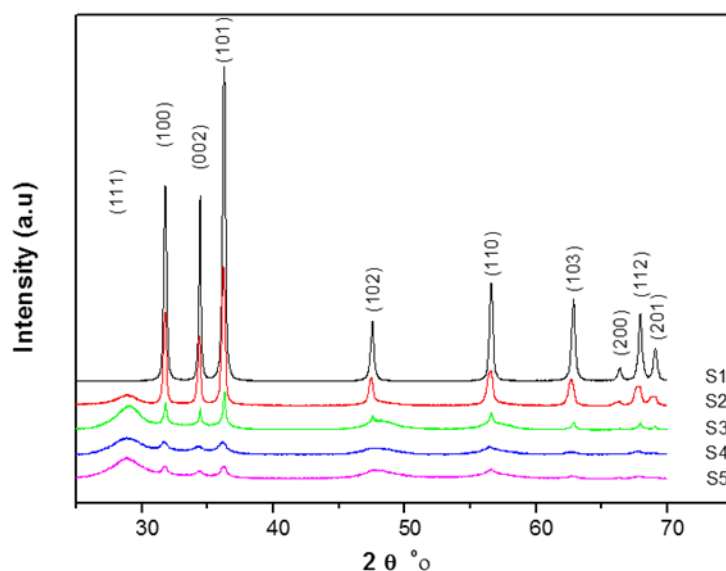
Figure 7-1 X-ray diffraction pattern of S-ZnO
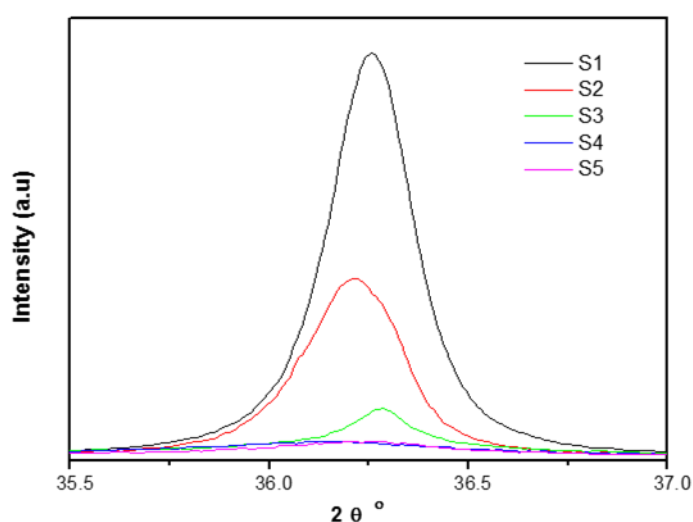
Figure 7-2 Details of the highest peak in the diffraction patterns

In the Table 7-2 the lattice parameter evidences the result of the XRD. When the S doping level reach over 1:1 with Zn, the crystal structure and the lattice changed dramatically, which can be attributed to the overwhelmingly introduced the S into the materials. Although the S ratios were quite high in the experiment, yet some part of the methionine was burn out as fuel in the pyrolysis process. Also, ZnO is more stable than ZnS in the same atmosphere because ZnO possessed a much lower Gibbs energy as -348kJ/mol compared with -204.6kJ/mol of ZnS. As a result, S doping wouldn't reach a high level in the combustion, although the ratio of methionine was relatively high in the preparations.

Table 7-2 Lattice parameter of samples

Sample	Crystallite size (nm)	Lattice parameters(Å)		Unit cell volume (Å³)
		a=b	c	
S1	39.2886	3.2488	5.2054	47.58
S2	39.8767	3.2484	5.2158	47.66
S3	45.5059	3.2470	5.2037	47.51
S4	40.8787	3.2559	5.22	47.92
S5	26.8993	3.2471	5.2104	47.58

SEM (Scanning electron microscope)
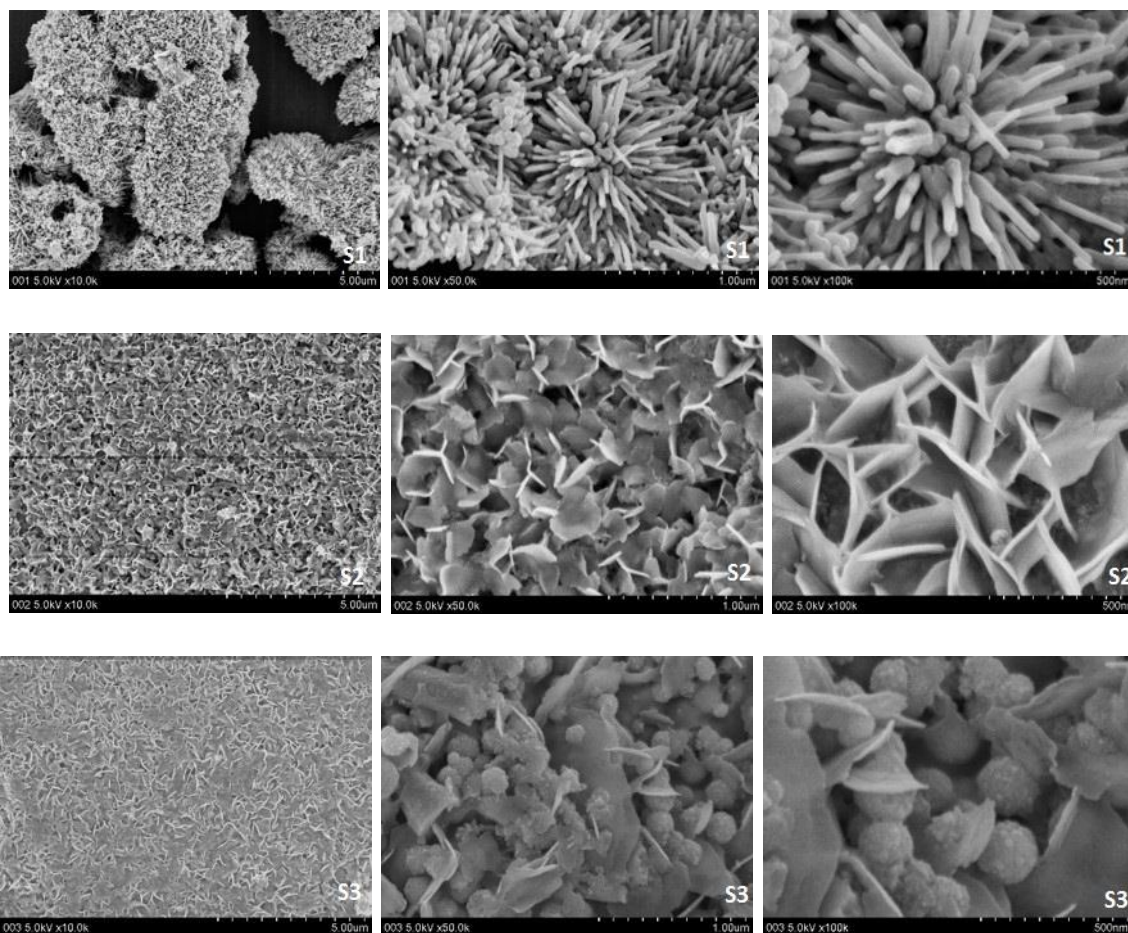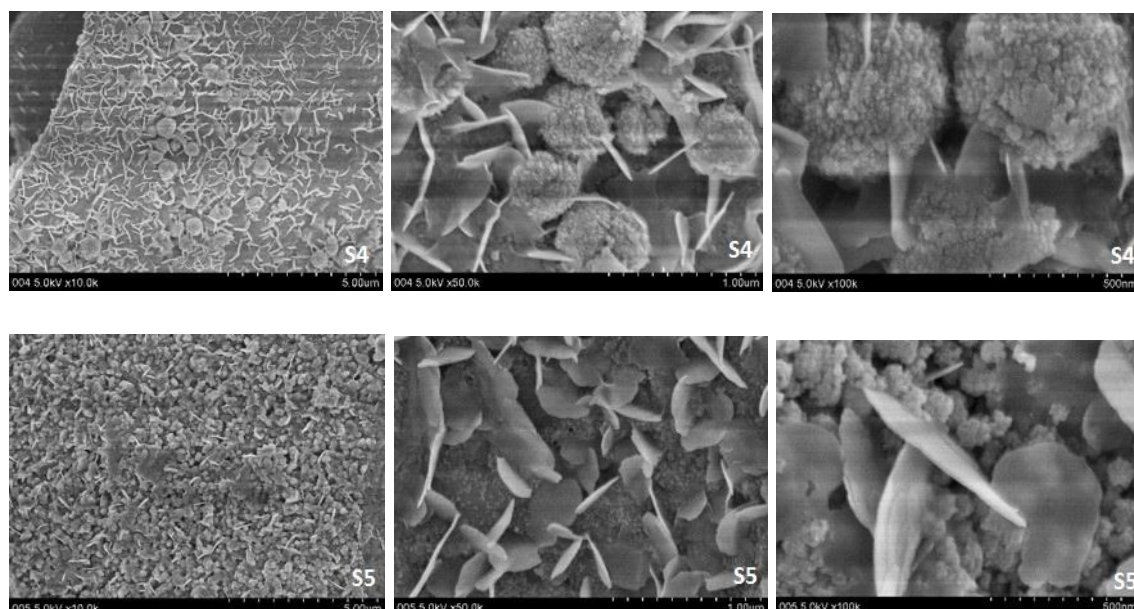
Figure 7-3 SEM pictures unveil different morphology and topology of the S-doped ZnO. An obivious transition from hierarchical nano-roads to flake cluster with amount of sulphur

The SEM images of the prepared the S-doped ZnO illustrate a gradual transition in the morphology of the materials from the hierarchical assembled nanorods to the nanoflake. With increasing the amount of the methionine, a clear trend of the transformation of the particle size was exhibited in the detailed SEM pictures. The higher level the sulphur was doped into the ZnO, the greater particle size materials would be produced, which also manifests the result in the XRD. In the images of S1, the pure ZnO exhibits flower-like assembled nanorods. Sizes of these nanorods range from 2μm to 4μm. However, when methionine introduced into the synthesis, the morphology of the materials changed instantly into nanoflakes. From sample S2 to S5, the constituent and structure of the materials gradually transformed into random mix of flakes and irregular shapes. In the detailed pictures of SEM, increasingly amount of amorphous lump took shape around the nanoflakes when S doping level increased. This phenomenon may ascribe to the aggregation of methionine. The excessive amount of methionine probably aggregated together and closely covered the Zn ions in the reaction.

7.3.2   Optical property of S-doped ZnO

The UV-vis reflectance data was collected on the Lambda 750s shown in the pictures below. In order to calculate the band gap of the catalysts, the absorption was approximate through the Kubelka-Munk Equation:

$$F(R) = \frac{(1-R)^2}{2R}$$

130

Where R is the reflectance directly collected from the spectrometer. For semiconductor samples, the optical band gap can be given by the Tauc plot $(F(R) \times hv)^n$ vs. hv. As for a direct band gap semiconductor like ZnO, the plot n=1/2 will show a linear Tauc region just above the optical absorption edge. Extrapolation of the line to the photon energy axis yields the semiconductor band gap of the sulphur doped ZnO. The difference of the light absorption characteristics was comparatively presented in the Figure 7-4. Compared with the pure ZnO, the band gap of the S doped ZnO (except for the last one) is gradually decreased with the amount of sulphur increased. However, when sulphur ratio to ZnO is over 1:1, the band gap of the photo-catalyst increase.
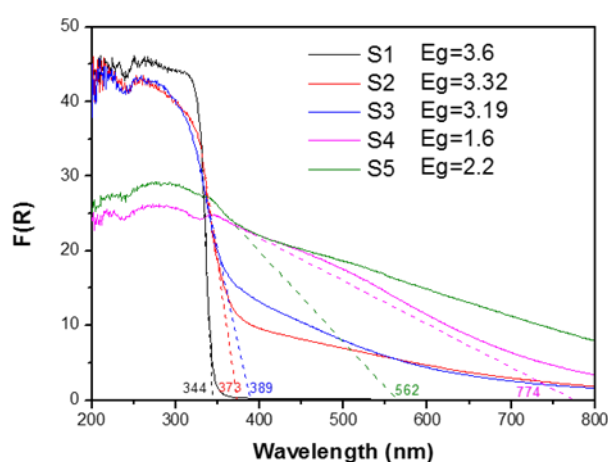
Figure 7-4 Uv-vis absorbance spectra and correspond reflectance vs. wavelength plot
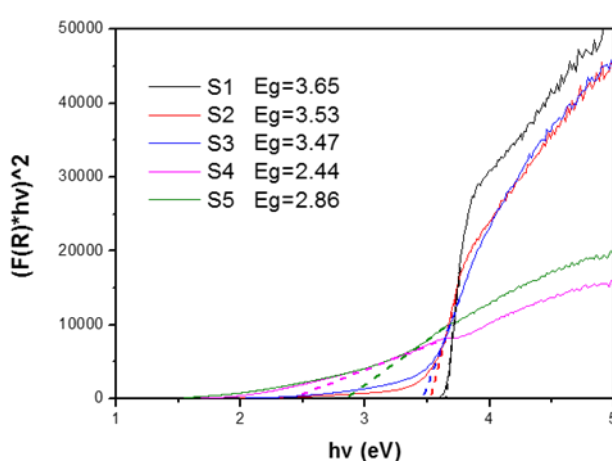
Figure 7-5 Tauc plot of different samples according to the UV-vis spectra

7.3.3   The Influence of Zn-dopant on Energy Band Structure

The XPS measurement was conducted to analyse the surface species and valence band of ZnO and S doped ZnO. The core-level XPS clearly evidences that Sulfur has been doped into ZnO in both sulfur cations (S-O and S=O) and anion (Zn-S bond) modes. The mode and amount of S species are directly proportionate to the Zn/methionine ratio. Valance band (VB) XPS shows S-doping may upshift VB maximum (VBM) and expands VB band width regardless of the mode of sulfur species. According to the intrinsic XPS peaks of sulphur, the S 2p 1/2 should appear in higher binding energy compared with S 2p 3/2. As shown in the Figure 7-7, two sulphur peaks in the plot represent S 2p 1/2 and S 2p 3/2. Obviously, all the S peaks consist of two satellite peaks which could contribute to the S-O, S-S and S-Zn. By increasing the amount of methionine, in the Figure 7-8, there is a clear red-shift in the peak of S 2p 1/2, which is resulting from the reduced Sulphur spices as increasing the amount of methionine acted as reductant in the pyrolysis.

Figure 7-7 shows the O1s XPS of pure and S-doped ZnO calcines at 450 °C. For pure ZnO, a large O 1s locates at 529.8eV is due to Zn-O bonds in wurtzite ZnO crystal, and a shoulder peak (531.3eV) of 25% height to the major peak may be due to surface chemical adsorbed oxygen species, such as OH- group and carbonates. The O1s XPS of S-doped ZnO encompass a peak of Zn-O is gradually left-shifted and diminished in the intensity. O1s XPS of S-doped ZnO were fitted into three peaks centering at 529.8 eV, 531.5 eV and 532.2 eV. The peak at 529.8 eV can be ascribe to Zn-O bond, while the peaks located at 531.5 eV is assigned to the oxygen species (OH group) and carbonate 532.2 eV can be reasonably attributed to the sulfate in S-doped ZnO. It is difficult to determine the concentration of ZnSO4 or ZnO species from the O1s XPS because the peaks are heavily overlapped. However, a significant increase of the S-Zn bond in the S-doped ZnO can be identified as increasing amounts of methionine.
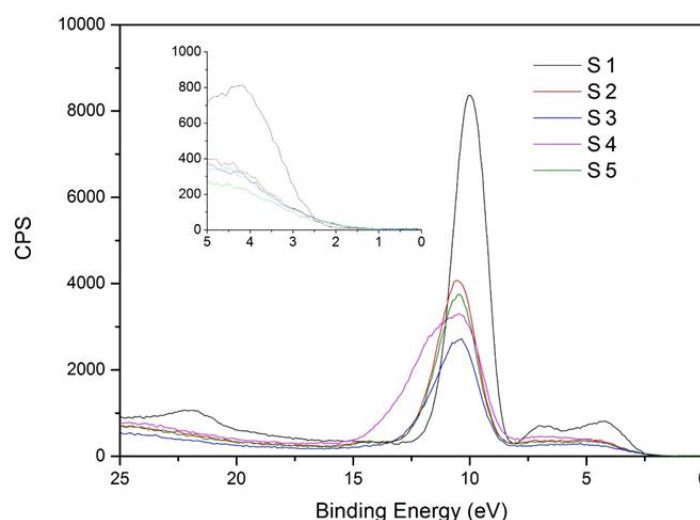
Figure 7-6 XPS survey of different samples, Sample 1-5 with increasing amount of S in the materials

Valence band (VB) XPS is a powerful tool to investigate the influence of impurity on the band structure of semiconductors. Figure 7-6 comparatively shows VB XPS spectra acquired on ZnO and S-doped ZnO. It clearly shows the C-doping not only red-shifts valance band maximum (VBM) energy but also expands the VB band width. The VBM of ZnO is approximately 2.24 eV relative to vacuum level, however it rose to 1.43 eV when sulphur was introduced in the material, indicating the rising of valence band in the S-doped ZnO. In addition, the ZnO VB with width about 6.0 eV is more localized with clear discrete energy levels than the VB of S-doped ZnO. The VB of S-doped ZnO is greater than 7.0 eV and overlapped with deeper energy level, revealing its VB electrons are delocalized and more dispersive.
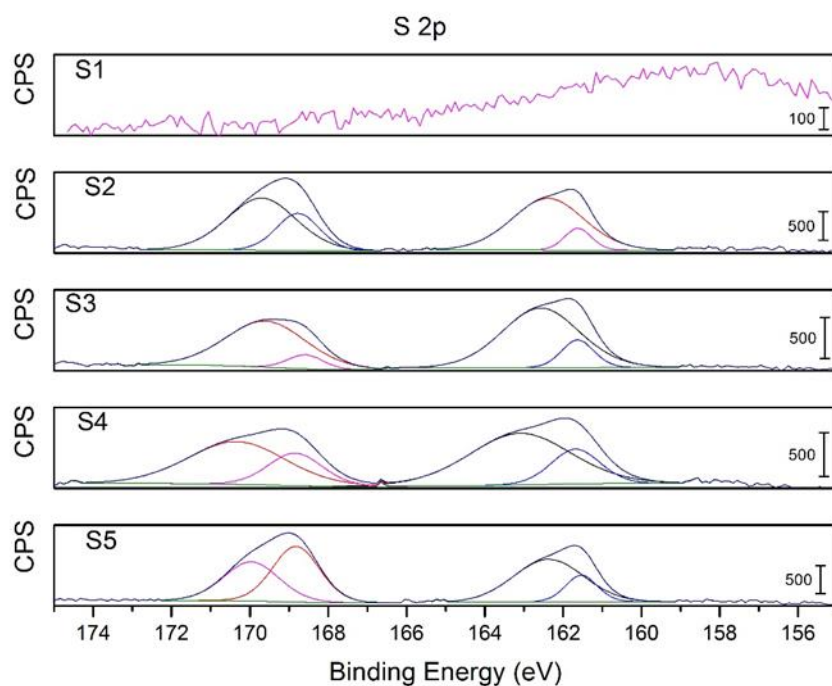
Figure 7-7 XPS peaks of the sulphur 2p, S1-5 with increasing amount of S in the materials
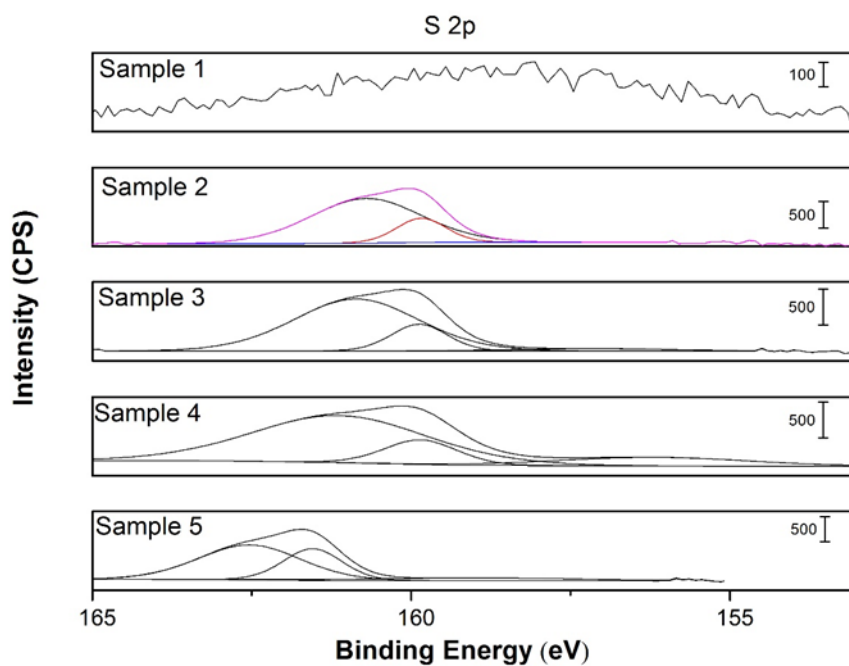
Figure 7-8 XPS patterns of sulphur 2p 3/2, Sample1-5 with increasing amount of S in the materials
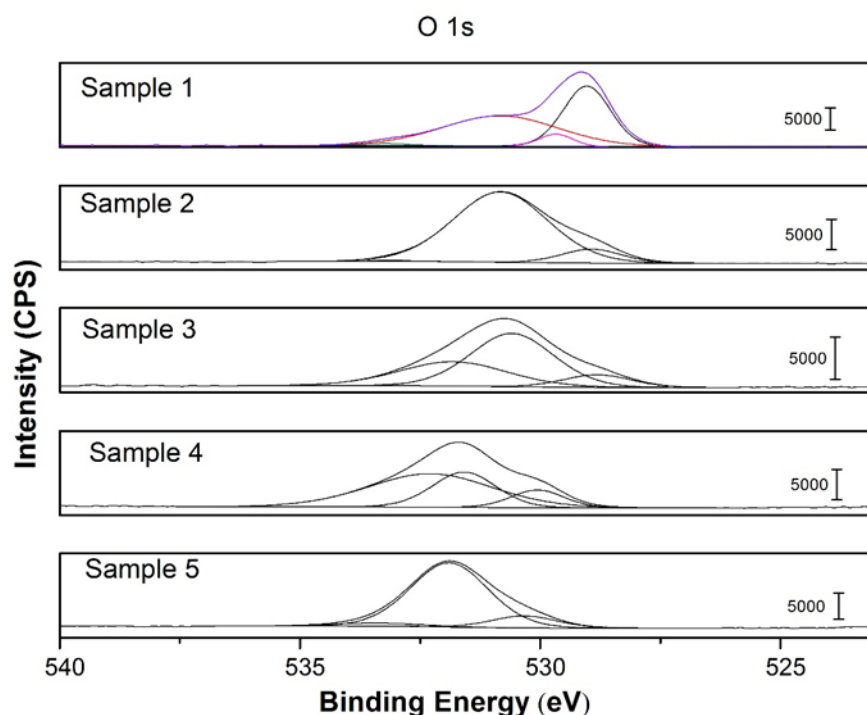
Figure 7-9 XPS patterns of the oxygen in the samples, Sample1-5 with increasing amount of S in the materials

7.3.4   Photo-catalytic activity test

Figure 7-10 show the time-dependent absorption spectrum of degradation of methylene blue (MB) on the S-ZnO under the visible light and full arc of the illumination. The photo-degradation should be induced by the photocatalytic reaction because the MB degradation is negligible without photo-catalysts and no degradation was observed in the dark. The spectrums reveal that although the S doped ZnO did promote the light absorption, ZnO exhibits a notable higher activeness in the photo-catalytic degradation in the MB than S-ZnO in both visible light and full spectrum. Owing to the wide band gap, ZnO cannot be excited by the visible light so that the degradation performance of the MB on the ZnO can be attributed to the dye-sensitized photo-catalysis. Under visible light, illumination of MB is excited by the light shorter than its characteristic absorption wavelength 662nm and then injects photo-excited electrons into the ZnO CB [200]. The electrons injected onto ZnO CB react with dissolved oxygen and give rise to active oxygen species which can decompose the excited MB. In contrast, S-doped ZnO may be excited by visible light due to its narrowed band gap to valence electrons onto CB and leave holes on VB. Furthermore, S-doped ZnO should have shown stronger dye-sensitising effect than ZnO since sensitising opportunity should be increased due to higher MB adsorption amount. It seems that the heavy S-doped

ZnO should be more active, whereas the experimental results demonstrate that it is less active than ZnO, suggesting heavy S-doping would deteriorate the dye-sensitised photo-degradation. It is reasonable to conclude that bandgap excitation of the S-doped ZnO contributes a little to the overall MB photo-degradation in comparison to the dye-sensitisation under visible-light illumination. The fact is that heavy S-doping and derived O vacancy would correspondingly serve as recombination centres in the photoreaction which may reduce dye-sensitising effects by trapping the electrons from excited dyes, and thus deteriorate photo-degradation on C-doped ZnO relative to ZnO.
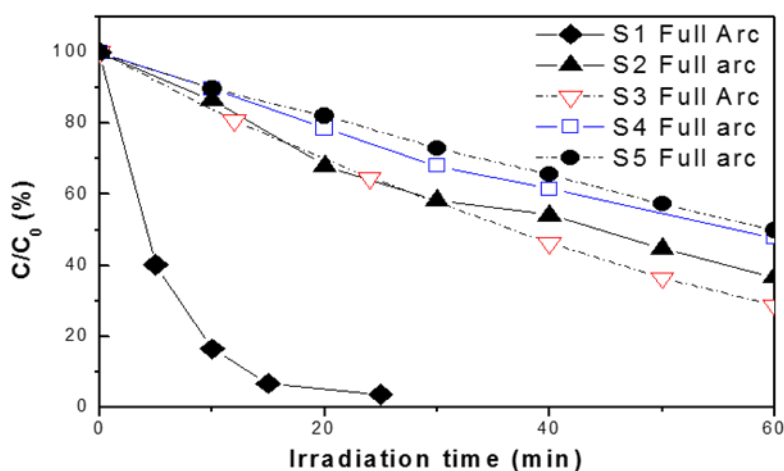
Figure 7-10 Photocatalytic activity of methylene blue degradation on ZnO and S-doped ZnO under full arc irradiation
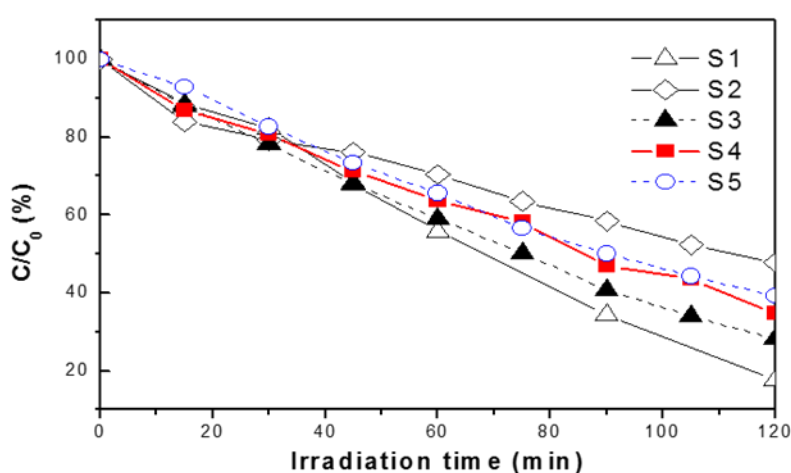
Figure 7-11 ZnO and S-doped ZnO photocatalytic activity for methylene blue degradation in visible light.

7.3.5 Antibacterial Test

Since sulphur is commonly used in the sterilization and disinfection in the medical care and the daily life. At the same time, during the photo-catalysis process the oxide radicals emerge in the particles, which may also enable the antibacterial process. Furthermore, considering its performance in the MB degradation test, S-doped ZnO were also expected to present a good performance in the antibacterial test. The experiment was divided into 5 groups with different doping levels S-doped ZnO. In order to identify its light-responded antibacterial activity, a controlled experiment was introduced into each group where photo-catalyst with bacteria, in the same concentration, was placed in the dark. For the test, plastic loops of bacteria were dispersed evenly in a small amount of 1/500 nutrient broth and the bacterial cell content of the suspension for inoculation was adjusted to about 108 cells/ml. The result unveiled that S-doped ZnO showed a remarkable performance in the antibacterial test.
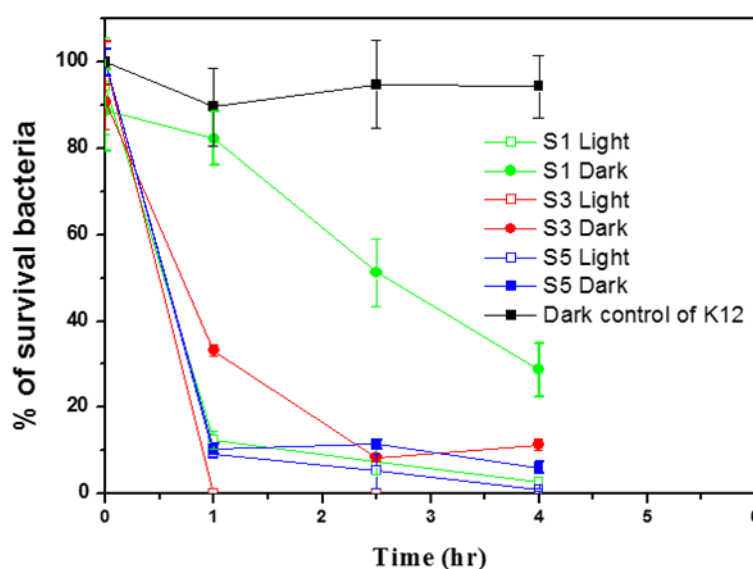
Figure 7-12 Antibacterial result of ZnO and S-doped ZnO under visible light.

In Figure 7-12, ZnO and S-doped ZnO samples all exhibited antibacterial property, while S-doped samples outperformed ZnO in dark and under light irradiation. All samples showed better antibacterial activity under light than in dark, indicating photo-catalysis contribute to their antibacterial performance. The photocatalytic contribution is much more significant for ZnO sample than S-doped samples. In the dark, S-doped ZnO exhibits comparable bactericidal activity to the pure ZnO under light, suggesting S-doped sample possesses intrinsic antibacterial property.

137

Compared with all the S-doped ZnO performance in the antibacterial test, increasing S-doping level just slightly enhances their antibacterial performance; however, it significantly reduced the photo-degradation performance in the MB solution. ZnO showed notably higher activity in photo-reduction of MB than S-doped ZnO, further confirming limited contribution of photo-catalysis for S-doped ZnO to antibacterial. From Figure 7-12, the exciting results suggest that S-doped ZnO is of great potential the sterilization and medical care.

7.4   Conclusion

We established a rapid pyrolysis method for facile synthesis of S-doped ZnO with controlled S-doping level and desired hierarchical morphology. Zn/methionine ratios govern the S-doping level, morphology, crystallinity and light adsorption of the S-doped ZnO.

S-doped ZnO with large surface area were successfully synthesised via pyrolysis process using methionine as direct agent. The S-doping leads to enhanced UV and visible light absorption yet does not affect the electron transition feature of ZnO. VBM XPS evidence the S-doping expands valence band width of ZnO and lifts its VBM energy as well as narrowed down the band gap. Although the S-doped ZnO showed enhanced light absorption in the UV test, its visible light activity test in MB photo-degradation is not as good as the pure ZnO because the S-doping led to significant charge recombination. In the antibacterial test, both kinds of the materials showed a good potential in the sterilization. However, photocatalysis contributes significantly for antibacterial property on ZnO, while S-doped ZnO possess intrinsic bactericidal capability less dependent of photo-catalysis.

Chapter 8 Conclusion & Future work

8.1   Conclusion

ZnO as a simple efficient second semiconductor in the heterojunctions was first prepared and examined. In this project, S-doped hierarchical ZnO was prepared via a simple combustion synthesis. Unlike metal doped BiOBr, S doped ZnO present a superior photocatalytic degradation. It is worth noting that S-doped ZnO also exhibited improved antibacterial performance with comparison of pure ZnO. However, due to the limitation of the equipment, PEC and water splitting performance was not measured. Although the heterojunction of ZnO/BiOBr were successfully prepared via hydrothermal synthesis, the photocatalytic performance of the hybrid materials is not as our expectation. The reduction in the photocatalytic performance of ZnO/BiOBr can be ascribed to the overwhelming amount of BiOBr cover up the ZnO seeds.

BiOBr is a promising photocatalyst for versatile application including solar energy conversion and environment remediation because of its unique layered structure and outstanding physic-chemical properties. However, the inherent drawbacks such as small specific surface area, low efficiency of solar energy harvesting and pH sensitivity have limited the photocatalytic performance of pristine BiOBr. To address these challenges, plenty of effort has been made in this project to improve the photocatalytic performance of BiOBr, including band structure engineering, morphology design and synthesis of heterojunction.

By introducing transitional metal Zn into the lattice of BiOBr, the influence of Zn doping on both energy band position and light absorbance were investigate by DFT calculations and XPS analysis. Meanwhile, the mechanism of the uphill and downhill energy conversion was also closely evaluated by the means of the photodegardation and PEC results. The results confirmed that the holes are the rate limiting species during the photodegardation process. And the detrimental of the degradation process can be ascribed to the broadened band gap due the Zn-dopant. However, the uphill energy conversion of ZnBiOBr is superior to that of pristine BiOBr due to the uprising of the CBM as well as the reduction of the charge recombination. Similar results were also confirmed in the hierarchically structured BiOBr.

In the hierarchically structured BiOBr and Zn-doped BiOBr, the photocatalytic performance was further promoted in both hydrogen evolution and chemical

degradation. Energy extraction of BiOBr form the waste was also testified by chronoamperometry with several simple organic compounds introduced into the electrolyte respectively.

Moreover, the p-n junction of BiOBr$_x$I$_{1-x}$/CuSCN was also investigated in the reaserch. Due to the inner built electric field within the depletion zone of p-n junction, the photo-induced electron-hole pairs were separate and transported to the surface and bulk of the material superlatively. Hence, stronger photo response currents were observed indicating a stronger photocatalytic activity. However, CuSCN is not stable at the temperature more than 150 ℃. The decomposition of CuSCN would break the junction with BiOBr. In this case, the charge transfer from the top layer of BiOBr would be blocked.

Generally, the photocatalytic performance of BiOBr is not only depends on the morphology and light absorbance, but also lie with energy band position. The energy band positions of the materials determine the oxidation and reduction state during the reaction. Although the heterojunction with second semiconductor can improve the photocatalytic performance, yet imbalanced ratio between the materials would also result in the detrimental impact on the photoreactions.

8.2   Future work

Although the relation between energy band and photocatalytic performance of BiOBr-based materials were explored in this work, yet some of the problems need further discussion.

1. Abnormal charge transfer between electrodes and electrolyte. During the photo-electrochemistry test, the photocurrent from the BiOBr films sometime exhibited cathodic behaviour instead of anodic. And this phenomenon disappears after a long-time irradiation.

2. According to a series experiment, the influence from heterojunction in the photocatalytic reaction require more detailed discussion, because some heterojunction showed a decreased photocatalytic activity, which is quite different from previous reports.

3. The device fabrication. More efforts should be made to prepare a complete photocatalytic device, such as photocatalytic cells. And chemical property of electrolyte and solvent in the cells need more investigation as well.

Reference

1. Mcdevitt, J.T., *Photoelectrochemical Solar-Cells.* Journal of Chemical Education, 1984. **61**(3): p. 217-221.

2. Oregan, B. and M. Gratzel, *A Low-Cost, High-Efficiency Solar-Cell Based on Dye-Sensitized Colloidal Tio2 Films.* Nature, 1991. **353**(6346): p. 737-740.

3. Huang, W.L., *Electronic structures and optical properties of BiOX (X = F, Cl, Br, I) via DFT calculations.* J Comput Chem, 2009. **30**(12): p. 1882-91.

4. Kahn, A., *Fermi level, work function and vacuum level.* Materials Horizons, 2016. **3**(1): p. 7-10.

5. Fujishima, A., X. Zhang, and D. Tryk, *TiO2 photocatalysis and related surface phenomena.* Surface Science Reports, 2008. **63**(12): p. 515-582.

6. Wang, Y., et al., *Visible-Light Driven Overall Conversion of CO2 and H2O to CH4 and O2 on 3D-SiC@2D-MoS2 Heterostructure.* J Am Chem Soc, 2018. **140**(44): p. 14595-14598.

7. Zonno, I., et al., *Understanding Mott-Schottky Measurements under Illumination in Organic Bulk Heterojunction Solar Cells.* Physical Review Applied, 2017. **7**(3): p. 034018.

8. Shishido, T., K. Teramura, and T. Tanaka, *Photo-Induced Electron Transfer Between a Reactant Molecule and Semiconductor Photocatalyst: In Situ Doping.* Catalysis Surveys from Asia, 2011. **15**(4): p. 240-258.

9. Zhu, H., et al., *Surface states as electron transfer pathway enhanced charge separation in TiO 2 nanotube water splitting photoanodes.* Applied Catalysis B: Environmental, 2018. **234**: p. 100-108.

10. Garland, J.E., D.J. Crain, and D. Roy, *Utilization of electrochemical impedance spectroscopy for experimental characterization of the diode features of charge recombination in a dye sensitized solar cell.* Electrochimica Acta, 2014. **148**: p. 62-72.

11. Goes, M.S., et al., *Impedance Spectroscopy Analysis of the Effect of TiO2 Blocking Layers on the Efficiency of Dye Sensitized Solar Cells.* Journal of Physical Chemistry C, 2012. **116**(23): p. 12415-12421.

12. Zhang, H.J., L. Liu, and Z. Zhou, *First-principles studies on facet-dependent photocatalytic properties of bismuth oxyhalides (BiOXs).* Rsc Advances, 2012. **2**(24): p. 9224-9229.

13. Jiang, D., et al., *Novel p-n heterojunction photocatalyst constructed by porous graphite-like C3N4 and nanostructured BiOI: facile synthesis and enhanced photocatalytic activity.* Dalton Trans, 2013. **42**(44): p. 15726-34.

14. An, H., et al., *Photocatalytic properties of BiOX (X = Cl, Br, and I).* Rare Metals, 2008. **27**(3): p. 243-250.

Reference

15. Amano, F., et al., *Correlation between surface area and photocatalytic activity for acetaldehyde decomposition over bismuth tungstate particles with a hierarchical structure.* Langmuir, 2010. **26**(10): p. 7174-80.

16. Bai, H., et al., *Large-scale production of hierarchical TiO2 nanorod spheres for photocatalytic elimination of contaminants and killing bacteria.* Chemistry, 2013. **19**(9): p. 3061-70.

17. Cho, J., et al., *Sulfur-doped zinc oxide (ZnO) Nanostars: Synthesis and simulation of growth mechanism.* Nano Research, 2011. **5**(1): p. 20-26.

18. Hoffmann, M.R., et al., *Environmental Applications of Semiconductor Photocatalysis.* Chemical Reviews, 1995. **95**(1): p. 69-96.

19. Zou, L., H.R. Wang, and X. Wang, *High Efficient Photodegradation and Photocatalytic Hydrogen Production of CdS/BiVO4 Heterostructure through Z-Scheme Process.* Acs Sustainable Chemistry & Engineering, 2017. **5**(1): p. 303-309.

20. Liu, N., et al., *A review on TiO2-based nanotubes synthesized via hydrothermal method: Formation mechanism, structure modification, and photocatalytic applications.* Catalysis Today, 2014. **225**: p. 34-51.

21. Mojiri, A., et al., *Spectral beam splitting for efficient conversion of solar energy—A review.* Renewable and Sustainable Energy Reviews, 2013. **28**: p. 654-663.

22. Ni, M., et al., *A review and recent developments in photocatalytic water-splitting using TiO2 for hydrogen production.* Renewable & Sustainable Energy Reviews, 2007. **11**(3): p. 401-425.

23. Sahinkaya, M.N., A.R. Plummer, and B. Drew, *A review of wave energy converter technology.* Proceedings of the Institution of Mechanical Engineers, Part A: Journal of Power and Energy, 2009. **223**(8): p. 887-902.

24. Arico, A.S., et al., *Nanostructured materials for advanced energy conversion and storage devices.* Nat Mater, 2005. **4**(5): p. 366-77.

25. Li, X., J. Yu, and M. Jaroniec, *Hierarchical photocatalysts.* Chem Soc Rev, 2016. **45**(9): p. 2603-36.

26. Schneider, J., et al., *Understanding TiO2 Photocatalysis: Mechanisms and Materials.* Chemical Reviews, 2014. **114**(19): p. 9919-9986.

27. Triboulet, R., *Growth of ZnO bulk crystals: A review.* Progress in Crystal Growth and Characterization of Materials, 2014. **60**(1): p. 1-14.

28. Xia, Y., et al., *Shape-controlled synthesis of metal nanocrystals: simple chemistry meets complex physics?* Angew Chem Int Ed Engl, 2009. **48**(1): p. 60-103.

29. Wu, W., J. Changzhong, and V.A. Roy, *Recent progress in magnetic iron oxide-semiconductor composite nanomaterials as promising photocatalysts.* Nanoscale, 2015. **7**(1): p. 38-58.

30. Bard, A.J., *Photoelectrochemistry.* Science, 1980. **207**(4427): p. 139-44.

31. Bard, A.J., et al., *The Concept of Fermi Level Pinning at Semiconductor-Liquid Junctions - Consequences for Energy-Conversion Efficiency and Selection of Useful Solution Redox Couples in Solar Devices.* Journal of the American Chemical Society, 1980. **102**(11): p. 3671-3677.

32. Fan, J.C., et al., *p-Type ZnO materials: Theory, growth, properties and devices.* Progress in Materials Science, 2013. **58**(6): p. 874-985.

33. Li, Y., et al., *Hexagonal-close-packed, hierarchical amorphous TiO2 nanocolumn arrays: transferability, enhanced photocatalytic activity, and superamphiphilicity without UV irradiation.* J Am Chem Soc, 2008. **130**(44): p. 14755-62.

34. Du, Y.K. and J. Rabani, *The measure of TiO2 photocatalytic efficiency and the comparison of different photocatalytic titania.* Journal of Physical Chemistry B, 2003. **107**(43): p. 11970-11978.

35. Bavykin, D.V., L. Passoni, and F.C. Walsh, *Hierarchical tube-in-tube structures prepared by electrophoretic deposition of nanostructured titanates into a TiO2 nanotube array.* Chem Commun (Camb), 2013. **49**(62): p. 7007-9.

36. Znaidi, L., *Sol–gel-deposited ZnO thin films: A review.* Materials Science and Engineering: B, 2010. **174**(1-3): p. 18-30.

37. Ong, C.B., L.Y. Ng, and A.W. Mohammad, *A review of ZnO nanoparticles as solar photocatalysts: Synthesis, mechanisms and applications.* Renewable & Sustainable Energy Reviews, 2018. **81**: p. 536-551.

38. Cheng, C., et al., *Enhanced photocatalytic performance of TiO2-ZnO hybrid nanostructures.* Sci Rep, 2014. **4**: p. 4181.

39. Qi, L., H. Li, and L. Dong, *Simple synthesis of flower-like ZnO by a dextran assisted solution route and their photocatalytic degradation property.* Vol. 107. 2013.

40. Lu, H., et al., *Hierarchical ZnO microarchitectures assembled by ultrathin nanosheets: hydrothermal synthesis and enhanced photocatalytic activity.* Journal of Materials Chemistry, 2011. **21**(12): p. 4228.

41. Di, J., et al., *Bismuth oxyhalide layered materials for energy and environmental applications.* Nano Energy, 2017. **41**: p. 172-192.

42. Dash, A., et al., *Microwave synthesis, photoluminescence, and photocatalytic activity of PVA-functionalized Eu3+-doped BiOX (X = Cl, Br, I) nanoflakes.* Langmuir, 2014. **30**(5): p. 1401-9.

43. Lu, L., et al., *Tuning the physicochemical property of BiOBr via pH adjustment: Towards an efficient photocatalyst for degradation of bisphenol A.* Journal of Molecular Catalysis a-Chemical, 2016. **423**: p. 379-385.

44. Jiang, Z., et al., *The hydrothermal synthesis of BiOBr flakes for visible-light-responsive photocatalytic degradation of methyl orange.* Journal of Photochemistry and Photobiology A: Chemistry, 2010. **212**(1): p. 8-13.

45. Snaith, H.J. and L. Schmidt-Mende, *Advances in liquid-electrolyte and solid-state dye-sensitized solar cells.* Advanced Materials, 2007. **19**(20): p. 3187-3200.

46. Wijeyasinghe, N. and T.D. Anthopoulos, *Copper(I) thiocyanate (CuSCN) as a hole-transport material for large-area opto/electronics.* Semiconductor Science and Technology, 2015. **30**(10): p. 104002.

Reference

47.   O'Regan, B., et al., *Electrodeposited Nanocomposite n-p Heterojunctions for Solid-State Dye-Sensitized Photovoltaics.* Advanced Materials, 2000. **12**(17): p. 1263-1267.

48.   Liu, C.L., et al., *Orientation growth and electrical property of CuSCN films associated with the surface states.* Crystengcomm, 2012. **14**(20): p. 6750-6754.

49.   Ghosh, S. and S.K. Sarkar, *Controlled morphology of electrochemically deposited CuSCN by variation of applied bias voltage.* 4 International Conference on Advances in Energy Research (Icaer 2013), 2014. **54**: p. 777-781.

50.   Shang, J., et al., *Bismuth Oxybromide with Reasonable Photocatalytic Reduction Activity under Visible Light.* Acs Catalysis, 2014. **4**(3): p. 954-961.

51.   Greene, L.E., et al., *Solution-grown zinc oxide nanowires.* Inorg Chem, 2006. **45**(19): p. 7535-43.

52.   Lin, C.C. and Y.J. Chiang, *Preparation of coupled ZnO/SnO2 photocatalysts using a rotating packed bed.* Chemical Engineering Journal, 2012. **181**: p. 196-205.

53.   Johra, F.T. and W.G. Jung, *RGO-TiO2-ZnO composites: Synthesis, characterization, and application to photocatalysis.* Applied Catalysis a-General, 2015. **491**: p. 52-57.

54.   Jiang, G.H., et al., *Photocatalytic properties of hierarchical structures based on Fe-doped BiOBr hollow microspheres.* Journal of Materials Chemistry A, 2013. **1**(7): p. 2406-2410.

55.   Guo, W., et al., *PEG-20000 assisted hydrothermal synthesis of hierarchical ZnO flowers: Structure, growth and gas sensor properties.* Physica E: Low-dimensional Systems and Nanostructures, 2015. **73**: p. 163-168.

56.   Ho, W., J.C. Yu, and S. Lee, *Synthesis of hierarchical nanoporous F-doped TiO2 spheres with visible light photocatalytic activity.* Chem Commun (Camb), 2006(10): p. 1115-7.

57.   Beranek, R., *(Photo)electrochemical Methods for the Determination of the Band Edge Positions of TiO2-Based Nanomaterials.* Advances in Physical Chemistry, 2011. **2011**: p. 1-20.

58.   Kim, S.H., et al., *Hierarchical ZnO structures templated with amino acid based surfactants.* Microporous and Mesoporous Materials, 2012. **151**: p. 64-69.

59.   Wang, J. and Y. Li, *Synthesis of single-crystalline nanobelts of ternary bismuth oxide bromide with different compositions.* Chem Commun (Camb), 2003. **3**(18): p. 2320-1.

60.   Xue, Y., et al., *Controllable synthesis of uniformly distributed hollow rutile TiO2 hierarchical microspheres and their improved photocatalysis.* Materials Chemistry and Physics, 2013. **143**(1): p. 446-454.

61.   Gao, J., et al., *High-yield synthesis of millimetre-long, semiconducting carbon nitride nanotubes with intense photoluminescence emission and reproducible photoconductivity.* Nanoscale, 2012. **4**(12): p. 3687-3692.

62. Xia, J., et al., *Self-assembly and enhanced photocatalytic properties of BiOI hollow microspheres via a reactable ionic liquid.* Langmuir, 2011. **27**(3): p. 1200-6.

63. Xia, J.X., et al., *Enhanced photocatalytic activity of bismuth oxyiodine (BiOI) porous microspheres synthesized via reactable ionic liquid-assisted solvothermal method.* Colloids and Surfaces a-Physicochemical and Engineering Aspects, 2011. **387**(1-3): p. 23-28.

64. Xia, J., et al., *Improved visible light photocatalytic activity of sphere-like BiOBr hollow and porous structures synthesized via a reactable ionic liquid.* Dalton Trans, 2011. **40**(19): p. 5249-58.

65. Xia, J., et al., *Advanced visible light photocatalytic properties of BiOCl micro/nanospheres synthesized via reactable ionic liquids.* Journal of Physics and Chemistry of Solids, 2013. **74**(2): p. 298-304.

66. Cai, T., et al., *Synthesis of hierarchically ordered egg-tray-like macroporous TiO2–SiO2 nanocomposites with ordered mesoporous walls.* Materials Letters, 2013. **111**: p. 173-176.

67. Zhao, Z.Y. and W.W. Dai, *Structural, electronic, and optical properties of Eu-doped BiOX (X = F, Cl, Br, I): a DFT+U study.* Inorg Chem, 2014. **53**(24): p. 13001-11.

68. Zhang, X., et al., *Generalized One-Pot Synthesis, Characterization, and Photocatalytic Activity of Hierarchical BiOX (X = Cl, Br, I) Nanoplate Microspheres.* The Journal of Physical Chemistry C, 2008. **112**(3): p. 747-753.

69. Xiong, J., et al., *Facile and rapid oxidation fabrication of BiOCl hierarchical nanostructures with enhanced photocatalytic properties.* Chemistry, 2013. **19**(29): p. 9472-5.

70. Jiang, Z., et al., *Enhanced visible-light-driven photocatalytic activity of mesoporous TiO(2-x)N(x) derived from the ethylenediamine-based complex.* Nanoscale, 2013. **5**(12): p. 5396-402.

71. Zhang, Z., et al., *Hierarchical assembly of ultrathin hexagonal SnS2 nanosheets onto electrospun TiO2 nanofibers: enhanced photocatalytic activity based on photoinduced interfacial charge transfer.* Nanoscale, 2013. **5**(2): p. 606-18.

72. Platt, N.J., et al., *Order of magnitude increase in photocatalytic rate for hierarchically porous anatase thin films synthesized from zinc titanate coatings.* Dalton Trans, 2017. **46**(6): p. 1975-1985.

73. Tragl, S., et al., *Template assisted formation of micro- and nanotubular carbon nitride materials.* Solid State Communications, 2007. **141**(9): p. 529-534.

74. Fragalà, M.E., et al., *Core–shell Zn-doped TiO2–ZnO nanofibers fabricated via a combination of electrospinning and metal–organic chemical vapour deposition.* CrystEngComm, 2010. **12**(11): p. 3858.

75. Sun, L., et al., *Cathodic electrodeposition of p-CuSCN nanorod and its dye-sensitized photocathodic property.* 9th International Conference on Nano-Molecular Electronics, 2011. **14**: p. 12-24.

Reference

76. Chen, H., et al., *Abnormal Cathodic Photocurrent Generated on an n-Type FeOOH Nanorod-Array Photoelectrode.* Chemistry, 2016. **22**(14): p. 4802-8.

77. Lee, H., et al., *Low-Temperature Fabrication of TiO(2) Electrodes for Flexible Dye-Sensitized Solar Cells Using an Electrospray Process.* ACS Appl Mater Interfaces, 2012.

78. Yu, J., G. Dai, and B. Cheng, *Effect of Crystallization Methods on Morphology and Photocatalytic Activity of Anodized TiO2Nanotube Array Films.* The Journal of Physical Chemistry C, 2010. **114**(45): p. 19378-19385.

79. Jumppanen, J.H. and M.L. Riekkola, *Influence of electrolyte composition on the effective electric field strength in capillary zone electrophoresis.* Electrophoresis, 1995. **16**(8): p. 1441-4.

80. Wojcik, P.J., et al., *Statistical mixture design and multivariate analysis of inkjet printed a-WO3/TiO2/WOX electrochromic films.* ACS Comb Sci, 2014. **16**(1): p. 5-16.

81. Dong, J., et al., *Defective Black TiO2 Synthesized via Anodization for Visible-Light Photocatalysis.* ACS Applied Materials & Interfaces, 2014. **6**(3): p. 1385-1388.

82. Sreekantan, S., K.A. Saharudin, and L.C. Wei, *Formation of TiO2nanotubes via anodization and potential applications for photocatalysts, biomedical materials, and photoelectrochemical cell.* IOP Conference Series: Materials Science and Engineering, 2011. **21**: p. 012002.

83. Indira, K., et al., *A Review on TiO2 Nanotubes: Influence of Anodization Parameters, Formation Mechanism, Properties, Corrosion Behavior, and Biomedical Applications.* Journal of Bio- and Tribo-Corrosion, 2015. **1**(4): p. 28.

84. De Marco, L., et al., *Highly efficient photoanodes for dye solar cells with a hierarchical meso-ordered structure.* Phys Chem Chem Phys, 2013. **15**(39): p. 16949-55.

85. Hosseini Zori, M. and A. Soleimani-Gorgani, *Ink-jet printing of micro-emulsion TiO2 nano-particles ink on the surface of glass.* Journal of the European Ceramic Society, 2012. **32**(16): p. 4271-4277.

86. Černá, M., et al., *Fabrication, characterization and photocatalytic activity of TiO2 layers prepared by inkjet printing of stabilized nanocrystalline suspensions.* Applied Catalysis B: Environmental, 2013. **138-139**: p. 84-94.

87. He, J., et al., *Diatom-templated TiO2 with enhanced photocatalytic activity: biomimetics of photonic crystals.* Applied Physics A, 2013. **113**(2): p. 327-332.

88. Bavykin, D.V., A.N. Kulak, and F.C. Walsh, *Control over the hierarchical structure of titanate nanotube agglomerates.* Langmuir, 2011. **27**(9): p. 5644-9.

89. Choi, S.K., et al., *Photocatalytic Comparison of TiO2 Nanoparticles and Electrospun TiO2 Nanofibers: Effects of Mesoporosity and Interparticle Charge Transfer.* The Journal of Physical Chemistry C, 2010. **114**(39): p. 16475-16480.

90. Erhart, P., K. Albe, and A. Klein, *First-principles study of intrinsic point defects in ZnO: Role of band structure, volume relaxation, and finite-size effects.* Physical Review B, 2006. **73**(20).

91. Bard, A.J., et al., *Electrochemical methods : fundamentals and applications.* 2nd ed. 2001, New York ; Chichester: Wiley. xxi, 833 p.

92. Finklea, H.O., *Photoelectrochemistry - Introductory Concepts.* Journal of Chemical Education, 1983. **60**(4): p. 325-327.

93. Hodes, G., *Photoelectrochemical Cell Measurements: Getting the Basics Right.* J Phys Chem Lett, 2012. **3**(9): p. 1208-13.

94. Gelderman, K., L. Lee, and S.W. Donne, *Flat-Band Potential of a Semiconductor: Using the Mott–Schottky Equation.* Journal of Chemical Education, 2007. **84**(4): p. 685.

95. Bhachu, D.S., et al., *Bismuth oxyhalides: synthesis, structure and photoelectrochemical activity.* Chem. Sci., 2016.

96. Gracia, J. and P. Kroll, *First principles study of C3N4carbon nitride nanotubes.* Journal of Materials Chemistry, 2009. **19**(19): p. 3020-3026.

97. Froschl, T., et al., *High surface area crystalline titanium dioxide: potential and limits in electrochemical energy storage and catalysis.* Chem Soc Rev, 2012. **41**(15): p. 5313-60.

98. Tian, Y., et al., *Graphitic carbon nitride–BiVO4heterojunctions: simple hydrothermal synthesis and high photocatalytic performances.* RSC Adv., 2014. **4**(8): p. 4187-4193.

99. Joo, S.H., et al., *Ordered nanoporous arrays of carbon supporting high dispersions of platinum nanoparticles.* Nature, 2001. **412**(6843): p. 169-72.

100. Kong, X.Y., et al., *Oxygen-Deficient BiOBr as a Highly Stable Photocatalyst for Efficient CO2 Reduction into Renewable Carbon-Neutral Fuels.* ChemCatChem, 2016. **8**(19): p. 3074-3081.

101. Di Fonzo, F., et al., *Hierarchically organized nanostructured TiO2 for photocatalysis applications.* Nanotechnology, 2009. **20**(1): p. 015604.

102. Greene, L.E., et al., *Low-temperature wafer-scale production of ZnO nanowire arrays.* Angew Chem Int Ed Engl, 2003. **42**(26): p. 3031-4.

103. Kong, L., et al., *Rapid synthesis of BiOBrxI1-x photocatalysts: Insights to the visible-light photocatalytic activity and strong deviation from Vegard's Law.* Catalysis Today, 2019.

104. Su, J., et al., *Nanostructured WO(3)/BiVO(4) heterojunction films for efficient photoelectrochemical water splitting.* Nano Lett, 2011. **11**(5): p. 1928-33.

105. Vernescu, B., *A Historical Perspective on Quantum Physics and its Impact on Society.* 2009.

106. Shen, G., et al., *Synthesis and optical properties of S-doped ZnO nanostructures: nanonails and nanowires.* J Phys Chem B, 2005. **109**(12): p. 5491-6.

Reference

107. Kabongo, G.L., *Luminescence investigation of zinc oxide nanoparticles doped with rare earth ions.* 2013.

108. Hill, J.C., A.T. Landers, and J.A. Switzer, *An electrodeposited inhomogeneous metal-insulator-semiconductor junction for efficient photoelectrochemical water oxidation.* Nat Mater, 2015. **14**(11): p. 1150-5.

109. Band, Y.B. and Y. Avishai, *Electronic Properties of Solids*, in *Quantum Mechanics with Applications to Nanotechnology and Information Science*, Y.B. Band and Y. Avishai, Editors. 2013, Academic Press: Amsterdam. p. 381-544.

110. Atitar, M.F., et al., *The Relevance of ATR-FTIR Spectroscopy in Semiconductor Photocatalysis.* 2015.

111. Pedron, C.F.e.D., *Caratterizzazione della composizione e struttura delle molecole attraverso misure di spettroscopia.* 2013.

112. Yang, X., et al., *Nitrogen-doped ZnO nanowire arrays for photoelectrochemical water splitting.* Nano Lett, 2009. **9**(6): p. 2331-6.

113. Shao, Z.-G., et al., *First-principles calculation of intrinsic carrier mobility of silicene.* Journal of Applied Physics, 2013. **114**(9): p. 093712.

114. Li, Z., et al., *Photocatalytic activity and DFT calculations on electronic structure of N-doped ZnO/Ag nanocomposites.* Catalysis Communications, 2011. **12**(10): p. 890-894.

115. Huang, W.L. and Q. Zhu, *DFT calculations on the electronic structures of BiOX (X = F, Cl, Br, I) photocatalysts with and without semicore Bi 5d states.* J Comput Chem, 2009. **30**(2): p. 183-90.

116. Kavan, L., et al., *Electrochemical and photoelectrochemical investigation of single-crystal anatase.* Journal of the American Chemical Society, 1996. **118**(28): p. 6716-6723.

117. Clark, S.J., et al., *First principles methods using CASTEP.* Zeitschrift für Kristallographie - Crystalline Materials, 2005. **220**(5/6).

118. Tang, H., et al., *Electrical and optical properties of TiO2 anatase thin films.* Journal of Applied Physics, 1994. **75**(4): p. 2042.

119. Albery, W.J., G.J. O'Shea, and A.L. Smith, *Interpretation and use of Mott?Schottky plots at the semiconductor/electrolyte interface.* Journal of the Chemical Society, Faraday Transactions, 1996. **92**(20): p. 4083.

120. Mora-Sero, I., et al., *Determination of carrier density of ZnO nanowires by electrochemical techniques.* Applied Physics Letters, 2006. **89**(20): p. 203117.

121. Saraf, S., M. Molotskii, and Y. Rosenwaks, *Local measurement of surface states energy distribution in semiconductors using Kelvin probe force microscope.* Applied Physics Letters, 2005. **86**(17): p. 172104.

122. Kennedy, J.H., *Flatband Potentials and Donor Densities of Polycrystalline α-Fe[sub 2]O[sub 3] Determined from Mott-Schottky Plots.* Journal of The Electrochemical Society, 1978. **125**(5): p. 723.

123. Chattot, R., et al., *Surface distortion as a unifying concept and descriptor in oxygen reduction reaction electrocatalysis.* Nat Mater, 2018. **17**(9): p. 827-833.

124.   Goodenough, J.B. and Y. Kim, *Challenges for Rechargeable Li Batteries.* Chemistry of Materials, 2010. **22**(3): p. 587-603.

125.   Hankin, A., J.C. Alexander, and G.H. Kelsall, *Constraints to the flat band potential of hematite photo-electrodes.* Phys Chem Chem Phys, 2014. **16**(30): p. 16176-86.

126.   Simon, P. and Y. Gogotsi, *Materials for electrochemical capacitors.* Nat Mater, 2008. **7**(11): p. 845-54.

127.   Hauch, A. and A. Georg, *Diffusion in the electrolyte and charge-transfer reaction at the platinum electrode in dye-sensitized solar cells.* Electrochimica Acta, 2001. **46**(22): p. 3457-3466.

128.   Wang, Q., J.E. Moser, and M. Gratzel, *Electrochemical impedance spectroscopic analysis of dye-sensitized solar cells.* J Phys Chem B, 2005. **109**(31): p. 14945-53.

129.   Cordoba-Torres, P., *Relationship between constant-phase element (CPE) parameters and physical properties of films with a distributed resistivity.* Electrochimica Acta, 2017. **225**: p. 592-604.

130.   Fabregat-Santiago, F., et al., *Influence of electrolyte in transport and recombination in dye-sensitized solar cells studied by impedance spectroscopy.* Solar Energy Materials and Solar Cells, 2005. **87**(1-4): p. 117-131.

131.   Angelo, J., et al., *Characterization of TiO2-based semiconductors for photocatalysis by electrochemical impedance spectroscopy.* Applied Surface Science, 2016. **387**: p. 183-189.

132.   Singh, M., et al., *The double layer capacitance of ionic liquids for electrolyte gating of ZnO thin film transistors and effect of gate electrodes.* Journal of Materials Chemistry C, 2017. **5**(14): p. 3509-3518.

133.   Zhang, X.C., et al., *First-principles investigation of impurity concentration influence on bonding behavior, electronic structure and visible light absorption for Mn-doped BiOCl photocatalyst.* Physica B-Condensed Matter, 2012. **407**(21): p. 4416-4424.

134.   Bi, C., et al., *Tunable photocatalytic and photoelectric properties of I⁻-doped BiOBr photocatalyst: dramatic pH effect.* RSC Adv., 2016. **6**(19): p. 15525-15534.

135.   Zhao, Z.Y., Q.L. Liu, and W.W. Dai, *Structural, Electronic, and Optical Properties of BiOX1-xYx (X, Y = F, Cl, Br, and I) Solid Solutions from DFT Calculations.* Sci Rep, 2016. **6**: p. 31449.

136.   Zhang, J., et al., *Self-Assembled 3-D Architectures of BiOBr as a Visible Light-Driven Photocatalyst.* Chemistry of Materials, 2008. **20**(9): p. 2937-2941.

137.   Hou, Q.-Y., et al., *First-principles study on the effect of high In doping on the conductivity of ZnO.* Chinese Physics B, 2013. **22**(7): p. 077103.

138.   Xu, M., et al., *Controlled Sn-Doping in TiO2 Nanowire Photoanodes with Enhanced Photoelectrochemical Conversion.* Nano Letters, 2012. **12**(3): p. 1503-1508.

Reference

139. Alshammari, A.S., et al., *Visible-light photocatalysis on C-doped ZnO derived from polymer-assisted pyrolysis.* RSC Adv., 2015. **5**(35): p. 27690-27698.

140. Henych, J., et al., *Role of bismuth in nano-structured doped TiO2 photocatalyst prepared by environmentally benign soft synthesis.* Journal of Materials Science, 2014. **49**(9): p. 3560-3571.

141. Jiang, G.H., et al., *Immobilization of N, S-codoped BiOBr on glass fibers for photocatalytic degradation of rhodamine B.* Powder Technology, 2014. **261**: p. 170-175.

142. Wei, Z., et al., *Preparation of Mn-doped BiOBr microspheres for efficient visible-light-induced photocatalysis.* Mrs Communications, 2013. **3**(3): p. 145-149.

143. Yu, J.C., et al., *Effects of F-Doping on the Photocatalytic Activity and Microstructures of Nanocrystalline TiO2Powders.* Chemistry of Materials, 2002. **14**(9): p. 3808-3816.

144. Jang, D.M., et al., *Transition-Metal Doping of Oxide Nanocrystals for Enhanced Catalytic Oxygen Evolution.* Journal of Physical Chemistry C, 2015. **119**(4): p. 1921-1927.

145. Liu, G., et al., *Unique electronic structure induced high photoreactivity of sulfur-doped graphitic C3N4.* J Am Chem Soc, 2010. **132**(33): p. 11642-8.

146. Kapilashrami, M., et al., *Probing the optical property and electronic structure of TiO2 nanomaterials for renewable energy applications.* Chem Rev, 2014. **114**(19): p. 9662-707.

147. Wu, H.-C., Y.-C. Peng, and T.-P. Shen, *Electronic and Optical Properties of Substitutional and Interstitial Si-Doped ZnO.* Materials, 2012. **5**(12): p. 2088-2100.

148. Song, X.C., et al., *The solvothermal synthesis and enhanced photocatalytic activity of Zn2+doped BiOBr hierarchical nanostructures.* New J. Chem., 2016. **40**(1): p. 130-135.

149. Liu, Z.-Q., et al., *BiOBr nanoplate-wrapped ZnO nanorod arrays for high performance photoelectrocatalytic application.* RSC Adv., 2016. **6**(20): p. 16122-16130.

150. Liu, Z., et al., *Solvothermal synthesis and photocatalytic activity of Al-doped BiOBr microspheres.* Ceramics International, 2014. **40**(4): p. 5597-5603.

151. Zhang, X., et al., *The role of Sn in enhancing the visible-light photocatalytic activity of hollow hierarchical microspheres of the Bi/BiOBr heterojunction.* Phys Chem Chem Phys, 2015. **17**(12): p. 8078-86.

152. Morrison, S.R., *Electrochemistry at semiconductor and oxidized metal electrodes.* 1980: Plenum Press.

153. Shannon, R.D., *Revised Effective Ionic-Radii and Systematic Studies of Interatomic Distances in Halides and Chalcogenides.* Acta Crystallographica Section A, 1976. **32**(Sep1): p. 751-767.

154. Shao, W., H. Wang, and X. Zhang, *Elemental doping for optimizing photocatalysis in semiconductors.* Dalton Trans, 2018. **47**(36): p. 12642-12646.

155. Wang, Y., et al., *Generating Defect-Rich Bismuth for Enhancing the Rate of Nitrogen Electroreduction to Ammonia.* Angew Chem Int Ed Engl, 2019. **0**(0).

156. Chai, B., et al., *Visible light photocatalytic performance of hierarchical BiOBr microspheres synthesized via a reactable ionic liquid.* Materials Science in Semiconductor Processing, 2014. **23**: p. 151-158.

157. Huo, Y.N., et al., *Solvothermal synthesis of flower-like BiOBr microspheres with highly visible-light photocatalytic performances.* Applied Catalysis B-Environmental, 2012. **111**: p. 334-341.

158. Dou, L., et al., *P123-assisted hydrothermal synthesis of BiOI with enhanced photocatalytic performance.* Materials Letters, 2015. **153**: p. 179-181.

159. Kato, Y., R. Nagao, and T. Noguchi, *Redox potential of the terminal quinone electron acceptor QB in photosystem II reveals the mechanism of electron transfer regulation.* Proc Natl Acad Sci U S A, 2016. **113**(3): p. 620-5.

160. Hsu, H.T., et al., *Enhanced photocatalytic activity of chromium(VI) reduction and EDTA oxidization by photoelectrocatalysis combining cationic exchange membrane processes.* J Hazard Mater, 2013. **248-249**: p. 97-106.

161. Kaifu, Z., et al., *Black N/H‐TiO2 Nanoplates with a Flower‐Like Hierarchical Architecture for Photocatalytic Hydrogen Evolution.* ChemSusChem, 2016. **9**(19): p. 2841-2848.

162. Bi, C.J., et al., *Tunable photocatalytic and photoelectric properties of I--doped BiOBr photocatalyst: dramatic pH effect.* Rsc Advances, 2016. **6**(19): p. 15525-15534.

163. Wang, H., et al., *Oxygen-Vacancy-Mediated Exciton Dissociation in BiOBr for Boosting Charge-Carrier-Involved Molecular Oxygen Activation.* J Am Chem Soc, 2018. **140**(5): p. 1760-1766.

164. Kern, R., et al., *Modeling and interpretation of electrical impedance spectra of dye solar cells operated under open-circuit conditions.* Electrochimica Acta, 2002. **47**(26): p. 4213-4225.

165. Avena, M.J., O.R. Cámara, and C.P. De Pauli, *Open circuit potential measurements with Ti/TiO2 electrodes.* Colloids and Surfaces, 1993. **69**(4): p. 217-228.

166. Minda, I., et al., *Identification of different pathways of electron injection in dye-sensitised solar cells of electrodeposited ZnO using an indoline sensitiser.* Phys Chem Chem Phys, 2016. **18**(13): p. 8938-44.

167. Young, G.J. and R.B. Rozelle, *Fuel cells.* Journal of Chemical Education, 1959. **36**(2): p. 68.

168. Zhu, T., J. Li, and Q. Wu, *Construction of TiO(2) hierarchical nanostructures from nanocrystals and their photocatalytic properties.* ACS Appl Mater Interfaces, 2011. **3**(9): p. 3448-53.

169. Pan, K., et al., *Facile fabrication of hierarchical TiO2 nanobelt/ZnO nanorod heterogeneous nanostructure: an efficient photoanode for water splitting.* ACS Appl Mater Interfaces, 2013. **5**(17): p. 8314-20.

Reference

170. Yuan, Z.Y., T.Z. Ren, and B.L. Su, *Hierarchically mesostructured titania materials with an unusual interior macroporous structure.* Advanced Materials, 2003. **15**(17): p. 1462-1465.

171. Wang, S., et al., *Novel alternating ferro-ferromagnetic two-dimensional (4,4) and photoluminescent three-dimensional interpenetrating PtS-type coordination networks constructed from a new flexible tripodal ligand as a four-connected node.* Crystal Growth & Design, 2007. **7**(4): p. 747-754.

172. Alivisatos, A.P., *Semiconductor clusters, nanocrystals, and quantum dots.* Science, 1996. **271**(5251): p. 933-937.

173. Lao, J.Y., J.G. Wen, and Z.F. Ren, *Hierarchical ZnO Nanostructures.* Nano Letters, 2002. **2**(11): p. 1287-1291.

174. Li, W.T., et al., *Synthesis of Zn2+ doped BiOCl hierarchical nanostructures and their exceptional visible light photocatalytic properties.* Journal of Alloys and Compounds, 2015. **638**: p. 148-154.

175. Guo, J., et al., *Experimental and DFT insights of the Zn-doping effects on the visible-light photocatalytic water splitting and dye decomposition over Zn-doped BiOBr photocatalysts.* Applied Catalysis B: Environmental, 2018.

176. Meng, Y.M., Y. Lin, and J.Y. Yang, *Synthesis of rod-cluster ZnO nanostructures and their application to dye-sensitized solar cells.* Applied Surface Science, 2013. **268**: p. 561-565.

177. Cohen, M.L., *Structural, electronic and optical properties of carbon nitride.* Materials Science and Engineering: A, 1996. **209**(1–2): p. 1-4.

178. Sekiguchi, T., et al., *Hydrothermal growth of ZnO single crystals and their optical characterization.* Journal of Crystal Growth, 2000. **214–215**(0): p. 72-76.

179. Li, K., et al., *Photocatalytic degradation and electricity generation in a rotating disk photoelectrochemical cell over hierarchical structured BiOBr film.* Applied Catalysis B-Environmental, 2015. **164**: p. 82-91.

180. Shoar Abouzari, M.R., et al., *On the physical interpretation of constant phase elements.* Solid State Ionics, 2009. **180**(14-16): p. 922-927.

181. Han, H., et al., *Dominant factors governing the rate capability of a TiO2 nanotube anode for high power lithium ion batteries.* ACS Nano, 2012. **6**(9): p. 8308-15.

182. Aroutiounian, V.M., V.M. Arakelyan, and G.E. Shahnazaryan, *Metal oxide photoelectrodes for hydrogen generation using solar radiation-driven water splitting.* Solar Energy, 2005. **78**(5): p. 581-592.

183. Jiang, C., et al., *Photoelectrochemical devices for solar water splitting - materials and challenges.* Chem Soc Rev, 2017. **46**(15): p. 4645-4660.

184. Law, M., et al., *Nanowire dye-sensitized solar cells.* Nat Mater, 2005. **4**(6): p. 455-9.

185. Liang, L., et al., *Porosity effects on electron transport in TiO2 films and its application to dye-sensitized solar cells.* J Phys Chem B, 2006. **110**(25): p. 12404-9.

186. Qu, J. and C. Lai, *One-Dimensional Nanostructures as Photoanodes for Dye-Sensitized Solar Cells.* Journal of Nanomaterials, 2013. **2013**: p. 1-11.

187. Zhao, Y., et al., *Zn-doped TiO2 nanoparticles with high photocatalytic activity synthesized by hydrogen-oxygen diffusion flame.* Applied Catalysis B-Environmental, 2008. **79**(3): p. 208-215.

188. Kwolek, P. and K. Szacilowski, *Photoelectrochemistry of n-type bismuth oxyiodide.* Electrochimica Acta, 2013. **104**(Supplement C): p. 448-453.

189. Scanlon, D.O., et al., *Band alignment of rutile and anatase TiO2.* Nature Materials, 2013. **12**(9): p. 798-801.

190. Jaffe, J.E., et al., *Electronic and Defect Structures of CuSCN.* Journal of Physical Chemistry C, 2010. **114**(19): p. 9111-9117.

191. Li, R., et al., *Synthesis of Bi4O5Br2 from reorganization of BiOBr and its excellent visible light photocatalytic activity.* Dalton Trans, 2016. **45**(22): p. 9182-6.

192. Wang, W., et al., *Visible-light-responsive photocatalysts xBiOBr–(1−x)BiOI.* Catalysis Communications, 2008. **9**(1): p. 8-12.

193. Calhoun, A. and G.A. Voth, *Electron Transfer Across the Electrode/Electrolyte Interface: Influence of Redox Ion Mobility and Counterions.* The Journal of Physical Chemistry, 1996. **100**(25): p. 10746-10753.

194. Liang, S., et al., *A novel ZnO nanoparticle blended polyvinylidene fluoride membrane for anti-irreversible fouling.* Journal of Membrane Science, 2012. **394**: p. 184-192.

195. Sakong, S., J. Gutjahr, and P. Kratzer, *Comparison of density functionals for nitrogen impurities in ZnO.* J Chem Phys, 2013. **138**(23): p. 234702.

196. Yan, H., et al., *Band structure design of semiconductors for enhanced photocatalytic activity: The case of TiO2.* Progress in Natural Science-Materials International, 2013. **23**(4): p. 402-407.

197. Herring, N.P., L.S. Panchakarla, and M.S. El-Shall, *P-type nitrogen-doped ZnO nanostructures with controlled shape and doping level by facile microwave synthesis.* Langmuir, 2014. **30**(8): p. 2230-40.

198. Chen, D.M., et al., *Influence of Defects on the Photocatalytic Activity of ZnO.* Journal of Physical Chemistry C, 2014. **118**(28): p. 15300-15307.

199. Fakhouri, H., et al., *Control of the visible and UV light water splitting and photocatalysis of nitrogen doped TiO2 thin films deposited by reactive magnetron sputtering.* Applied Catalysis B: Environmental, 2014. **144**: p. 12-21.

200. Ko, S.H., et al., *Nanoforest of hydrothermally grown hierarchical ZnO nanowires for a high efficiency dye-sensitized solar cell.* Nano Lett, 2011. **11**(2): p. 666-71.